Integration of Plug-in Electric Vehicles into Power Grid: Impact Analysis and Infrastructure Planning

DISSERTATION

Presented in Partial Fulfillment of the Requirements for the Degree Doctor of Philosophy in the Graduate School of The Ohio State University

By

Daijiafan Mao

Graduate Program in Electrical and Computer Engineering

The Ohio State University

2019

Dissertation Committee:

Dr. Jiankang Wang, Advisor

Dr. Mahesh Illindala

Dr. Jin Wang

Abstract

Widespread adoption of Plug-in Electric Vehicles (PEVs) brings significant social and economic benefits. The development and promotion of PEV are essential to scale up the transition to electric mobility. Overall, the large-scale integration of PEV can lead us towards a more connected and environmentally friendly world. However, without proper preparation and management, the massive PEV charging could exert an increasingly disruptive influence on the electric power grid. The goal of this dissertation is to propose algorithms and methods for grid operators and electric utilities to accurately analyze PEV's charging impact on the power system from both distribution and transmission voltage levels. The practical impact metrics provide an important tool to develop proper mitigation strategies through infrastructure planning.

PEVs are characterized as a stochastic and impulsive electric load, which means they are of high power density and vary in a fast and discrete manner. These load characteristics make conventional assessment methods unsuitable. This dissertation first proposes an algorithm, which captures the inter-temporal response of grid assets and allows fast assessment through an integrated interface. To realize these advantageous features, we establish analytic models for two generic classes of grid assets and recast their cost functions in the statistical settings of PEV charging.

The proposed impact analysis algorithm can be developed into software planning tool and embedded into utilities' strategy of impact mitigation. The current auto industry has envisioned the ability to recharge PEV at speeds comparable to the traditional gas refueling. This trend has facilitated the integration of Fast Charging Stations (FCS) into transportation service infrastructure. This dissertation, for the first time, proposes a graph-computing based integrated FCS location planning model, which maximizes PEV charging convenience while ensuring the power grid's reliability. The proposed model is cast as a multi-objective mixed-integer problem and solved by the cross-entropy optimization algorithm, in which the computational efficiency is significantly improved with graph parallel computing techniques.

On the transmission level PEV charging impact, this dissertation proposes a Graph-computing based Cascading Failure Evolution (G-CFE) analysis to predict potential cascading outages induced by FCS on power transmission systems. Fundamentally different from the existing cascading analysis tools, which are based on DC power flow or require a long computation time, the proposed method greatly improves accuracy by using AC power flow, while guaranteeing the analyzing speed with graph parallel computing techniques. The proposed G-CFE model can accurately capture the stochastic PEV charging patterns with Monte-Carlo simulation and be easily scaled to various network configurations through a graph-based scheme.

Dedication

This document is dedicated to my family.

Acknowledgments

There are many people who have helped me during my Ph.D. studies. My sincerest gratitude is to my advisor, Dr. Jiankang (J.K.) Wang, for her inspiring wisdom, expert advice, and timely encouragement. She has been extremely patient with me when I started my Ph.D., and diligently guided me towards becoming skillful in research. She is my role model for life. It is my great honor to be her student.

I would like to thank my Ph.D. defense, candidacy, and qualifying exam committee members, Dr. Mahesh Illindala, Dr. Jin Wang, Dr. Korie Edwards, Dr. Antonio Conejo, Dr. Vadim Utkin and Dr. Wei Zhang, for their valuable time, comments, and suggestions.

I would like to thank the long-time sponsor of my research projects, the Ford Motor Company. In particular, thanks to Mr. Allan Gale, Dr. Michael Degner, and Dr. Xi (Lucy) Lu for their insightful guidance through the bi-weekly teleconferences for the past three years.

I would like to thank Global Energy Interconnection Research Institute North America (GEIRINA), for generously offering me summer and spring internship opportunities and professionally collaborating in my research projects.

I am grateful for being a graduate student member of the Center for High Performance Power Electronics (CHPPE) at The Ohio State University. What an inspiring and supportive place for research, learning, and self-discovery. My sincere thanks to

my fellow colleagues: Dr. He Li, Dr. Chengcheng Yao, Dr. Xuan Zhang, Ms. Gengyao Li, Mr. Da Jiao, Mr. Fanbo Zhang, Mr. Lixing Fu, Ms. Huanyu Chen, Dr. Chen Yuan, Dr. Abrez Mondal, Dr. Hussam Khasawneh, Dr. Kexing Lai, Dr. Yu Liu, Dr. Haiwei Cai, Dr. Jianyu Pan, Mr. Will Perdikakis, Dr. Miao Wang, Mr. Yingzhuo Chen, Dr. Ziwei Ke, Dr. Han Xiong, Dr. Bining Zhao, Dr. Xuan Zhang, Dr. Xuan Wu, Ms. Xintong Lyu, Ms. Xiao Li, Ms. Xiaodan Wang, Mr. Yue Zhang, Mr. Yousef Abdullah, Ms. Danielle Meyer, Ms. Emily Reed, Mr. Rich Alexander, Mr. Ziran Gao, Mr. Christian Moya, Mr. Gonzalo Constante, Ms. Peimeng Guan, Ms. Chuning Luo, Dr. Yuanxin Li. The list can truly go on. Thanks for sharing this journey with me at OSU.

Most importantly, none of this would have been possible without the love and care of my family. My parents, Shixiang Mao and Ling Deng, have supported me, mentally and financially, through all these years. I would like to thank my dear wife, Shuyao Wang, for her continuous encouragement and support. All these family supports brought me the courage and strength to conquer the obstacles and setbacks during my Ph.D. study. I dedicate this dissertation to them.

Vita

October, 1990	Born - Changsha, Hunan, China
2013	B.S. Electrical Engineering, North China Electric Power University, Beijing, China
2015	M.S. Electrical Engineering, The Ohio State University
2015 - 2019	Ph.D. Electrical Engineering, The Ohio State University

Publications

Research Publications

D. Mao, J. Wang, J. Tan, G. Liu, Y. Xu and J. Li, "Location Planning of Fast Charging Station considering its Impact on the Power Grid Assets," 2019 IEEE Transportation Electrification Conference (ITEC 2019), 19-21 Jun. 2019.

Z. Gao, **D. Mao** and J. Wang, "Distribution Grid Response Monitor," IET Generation, Transmission & Distribution, vol. 13, pp. 4374-4381, 2019.

D. Mao, Z. Gao and J. Wang, "An Integrated Algorithm for Evaluating Plug-in Electric Vehicle's Impact on the State of Power Grid Assets," International Journal of Electrical Power and Energy Systems, 105:793-802, 2019.

D. Mao, K. Potty and J. Wang, "The Impact of Power-Electronics-Based Load Dynamics on Large-disturbance Voltage Stability," 2018 IEEE Power and Energy Society General Meeting (PESGM), Portland, OR, 2018.

D. Mao, D. Meyer and J. Wang, "Evaluating PEV's Impact on Long-Term Cost of Grid Assets," 2017 IEEE 8th Conference on Innovative Smart Grid Technologies (ISGT 2017), 23-26 Apr. 2017.

D. Mao, H. J. Khasawneh, M. S. Illindala, B. L. Schenkman and D. R. Borneo, "Economic Evaluation of Energy Storage Options in a Microgrid with Flexible Distribution of Energy and Storage Resources," 2015 IEEE/IAS 51st Industrial and Commercial Power Systems Technical Conference (I&CPS), Calgary, AB, 2015, pp. 1-7.

Fields of Study

Major Field: Electrical and Computer Engineering

Table of Contents

Page

List of Tables

List of Figures

Chapter 1: Introduction

1.1 Background and Motivation

Plug-in Electric Vehicles (PEV) have become increasingly popular in our daily traveling routine. PEVs use energy storage, usually in the form of battery banks, that are designed to be recharged using utility grid power [1]. The world has seen a myriad of benefits that PEV promise. They help us reduce greenhouse gas (GHG) emissions and our dependence on fossil fuels [2, 3]. They can lead us towards a more connected and environmentally friendly world. The development and promotion of PEV are essential to scale up the transition to electric mobility.

According to the International Energy Agency (IEA), the zero-emission mobility is expanding at a rapid pace. In 2018, the global PEV fleets exceeded 5.1 million, up 2 million from the previous year, and the worldwide PEV penetration target is 30% of total market share by 2030 (*i.e.,* EV30@30 Campaign) [4]. Country-specific market status and targets, shown in Table 1.1, further illustrate the continued push towards massive PEV adoption [4–9]. Technology advances and policy incentives continuously serve as the key enablers for such PEV penetration trend.

One obstacle of the massive PEV adoption is the *range anxiety*, which is a common phenomenon defined as the urge to charge PEV when its battery's State of Charge

Table 1.1: Global Leading PEV Market Status and Ambitions

Country	**New PEV Sales in 2018**	**Cumulative Sales through 2018**	**PEV Market Share**	**Penetration Targets**
USA	361,320	1123,370	2.45%	10% in 2025
China	1078,530	2306,300	4.48%	20% by 2025
Norway	72,690	249,000	46.42%	100% by 2025
Netherlands	29,160	148,490	6.57%	100% by 2035
UK	50,360	184,030	2.10%	100% by 2040
Japan	49,750	255,100	1.13%	30% by 2030

Note: Market share is based on the total market size of each country

(SOC) falls below a threshold. The charging accessibility, convenience, and efficiency greatly affect people's intention to own PEV. To address the range anxiety concern, fast charging infrastructure has been developed and deployed worldwide to further escalate the momentum for transportation electrification. Tesla has been developing a network of supercharging stations with power level up to 150 kW [10]. In Western Europe, since 2018, the joint venture Ionity has opened over 100 fast-charging stations toward its goal of 400 by 2020. At these stations, a PEV driver can stop for 15 to 45 minutes and recharge a vehicle as fast as its on-board charger permits, *e.g.,* all the way up to 350 kW [11]. China remains the world's largest PEV market in 2018, where the utility State Grid Corporation has paved the way for the charging infrastructure development and ambitious penetration target [12]. It can be seen that automakers, utilities, charging hardware manufacturers and other power sector stakeholders are all participating in boosting investment of fast charging infrastructure.

The assumed trajectory for the electric power grid decarbonisation effort is consistent with transportation electrification and further strengthens GHG emission reductions from PEV. When the power grid interacts with PEV through charging activities, it observes an unconventional type of load. PEV loads consume much higher power. Table 1.2 shows the charging levels, terminal voltages and connection configurations regarding current charging technology [13–15]. For example, at DC Level 2, it is possible to charge a 25 kWh battery pack in less than 10 minutes. This magnitude of power requirements far exceed the peak power demand for an average household in the U.S. Moreover, the Power Electronics-interfaced (PE-interfaced) configuration of PEV charger can ramp up to full charging power almost instantaneously. For example, it only takes 7 seconds for a 2016 Ford Focus Electric to reach its full charging power after connecting to the grid. Therefore, the PEV charging characteristics are of high power demand and impulsive.

Table 1.2: PEV Charging Level, Terminal Voltage and Configuration

Charging Level	**Terminal Voltage**	**Power per Vehicle**	**Charging Time**	**System Level Connection**
AC Level 1	120 V 1-phase	2 kW	10∼13 h	Residential/Commercial Secondary Customer 120 V and 240 V
AC Level 2	240 V 1-phase	20 kW	1∼4 h	
AC Level 3	240 V 3-phase	43.5 kW	∼1 h	
DC Level 1	200∼450 V	36 kW	0.5∼1.44 h	Commercial Primary/Secondary Customer 480 V
DC Level 2	200∼450 V	96 kW	0.2∼0.58 h	
DC Level 3	200∼800 V	200 kW	∼10 min	
Ultra-Fast Charging (UFC)	≥800 V	500 kW	∼Gas Refueling	Sub-transmission Primary Customer 26 kV or 69 kV

Note: Ultra-Fast Charging is not yet finalized

These charging activities add additional demand to a power grid that may be already struggling to meet its regular obligations, which present challenges. Both transmission system and distribution system can observe the loading stress induced by PEV charging in various effects. The transmission systems (above 138 kV) transport power from generating units to all the power delivery systems within its operation region. Distribution systems operate from 2 kV to 35 kV, delivering electricity from substations, which are connected to the transmission system. Power networks that are operated between 35 kV and the transmission voltage level (138 kV) are referred to as the sub-transmission level [16].[1] Accurately and efficiently assessing these charging impacts from both voltage levels plays a crucial role in managing the power grid and maintaining the operating reliability.

1.2 Literature Review

The charging impacts of high penetration of PEVs have been studied at both distribution and transmission voltage levels. At the distribution level, studies have been focused on residential charging and conventional commercial charging, ranging from 120 V to 480 V, as shown in Table 1.2 [17–19]. PEV charging impact is assessed in terms of charger modeling and load behavior characterization in [20–22], with results obtained by either hardware experiments or field measurements. In [23, 24], battery degradation protection strategy and associated costs are further considered when optimally coordinating the PEV charging schedules. Ref. [25, 26] investigate the charging impact on overall power quality, and in particular, voltage profile along

[1] The voltage level classification varies by operators, electric administrative regions, and countries.

the distribution feeder, considering uncertainties of charging patterns. Ref. [27] proposes a four-quadrant charger operation technique to properly manage the charging, satisfying feeder voltage and peak demand constraints. The design of coordinated charging strategies for impact mitigation has been presented in [28–30].

On aggregate of charging infrastructure and corresponding impacts, existing studies have focused on the interaction between PEV charging stations and the distributed generation (DG) as well as energy storage (ES) [31–35]. Furthermore, distribution expansion planning [36], maximum PEV penetration capability [37], and grid asset depreciation analysis [38], etc., have been studied under the scope of distribution level PEV charging impact.

At the transmission level, literature has assessed the aggregate of lower level PEV charging on their participation in electricity markets [39–41]. The frequency regulation [42, 43] and congestion management [44, 45] under PEV integration have been investigated as well. Furthermore, the charging coordination with DG [46], worst contingencies identification [47], and transmission expansion planning [48], etc., have been studied under the scope of transmission level PEV charging impact.

As illustrated in Section 1.1 and Table 1.2, the ambition of Ultra-Fast Charging (UFC) is to boost the charging speed to a level that is comparable to the traditional gas refueling. With such high-power requirements, the connection topology and configuration between fast charging infrastructure and the power grid requires adjustment. High-power demand may require a high connecting voltage level, necessitating UFC connections at the transmission/sub-transmission system instead of the traditional medium/low-voltage distribution system. Such a configuration is similar

to a large industrial load center of primary customer grade. So far, besides conceptual proposals and a few pilot projects, the feasibility, topology, and potential grid impacts of UFC have yet to be thoroughly studied.

1.3 Dissertation Structure

This dissertation focuses on the integration of PEV into the electric power system, where the grid impact analysis and corresponding charging infrastructure planning have been elaborated throughout the dissertation. The remaining of this dissertation is organized as follows.

Chapter 2 proposes an integrated algorithm for evaluating grid assets depreciation under high penetration of PEVs, which is a typical distribution level charging impact. The fidelity of the proposed method is demonstrated on a set of real-world power distribution networks. The results of the case study have been developed impact analysis and predictive planning software prototype in the chapter. This chapter also analyzes the mechanism and impact of dynamic loss of voltage stability under grid-side disturbances by studying a PEV-connected rudimentary system.

Based on the distribution level impact metrics developed in Chapter 2, Chapter 3 proposes a graph-computing based integrated location planning model for PEV fast charging stations (FCS). The proposed model considers the requirements for FCS in both aspects of power supply and transportation, thus guaranteeing reliable power grid operation as well as economic planning decisions. To ensure fast convergence of the planning process, the chapter further proposes a graph-based cross-entropy (CE) optimization algorithm, which enhances computational efficiency with graph parallel

computing technique. The integrated planning model and graph-based implementation have been validated on a synthetic network.

Chapter 4 takes the PEV' charging impact assessment to the transmission level and proposes a Graph-computing based Cascading Failure Evolution (G-CFE) analysis to predict potential cascading outages induced by Ultra-Fast Charging Station (UFCS) on power transmission systems. The proposed G-CFE model is the first effort to analyze PEV's disruptive impact on transmission power grids. The advantages of the proposed method is validated in a real-world provincial transmission system.

Finally, in Chapter 5, the contributions of this dissertation are summarized and future works are recommended.

Chapter 2: Distribution Level PEV Charging Impact

2.1 Introduction

As described in Chapter 1, the impact of high penetration of PEVs on the power grid has been studied at two voltage levels: distribution (below 26 kV) and transmission. In this chapter, we investigate the distribution level PEV charging impact.

Distinct from conventional electric loads, PEV loads are stochastic and *impulsive*, which means they are of high power density and vary in a fast and discrete manner. Prior works have shown that these load characteristics result in negative impacts on the power grid, including disruptively varying voltage profiles along the feeder and overloading of service transformers, etc. [14, 29, 49–52]. This will consequently affect the operating state of grid assets and induce lifetime depreciation over the long term. With increasing PEV penetration and improving fast/ultra-fast charging technologies, it is critical for electric utilities to accurately quantify the impact of PEV loads on grid assets and plan for equipment replacement and infrastructure expansion accordingly, to ensure service reliability.

Static analysis and Time-Series (TS) analysis have been utilized to assess grid assets' response under high penetration of PEVs. Most of the static analysis results in the consideration of maximum PEV loads induced by coincidental charging. For

example, [53] shows that the energy losses can increase up to 40% in off-peak hours and the investment cost can increase up to 15% of total distribution network costs for a scenario of 60% PEV penetration level. In [54], the case study shows that both peak-to-average ratio (PAR) and loss increment are big concerns to the widespread PEVs due to the coincidence of daily peak load and charging activities. The limitation of this approach is that only the worst cases are considered, and thus tend to overestimate the negative impact. Improving on this approach, other work, such as [55, 56], considers the probabilistic distribution of PEV loads connected in the system. In [55], Roulette wheel selection concept is used to take various uncertainties into account, thus quantifies the congestion and security risk impact of PEV in the form of probabilistic distribution functions. While these assessments allow more accurate input of PEV charging, an inherent deficiency of the static analysis is embedded from the assumption of fixed grid configurations. Hence, they cannot capture the inter-temporal response of grid assets. These deficiencies can be alleviated in TS analysis.

TS analysis feeds time-series load profiles to power flow analysis and monitors power grid's response. A few studies adopt TS analysis in PEV's impact assessment, under deterministic or stochastic settings. Ref. [56] simulated four PEV charging scenarios, considering stochastic nature in charging start time, and thus concludes that a 20% level of PEV penetration would lead to a 35.8% increase in peak load for uncontrolled charging scenario. However, the results of these studies do not naturally fulfill utilities' needs of quantifying the long-term cost induced by PEV. This is because (i) the existing studies are simulation-based, and thus the conclusions drawn

cannot be generalized to other power systems; (ii) TS analysis only shows the electrical response (*e.g.,* voltage, power, etc.), but grid asset depreciation could depend on response in other dimensions (*e.g.,* winding temperature, mechanical fatigue, etc.); and most importantly (iii) the load flow resulted from the TS analysis are taken in the form of annual average in the evaluation [57], which makes the impulsive charging characteristics invisible. In other words, the load spikes caused by PEV charging can be easily averaged off in the assessment and shown harmless, while they could greatly reduce the lifetime of the grid assets in reality.

Therefore, in this chapter, we propose an integrated algorithm that evaluates the temporal and multi-dimensional operating state of grid assets under the umbrella of TS analysis [38, 58]. The contributions of the proposed algorithm are twofold:

(i) It provides an approach to conveniently assess PEV's impact on grid assets. The PEV charging profiles are pre-processed through Monte Carlo Simulation (MCS), which ensures consideration of stochastic charging patterns, fed into TS analysis and asset lifetime estimation. The outputs are presented through an integrated interface.

(ii) Inter-temporal response of grid assets is considered. Compared to existing methods, which assess grid assets based on their average loading, the proposed algorithm considers assets' operating frequency and temperature variation. These factors could lead to significant differences in the assessment, as demonstrated in the numerical cases.

Following the charging impact evaluation algorithm, this chapter then establishes a new context where the power-electronics-based (PE-based) load, represented by PEV, dominates the total load composition in power distribution systems. Under the new context, the mechanism and impacts of voltage instability under large disturbances

have been analytically explored [59]. Finally, the chapter introduces a software prototype, wherein the author developed asset depreciation analysis module, that serves as an impact visualization tool and predictive planning guideline under the increasing PEV penetration [60].

Note that the response of grid assets is defined as the inter-temporal operating state change. Throughout the chapter, "grid assets" and "power delivery equipment" are used interchangeably. In addition, although the proposed algorithm can be applied to any power systems, we only examine its effectiveness in simple settings, where mitigation method on PEV charging is not applied.

2.2 Analytic Models of Integrated Evaluation Algorithm

The proposed integrated charging impact evaluation algorithm is outlined in Fig. 2.1. In general the algorithm combines time-series power flow (TSPF) analysis with off-line asset degradation impact assessment.

2.2.1 Total Cost of Ownership Analysis in Utility Practice

Grid assets can be classified into two categories based on their lifetime depreciation procedures: continuous loading equipment and discrete operating equipment. The former's depreciation rate depends on their thermal loading, while the latter's depends on the operating frequency. Examples are transformers, which depreciate faster under heavy loading, and voltage regulators (VR), which exhaust after operating for a certain number of times.

Total Cost of Ownership (TCO) analysis is commonly adopted by utilities to assess the long-term cost of the equipment, which accounts for the present value of capital cost and operating depreciation. The TCO of discrete operating equipment is

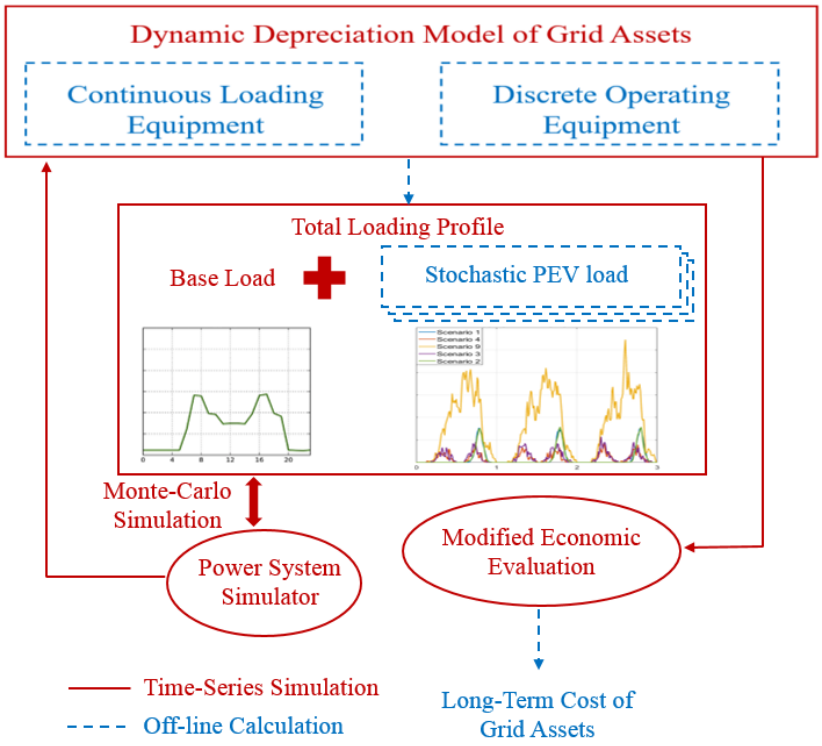

Figure 2.1: Workflow of Integrated Charging Impact Evaluation Algorithm

conventionally evaluated independent of loading conditions. For continuous loading equipment, its TCO is exemplified by a transformer and expressed as (2.1), with terms expanded in (2.2) - (2.5) [61]

$$TCO = C_o + CL \cdot A + LL \cdot B, \tag{2.1}$$

where C_o is the bid price (*i.e.,* capital cost) of the transformer, the rest of the terms are operating costs. CL, LL are transformer core loss and load loss in kW provided by manufacturers, A and B are core loss and load loss factor in $\$/kW$

$$A = DC + N \cdot PEC \tag{2.2}$$

$$B = (RF \cdot DC + LoF \cdot PEC) \cdot \hat{P}^2, \tag{2.3}$$

where DC represents the levelized hourly demand cost in $\$/kW-hr$, N is the total hours in the analyzing period, RF is the transformer responsibility factor indicating the relationship between transformer peak load and transformer load at the system peak time, $\hat{P}$ is the normalized peak loading, calculated as the ratio of peak loading to the transformer rating $\hat{s}/s_R$, PEC is the present value of energy cost in $\$/kWh$, which depends on the normal transformer insulation life T_{ins}, interest rate i, and energy cost EC

$$PEC = EC \cdot \frac{(1+i)^{T_{ins}} - 1}{i(1+i)^{T_{ins}}}, \tag{2.4}$$

and LoF is the transformer loss factor depending on the annual average loading s_{avg} of the transformer, calculated as

$$LoF = \gamma \frac{s_{avg}}{\hat{s}} + (1-\gamma)(\frac{s_{avg}}{\hat{s}})^2, \tag{2.5}$$

where γ is the dynamic load factor constant.

In (2.1), the last term $LL \cdot B$ models the depreciation induced from transformer loading. From (2.3) and (2.5), it can been seen that average annual loading is used to approximate the time-varying loading. This conventional assessment method can occasionally capture the long-term overloading [57]. However, they are incapable of capturing short-term overloading induced from impulsive PEV loads, because the "load spikes" of charging could be easily averaged off.

2.2.2 Grid Asset Depreciation Model (GADM)

Lifetime depreciation models of grid assets under the same category take similar forms. In this section, we present the dynamic models of transformers and VR to represent the continuous loading equipment and discrete operating equipment, respectively. These models are adopted to assess the equipment's temporal response in

the proposed algorithm. We also derive their corresponding Loss of Life (LoL) metrics. This Grid Asset Depreciation Model (GADM) and the subsequent re-established TCO evaluation serve as the core of the proposed impact evaluation algorithm.

Continuous Loading Equipment

The distribution transformer's lifetime depends on the internal winding hot-spot temperature Q_{HST}, which is directly related to the loading level $s(t)$ at each instant [62]. The dynamics of this thermal model has the following general form in terms of continuous time differential equations

$$\dot{Q}_{TO}(t) = f_1(\mathbb{E}^2[K(t)], Q_{TO}(t)) \tag{2.6}$$

$$\ddot{Q}_H(t) = f_2(\mathbb{E}^y[K(t)], \dot{Q}_H(t)) \tag{2.7}$$

$$Q_{HST}(t) = Q_{TO}(t) + \tau_H \cdot \dot{Q}_H(t), \tag{2.8}$$

where Q_{TO} is the top-oil temperature, $\mathbb{E}[K(t)]$ is the expectation of load factor $K(t) = s(t)/s_R$ at each instant obtained from distribution power flow analysis embedded with MCS, $\dot{Q}_H$ is the hot-spot temperature dynamic over top-oil, τ_H is the hot-spot temperature time constant, and y is the winding exponent power. The compact form of the dynamic system model of (2.6) - (2.8) can be written as a stochastic function of continuous loading level

$$\dot{Q}_X = f(Q_X, s(t)|\mu, \sigma) \tag{2.9}$$

$$Q_{HST} = a^T \cdot Q_X, \tag{2.10}$$

where $Q_X = [Q_{TO}\ \dot{Q}_H]$ and $a = [1\ \tau_H]^T$.

Then, the LoL for transformer L_T during any time span $[t_1, t_2]$ is derived as in (2.11). The transformer's expected lifetime T_x can be found by solving $L_T(0, T_x) = 1$.

$$L_T(t_1, t_2) = \frac{1}{T_{ins}} \int_{t_1}^{t_2} F_{AA}(t)dt, \tag{2.11}$$

where F_{AA} is the accelerated aging factor defined in (2.12) [63]

$$F_{AA}(Q_{HST}) = exp(\alpha - \frac{\beta}{Q_{HST}(t) + \Omega}), \tag{2.12}$$

where α, β and Ω are thermal constants of the transformer. When $F_{AA}(t) > 1$, the lifetime of the transformer is shortened at instant t.

Discrete Operation Equipment

Voltage regulator (VR) is essentially a type of tap changing transformer. In the power distribution system, VR are installed to regulate the voltage deviation to within predetermined range. Impulse loads, such as PEV, tend to cause time-varying and salient voltage deviation, which may result in more frequent tap operations. VR's lifetime is determined by its mechanical durability and specified as the total number of effective tap operations. The operation policy of VR can be expressed as follow

$$h(n) = \begin{cases} (V(n) - V_R) \cdot \frac{1}{\kappa}, & \text{if } V(n) \in [h_{min}, \underline{\epsilon}] \cup [\bar{\epsilon}, h_{max}] \\ h_{max}, & \text{if } h(n-1) + \Delta h(n) \geq h_{max} \\ h_{min}, & \text{if } h(n-1) - \Delta h(n) \leq h_{min} \end{cases}, \tag{2.13}$$

where $h(n)$ is the VR tap position at the n^{th} (discrete) instant and dependent on its nodal voltage magnitude $V(n)$ as calculated from power flow, V_R is the reference voltage magnitude, κ is the VR step-size, $[\underline{\epsilon}, \bar{\epsilon}]$ is VR's dead-band, and h_{max}, h_{min} are maximum and minimum tap position, beyond which the VR will be saturated.

By observing the change of tap positions triggered by voltage variation, the LoL of VR L_V during any time span $[n_1, n_2]$ can be obtained in (2.14), and the VR's lifetime

T_v can be estimated by solving $L_V(0, T_v) = 1$.

$$L_V(n_1, n_2) = \frac{1}{N_{op}} \sum_{n_1}^{n_2} |h(n) - h(n-1)|, \tag{2.14}$$

where N_{op} is the VR's empirical maximum number of tap operations.

Re-established TCO Evaluation

The outputs of TS analysis enable us to accurately assess the LoL of power delivery equipment in the grid with PEV loads during any time span of interest. In this section, we re-establish the TCO formulation for grid asset long-term cost assessment. For VR, the TCO can be simply expressed as

$$TCO^V(n_1, n_2) = L_V(n_1, n_2) \cdot C_o^V, \tag{2.15}$$

where $L_V(n_1, n_2)$ is specified in (2.14) and C_o^V is VR's capital cost.

For transformers, the TCO can be formulated as

$$\begin{aligned} TCO^T(t_1, t_2) =& L_T(t_1, t_2) \cdot C_o^T \\ &+ CL \cdot A(t_1, t_2) + LL \cdot B(s, t_1, t_2), \end{aligned} \tag{2.16}$$

where $L_T(t_1, t_2)$ is specified in (2.11) and other parameters are specified in Section 2.2.1. PEC in (2.4) is modified to reflect the future cost in $[t_1, t_2]$ to the present day value as

$$PEC = \frac{EC}{i}[\frac{1}{(1+i)^{t_1}} - \frac{1}{(1+i)^{t_2}}], \tag{2.17}$$

and the parameter LoF in (2.5) is modified to capture time-varying loading level under stochastic PEV charging patterns as

$$LoF(s, t) = \gamma \frac{\mathbb{E}[s(t)]}{\hat{s}} + (1-\gamma)(\frac{\mathbb{E}[s(t)]}{\hat{s}})^2. \tag{2.18}$$

In both (2.15) and (2.16), the first term reflects the capital cost of the equipment due to the accelerated depreciation resulted from extra PEV loading stress, while the other terms in (2.16) reflects the operating cost induced from stochastic TS load profiles. Therefore, the re-established TCO evaluation, with TS analysis and GADM, can accurately capture any overloading form.

2.3 Case Study of Integrated Evaluation Algorithm

To demonstrate the validity of the proposed algorithm, case studies of real-world distribution systems are carried out in this section. Simulation results of grid asset depreciation state and long-term cost evaluation are presented.

2.3.1 Test System Topology and Simulation Setup

The integrated methodology outlined in Section 2.2 has been applied to three large-scale power distribution systems in Columbus metropolitan area, Ohio. These three areas can be demographically categorized as in Table 2.1.

Table 2.1: Demographic Categorization of Power Distribution Systems

Community	Electric Service Area (km^2)	Connected Capacity (kVA)
Urban	2.820	16,793
Suburban	5.568	11,661
Rural	6.786	7,707

These areas have comparable amount of base load, *i.e.,* connected capacity. The electric circuit data obtained from American Electric Power (AEP) is originally formatted in CYME, a commercial-grade power system simulation software widely used by electric utilities. Due to the customized simulation setup and the need for flexible

PEV load integration, all data has been firstly converted to the format compatible in OpenDSS [64], an open-source power distribution system simulator. The entire algorithm hereafter is demonstrated with MATLAB and OpenDSS.

The topology of electric circuit from CYME and corresponding network atlas from Google Maps are shown in Fig. 2.2. The main feeder of power distribution circuit has been sketched in the map by black solid line and the locations of the substation for each area have been labeled by blue marker for illustrative purpose. The urban circuit has the longest main feeder and the highest density of sub-feeders throughout the network, whereas the suburban circuit has a relatively sparse distribution of sub-feeders, followed by rural circuit which has a simple tree topology and the lowest sub-feeder density.

In terms of load condition, the "base load" shown in Fig. 2.3 serves as the benchmark in the case study. It is recorded at the substation of each area in a 15-minute resolution for one year and assumed that no PEVs are connected in this benchmark case. In addition to circuit configuration, these three areas also differ in loading demographics. The urban and suburban circuits are mainly comprised of residential and commercial load type, whereas the industrial load type dominates the rural circuit. As shown in Fig. 2.3c, the envelope of the load profile in the rule area is stretched wider because some industrial loads are constantly running at their full capacity during the work time while completely off during the night, weekend, and holidays.

2.3.2 Simulated PEV Charging Scenarios

The total load at any location h in the network is the summation of the base load P_h^b and aggregated PEV load P_h^{PEV}, i.e., $P_h(t) = P_h^b(t) + \sum P_h^{PEV}(t)$. There

(a) Urban Area (b) Suburban Area (c) Rural Area

Figure 2.2: Topology of Power Distribution Systems

are multiple factors that collectively affect individual PEV's daily charging profile $P^{PEV}(t)$. In this case study, the following three typical aspects are considered: (i) charging level; (ii) battery capacity; and (iii) vehicle type.

For each aforementioned aspect, two specifications are assumed. The PEV can utilize "slow-charging" level $P = 19.2\ kW$, which is commonly used in residential household as expedited home charging level, or "fast-charging" level $P = 120\ kW$, which is a widely used DC public charging level exemplified by Tesla supercharger [13, 65]. The battery capacity are assumed to be either "short-range" $C = 40\ kWh$

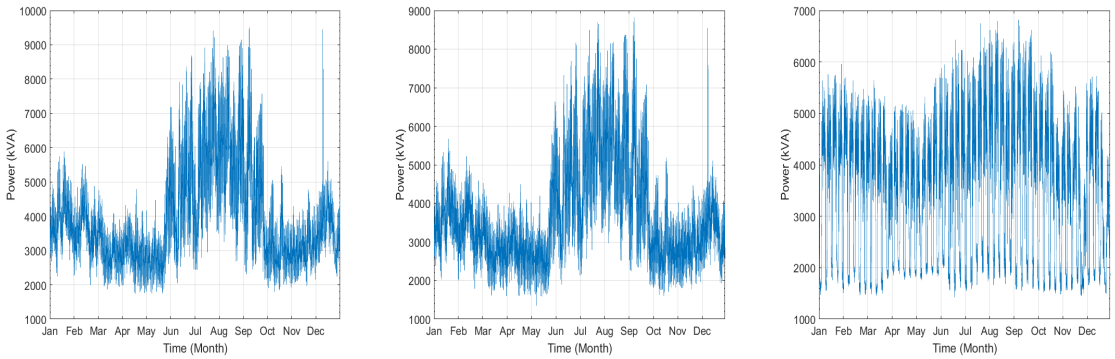

(a) Urban Area (b) Suburban Area (c) Rural Area

Figure 2.3: Yearly Profile of Base Load

or "long-range" $C = 60\ kWh$.[2] As for the vehicle type, we assume that the PEV is either used as commuter or as ride-service (*e.g.,* Uber, shuttle, cab, etc.).

The charging level and vehicle type collaboratively determine the stochastic PEV charging behavior, which is modeled by two random variables: the charging start time t_s and the charging period Δt. The latter is an explicit function of initial State of Charge (SOC) of battery at the beginning of charging action, given battery capacity C and charging level P, *i.e.,* $\Delta t = C \cdot (1 - SOC)/P$.

In terms of vehicle types, for the commuter who utilizes slow-charging, we assume that charging occurs immediately after getting back home from work, and the charging period Δt is determined by the mileage driven for daily commute. According to National Household Travel Survey [66], the individual commuter's departure/arrival time and daily driving mileage are assumed to follow Normal distribution. For the commuter who utilizes fast-charging, we assume that charging occurs either *en*

[2]The 2018 Nissan LEAF is equipped with 40 kWh battery pack and the 2018 Chevrolet Bolt EV is equipped with 60 kWh battery pack.

route to work or on the way home. Whether or not the vehicle charges *en route* is determined by a range anxiety threshold $\tau = 30\%$, as opposed to the slow-charging commuter case where every PEV charges at home every night. The ride-service type of PEVs will be driving for daily service from 7 am to 9 pm and charge *en route* whenever the SOC falls below the threshold τ. The average speed for different time in a day is used to formulate their multiple charging need [67]. Noted that the ride-service PEV is only considered to utilize fast-charging level and equipped with long-range battery due to the inherent requirement of vehicle usage.

From an aggregation point of view, it is assumed that each area studied has either 500 or 1000 PEV fleets in order to observe progressive impacts. The number of fleets simulated in this case study is consistent with the penetration goal set by the U.S. that every household owns a PEV in the future [68,69]. For some states such as California, the PEV penetration goal in coming decades has been even more aggressive, as almost 2 fleets per household [70,71]. Accordingly, the particular case of 500 and 1000 PEVs fall in the reasonable median of the PEV density. All simulated charging scenarios determined by aforementioned factors are summarized and indexed in Table 2.2.

The aggregated PEV charging profile of 500 fleets in a randomly selected 3-day period for all charging scenarios (viz. Table 2.2) is shown in Fig. 2.4. It can be seen that even though the slow-charging commuter has lower charging power individually, it's much easier for them to have coincidental charging than fast-charging commuter scenario due to the concentration of home charging events. Utilizing fast-charging level, the PEV only needs to recharge every 3-4 days and has a shorter period needed for each charging action. Moreover, the *en route* fast-charging actions have been split equally into departure and arrival charging, *i.e.,* the aggregated daily charging

Table 2.2: Summary of Simulated PEV Charging Scenarios

Vehicle Type	No. of Fleets	Charging Level	Battery	Scenario Index
Commuter	500	Slow-charging	Short-range	1
			Long-range	2
		Fast-charging	Short-range	3
			Long-range	4
	1000	Slow-charging	Short-range	5
			Long-range	6
		Fast-charging	Short-range	7
			Long-range	8
Ride-service	500	Fast-charging	Long-range	9
	1000			10

of fast-charging commuter has two spikes as compared to the single higher spike of slow-charging commuter. On the other hand, the fast-charging ride-service scenario reveals the most significant loading stress among all scenarios. Individual ride-service PEV will be charging *en route* multiple times (1∼4) during their service hours every day. The battery capacity imposes less influence on aggregated charging profile than the other two factors.

To truly reflect stochastic PEV charging patterns, Monte-Carlo Simulation (MCS) is implemented in TS analysis. The power flows in the grid are simulated in multiple iterations under total TS load profiles and are fed into the GADM simultaneously. The law of large numbers indicates that as the sample size gets sufficiently large, the expected value of model outputs can be approximated by taking the sample mean of the MCS output results. For example, the $\mathbb{E}[K(t)]$ in (2.6) and (2.7) is the *expectation* of load factor $K(t)$ at each instant obtained from averaging the power flow result over MCS iterations. In this case study, every charging scenario has been iterated 100

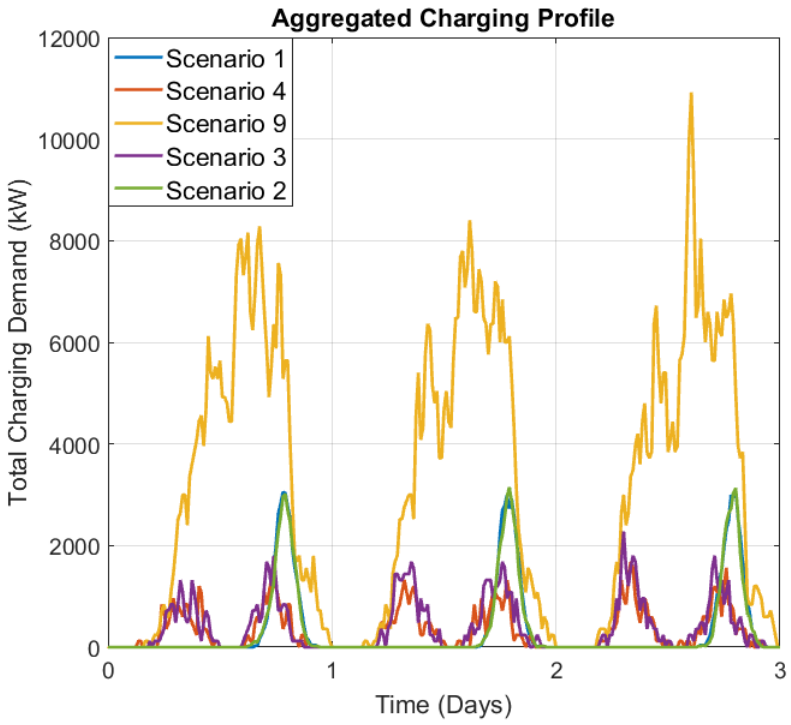

Figure 2.4: Aggregated PEV Charging Profile of Random 3-day Period

times in MCS, with 500 or 1000 PEVs' yearly charging profiles randomly allocated in the area each iteration.

2.3.3 Grid Asset Depreciation Analysis

Transformer Depreciation induced by PEV Charging

This section presents the lifetime depreciation evaluation of substation transformer induced by PEV charging. The thermal parameters related to transformer LoL estimation are collectively selected from [62,63,72]. Note that the substation transformers are assumed to have the same rating $s_R = 10\ MVA$ and thermal parameters in all three areas due to the lack of field measurement and *ceteris paribus* in the case study.

Moreover, the normal insulation life of substation transformer has been selected as 25% retained tensile strength $T_{ins} = 15.41$ yr $(135,000$ hr$)$ [62].

The transformer's accumulated LoL based on thermal model (2.6) - (2.11) are exemplified by Fig. 2.5, demonstrating two specific charging scenarios and benchmark case for all areas. The abrupt increase of degradation after 0.4 year in each one-year period is mainly attributed to the shape of base load as shown in Fig. 2.3. All three areas' base load have the similar pattern that the envelope of load curve starts to stretch upward in mid-May. As the simulated PEV load profile has no seasonal fluctuation, the total load profile pattern will be consistent with the base load. Hence, the degradation will start to speed up as it is highly related to the loading level.

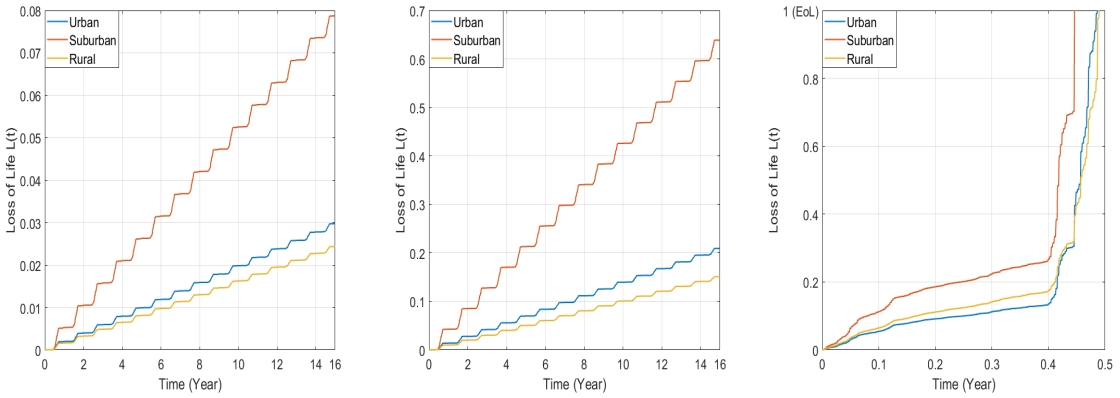

(a) Benchmark (b) Scenario 1 (c) Scenario 9

Figure 2.5: Accumulated Transformer Loss of Life

When the same charging scenario is applied to different demographic areas, it can be seen that the transformer in suburban area is the most prone to induce depreciation, followed by urban and rural area, thus revealing the grid's topological impact

under the same charging scenario. On the other hand, when different charging scenarios are applied to the same area, it can be observed that the ride-service type of PEV will induce more drastic burden to the asset than commuter type (cf. Fig. 2.5b & Fig. 2.5c). The utility must consider the upgrade of transformer to a higher rating. Otherwise, according to the GADM, the current 10 MVA transformer will endure an extremely high overloading burden that makes the transformer reach End of Life (EoL) within a year.

Fig. 2.6 provides a zoom-in look of LoL pattern in a one-year period, comparing benchmark with scenario 1 and 4. It can be seen that the rate of LoL, *i.e.,* the stiffness of LoL curve, is increased under impulsive PEV charging load, thus the lifetime of transformer is greatly shortened. Moreover, the scenario 1 has a more detrimental effect to transformer than scenario 4 does due to the concentration of home charging events.

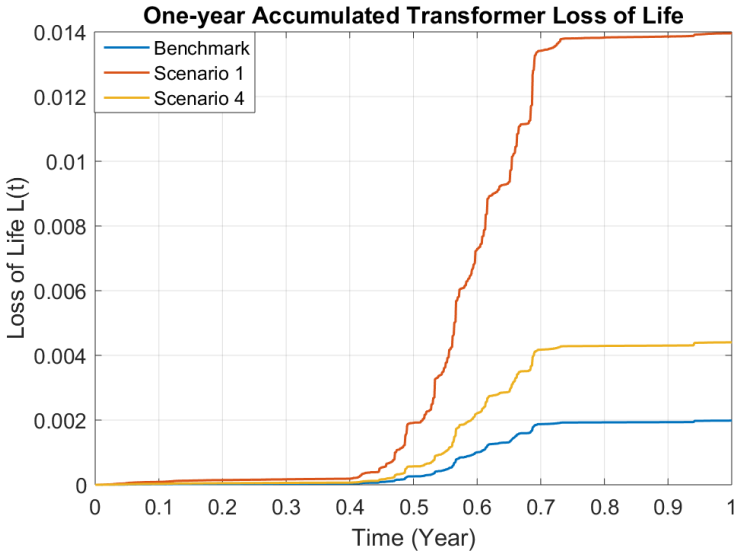

Figure 2.6: Zoom-in Look of One-year LoL in Urban Area

Table 2.3: Summary of Estimated Transformer Lifetime

Area	Charging Scenario Index	Yearly LoL (%)	Lifetime (yr)
Urban	Benchmark	0.19	15.41
	1	1.36	15.41
	2	1.18	15.41
	3	0.53	15.41
	4	0.43	15.41
	5	27.64	3.62
	6	19.69	5.08
	7	1.63 E+03	ε
	8	1.01	15.41
	9	1.05 E+03	ε
	10	1.82 E+06	ε
Suburban	Benchmark	0.51	15.41
	1	4.15	15.41
	2	3.58	15.41
	3	1.52	15.41
	4	1.31	15.41
	5	93.81	1.07
	6	66.26	1.51
	7	24.73	4.04
	8	2.98	15.41
	9	3.22 E+03	ε
	10	6.56 E+06	ε
Rural	Benchmark	0.16	15.41
	1	0.98	15.41
	2	0.86	15.41
	3	0.40	15.41
	4	0.30	15.41
	5	19.40	5.15
	6	13.80	7.25
	7	5.22	15.41
	8	0.74	15.41
	9	0.66 E+03	ε
	10	1.63 E+06	ε

The transformer depreciation evaluation of all simulated charging scenarios is summarized in Table 2.3. The Yearly LoL indicates the percent loss of life regarding

normal insulation life T_{ins} per year, thus the estimated lifetime can be obtained as 100/(Yearly LoL). If this value is longer than 15.41 yr, then the corresponding charging scenario is considered to have no noticeable impacts on transformer. On the other hand, there are several charging scenarios for each area that will greatly reduce transformer's lifetime. For certain drastic case such as ride-service type of PEV charging, the estimated lifetime can even be shortened to $\varepsilon < 0.5$ yr, which shows an urgent need for the upgrade of equipment. All charging scenarios that impose such salient impact on transformer lifetime and thus considered to be unacceptable for utilities are marked in shade in the Table 2.3.

Note that the LoL is very sensitive to the transformer rating and certain thermal parameters, thus the estimated lifetime under each charging scenario only falls in a ballpark range, depending on the accuracy of selected parameters. Therefore, in addition to considering the estimated lifetime as an absolute reference, utilities could compare the charging scenario's relative LoL with each other, due to the consistent pattern of LoL for all simulated charging scenarios.

Voltage Regulator Depreciation induced by PEV Charging

This section presents the state evaluation of VR induced by PEV charging. We assume that there are two three-phase VRs installed at midway through the feeder in each area. The step-size of VR tap is selected as $\kappa = 0.0065$. The yearly simulation monitored their tap operations. Fig. 2.7 shows the tap operation in a randomly selected 10-day period for urban area, comparing the VR operating frequency regarding number of PEV fleets with the benchmark. The temporal response of VR is strongly correlated with PEV daily charging activities. Moreover, the increasing number of

PEV causes greater voltage deviation and more salient TS load profile, thus induce more frequent VR tap operations.

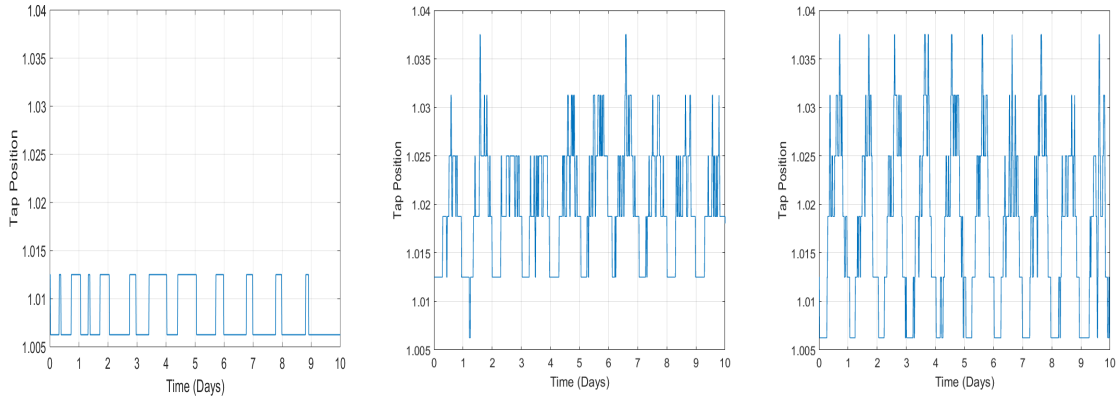

(a) Benchmark (b) Scenario 9 (c) Scenario 10

Figure 2.7: VR Tap Operation of Random 10-day Period in Urban Area

Fig. 2.8 shows the total counts of VR tap operations under multiple scenarios for each area with 500 PEV fleets. The inherent unbalanced loading of distribution system causes the different number of tap operations annually for each phase of VR. More importantly, it reveals an insightful observation that the VR operation is highly affected by the impulsiveness of charging activities. Admittedly, Scenario 1 has a higher loading impact due to concentrated home charging actions, however, Scenario 4 has a higher impact on VR operations due to the more frequent charging activities (cf. Fig. 2.4). The subsequent LoL of VR can be derived based on (2.14). It indicates a consistent pattern of lifetime depreciation as in Fig. 2.8.

Note that the two three-phase VRs successively installed at the middle of feeder share the burden of voltage adjusting requirement under highly impulsive PEV loads.

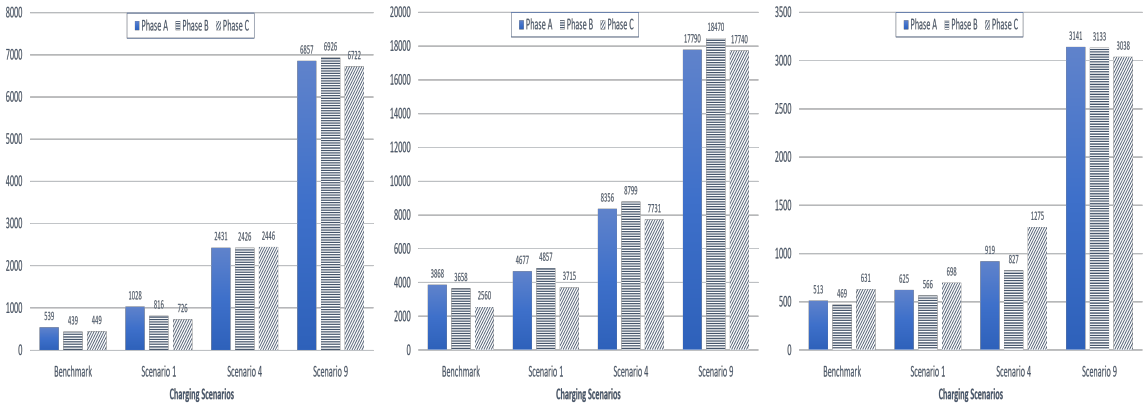

(a) Urban Area (b) Suburban Area (c) Rural Area

Figure 2.8: Number of Tap Operations Per Year

The more VRs installed in the system, the more controllability of the voltage profile is available in real time, but meanwhile induce more capital investment. The utility is facing more challenges with the current trend of increasing PEV penetration when dealing with such trade-off [73, 74].

2.3.4 Effect of Demographics on Asset Depreciation

All previous case studies exclude the demographic discrepancy embedded in different areas, and only consider one charging scenario at each simulation. This section serves as an extended case study to particularly analyze the demographic impact on grid assets, where we have mixed charging scenarios at each simulation. The comparing metrics have been modified as follows. For each area, the PEV penetration level (PL) is defined as the ratio of coincidental charging load to the total base load.

$$PL = \frac{\sum P^{PEV}}{P^b} \times 100 \tag{2.19}$$

The three areas have different percent composition of slow/fast-charging PEV based on their demographic nature, as shown in Table 2.4. Note that in this study we assume that the percentage of fast-charging (120 kW) PEV is in descending order of suburban (highest), urban, and rural area (lowest). This assumption is justified by the fact that the suburban area has the highest possibility for PEV to utilize *en route* fast-charging facility.[3] Hence, it is expected that the power grid in suburban area will be exposed to the most impulsive and drastic PEV load, which induces the most depreciation and long-term cost for the grid assets.

To observe progressive impact, multiple PL scenarios, *i.e.,* benchmark (no PEV), 50%, 100%, 200% and 300%, are investigated. Same reasoning mentioned in Section 2.3.2, the setup and upper bound of PL is set based on the scenario that every household owns a PEV, which is predicted realistic in the near future. Note that this study does not intend to draw an exhaustive conclusion for various charging and penetration scenarios, but rather, to propose an integrated algorithm that helps utility interpret PEV's impact. Based on (2.19) and Table 2.4, the detailed number of PEV fleets for slow-charging and fast-charging can be determined respectively, which in total make up the PL of interest.

Table 2.4: Percent Composition of Two Charging Levels

	Slow-charging	Fast-charging
Suburban Area	60%	40%
Urban Area	70%	30%
Rural Area	80%	20%

[3]For example, the only Tesla Supercharging Station currently built in Columbus is not located in downtown (urban area), but in Grove City (suburban area).

The long-term cost of transformer is estimated with the modified method described in Section 2.2.2 and compared with the conventional TCO formulation described in Section 2.2.1. The results are compared over normal lifetime T_{ins}. If the transformer is exhausted at $T_x \leq T_{ins}$ due to the extra stress imposed by PEV loads, then a new transformer is purchased and its induced cost (capital cost and operating cost) is added to the total cost. The parameters associated with TCO evaluation of the substation transformer are obtained from an anonymous vendor and in [61], as summarized in Table 2.5.

Table 2.5: TCO Parameters and Specifications

Parameters	**Value**
s_R [MVA]	10
CL [kW]	13.2
LL [kW]	53
DC [$/kW-yr]	120
RF	0.81
EC [$/kWh]	0.05
γ	0.2
i [%]	5
C_o [$]	70,000
Evaluation Period [yr]	15.41

The TCO of transformer in suburban area estimated with two methods are shown in Fig. 2.9. It can be seen that the results of both methods indicate that the long-term cost of the transformer is greatly increased with increasing PL. Moreover, results are very close at low PL, and when PL is greater than 200%, the proposed method assesses much higher long-term cost than conventional TCO. This difference in trend is attributed to the fact that substation transformers are usually over-sized for reliability concerns. Therefore, a relatively low PL is not likely to cause a noticeable

adverse impact on transformer operation. However, when the grid hosts more PEV, the impact can only be captured accurately with the proposed TCO method.

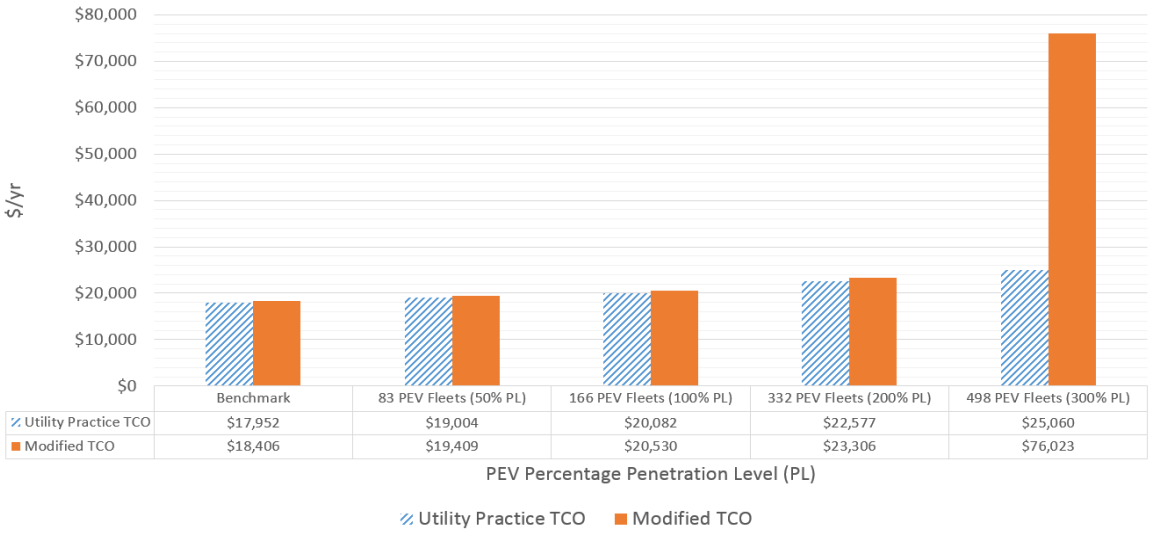

Figure 2.9: TCO of Transformer in Suburban Area

In this case, the derivation of PL is based on a proportion of electric load in each area, which gives us a relatively conservative estimation of charging impact. For example, under 300% PL, the suburban area will have 498 fleets in total, which could likely be an understatement considering the case study results in Section 2.3.3. But still, we can observe a $\sim 5\%$ accuracy improvement of cost estimation as compared to current utility practice for the lower PL case and a $30\% \sim 40\%$ accuracy improvement for the more drastic PL cases.

A further question to ask is whether it is more reasonable to use a transformer with larger rating under high PL, which will essentially bring the results of the two methods to the same values. The answer could be case dependent. For example, sometimes a larger transformer could cost more than replacing a small transformer

after its end of life, while other times the reverse is true. Nevertheless, even if the planning strategy might conceal the inaccuracy of the conventional TCO method, the fidelity of the proposed method is demonstrated at every PL. Moreover, the proposed method enables evaluation of equipment long-term cost over any time span of interest, which provides great flexibility to utilities' planning work.

2.4 Impact of PEV Charger Dynamics on Voltage Stability

2.4.1 Motivation

Following the charging impact evaluation algorithm in Section 2.2 - 2.3, this section then establishes a new context where the power-electronics-based (PE-based) load, represented by PEV, dominates the total load composition in a power distribution system. In the new context, we explored the mechanism and impacts of voltage instability under grid-side large disturbances.

Voltage instabilities have been well studied in literature with both static and dynamic approaches [75–77]. The static approach is based on power flow equations, estimating if the system is stable, and deducing the stability margin through voltage-reactive power sensitivity, eigenvalues of the power flow Jacobian and continuation power flow (CPF) techniques [75, 78]. The dynamic approach considers system dynamics induced by physical devices, such as generators, induction motors and self-restoring loads. The analysis techniques under dynamic approaches include time-domain simulation, linear/nonlinear system theories, etc. [79]. Note that the term "static" is inspired by the steady-state analysis tool, *i.e.,* power flow. Nevertheless, the voltage stability analysis is dynamic by nature, as the driving force of voltage instability is the load's dynamic attempt to restore power consumption.

Hence, thorough studies have been conducted regarding the load-driven mechanism of voltage instability, either in generic forms of nonlinear models with first-order dynamics of voltage dependent loads, or in specific forms derived for individual devices (*e.g.,* induction motor) [80,81]. The application of singular perturbation theory made possible the decomposition of entire system dynamics into two widely separate time scales [82], as shown in (2.20) and (2.21), enabling great simplification when corresponding analysis techniques have been applied.

$$\dot{x_S} = f_S(x_S, x_F) \tag{2.20}$$

$$\varepsilon\dot{x_F} = f_F(x_S, x_F), \tag{2.21}$$

where, x_S, x_F are vectors of slow and fast variables, respectively, and the system is separated into a slow subsystem (2.20) and fast subsystem (2.21) due to small parameter ε.

The transient response for the impedance network is very fast compared to the slower dynamics of load-driven voltage instability, and thus can be formally eliminated by setting $\varepsilon = 0$. This approximation has reformed dynamic properties of the system, as (2.21) degenerates into the algebraic equation (2.22), which is also the equilibrium condition for the fast subsystem (2.21).

$$0 = f_F(x_S, x_F) \tag{2.22}$$

Equations (2.20) and (2.22) constitute the Differential-Algebraic (D-A) system. In particular, for a long-term characteristic component such as a load tap changer (LTC), the time-scale decomposition simplifies the analysis through the quasi-steady-state (QSS) approximation by assuming all short-term dynamics, including synchronous generator, induction motor, etc., operate at equilibrium. This singularly perturbed

model is shown in (2.23) - (2.25) [81].

$$\dot{z_c} = h_c(x, y, z_c) \tag{2.23}$$

$$0 = f(x, y, z_c) \tag{2.24}$$

$$0 = g(x, y, z_c), \tag{2.25}$$

where, without loss of generality, (2.23) models the long-term dynamics of continuous state variables z_c, (2.24) refers to the equilibrium condition of short-term dynamic states x through singular perturbation, and (2.25) denotes the steady-state condition of network (*i.e.,* power flow) for algebraic states y.

The fundamental assumption for this time-scale decomposition is that when grid-side large disturbances (*e.g.,* loss of a line or generation) are imposed, the response of electromagnetic transients on the impedance network always settle fast enough and are stable. Thus, before a disturbance, the grid operation point can be found by intersecting the Constant Power Load (CPL) characteristic curve with the network $P-V$ characteristics, as shown in Fig. 2.10. Post disturbance, the network characteristic shrinks drastically due to the change of network topology. Thus, the CPL curve no longer intersects the post-disturbance network $P - V$ curve, indicating voltage instability [81].

However, as an ongoing trend, the landscape of power system loads has been significantly altered by the power-electronics-based (PE-based) load, in particular, PEV, gradually dominating the total load composition. The inherent high-bandwidth control of PE-based loads makes the assumption, on which the singular perturbation analysis is based, no longer valid. The dynamics of PE-based loads belong to neither long-term nor short-term characteristics regarding conventional time-scale decoupling,

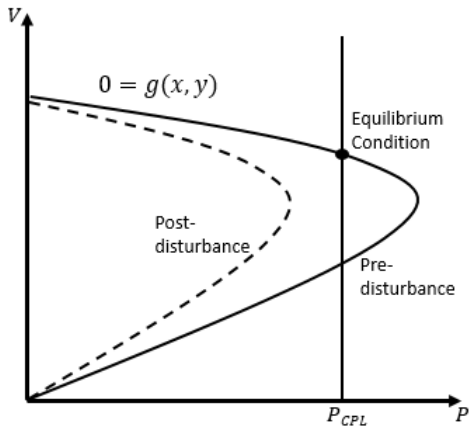

Figure 2.10: $P - V$ Curve Demonstration of Voltage Instability

but fall into one that is comparable to a network's instantaneous response. Therefore, we must resort to component-level analysis to evaluate grid-side response under large grid disturbance.

As the first step toward studying the voltage stability under this new context, this section investigates the interaction between a large grid-side disturbance and PEV charger load, which is modeled with a representative PE structure. This work demonstrates voltage instability induced from PE-based load response to grid-side disturbance. Furthermore, it proposes a technique for estimating the Region of Attraction (ROA) of stable equilibria, which implies a critical clearing time for disturbance [83]. Despite the exemplification with a rudimentary system, the proposed technique can be extended to analyze power grids of a greater scale.

2.4.2 Modelling of PEV Charger and Dynamic Analysis

System Configuration

Appropriate dynamic modeling of PEV loads is critical to study the voltage instability mechanism induced by large disturbances and to design preventive actions at component level. The PE structure within the charger is generally comprised of a cascaded system, which contains a grid-connected converter (AC/DC Rectifier), a load-side converter (DC/DC Converter) and a battery [84]. Such integrated configuration, as a whole, is designed to have constant power consumption at the load side regardless of input variations. Moreover, despite the reactive compensation requirement in certain applications, the high bandwidth PE controller generally ensures pure active power absorption from the grid with unity power factor. The system configuration is shown in Fig. 2.11.

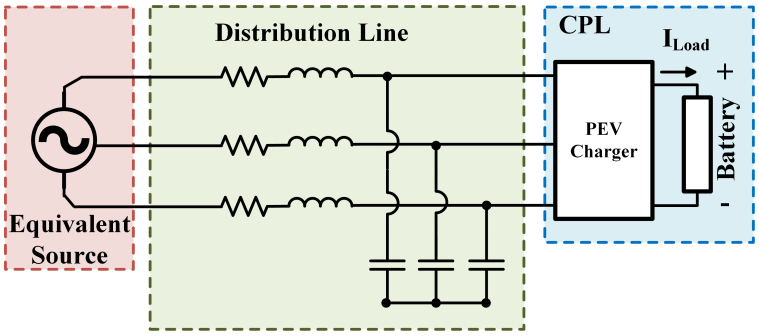

Figure 2.11: System Configuration

Dynamic System Modelling

The CPL characteristics are embedded with AC three-phase grid-connected system. A baseline model has been adopted, combining source and line dynamics with

an infinite bandwidth CPL in order to simulate a PEV charger's short-term characteristics [85]. The system equivalent circuit in dq frame is shown in Fig. 2.12.

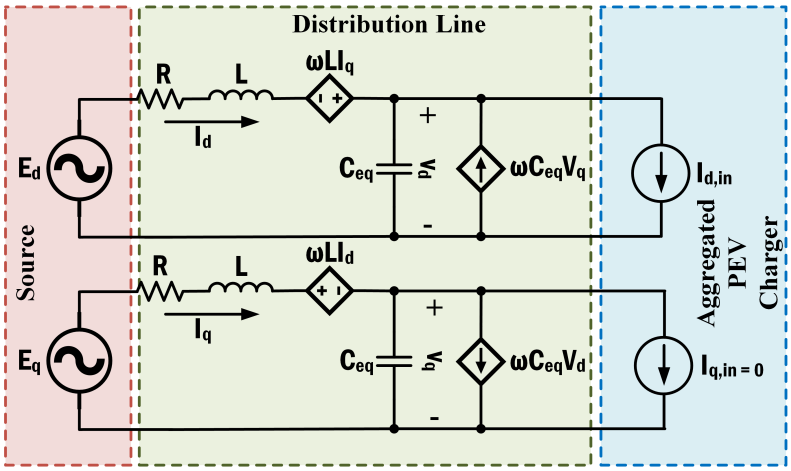

Figure 2.12: System Equivalent Circuit in dq Frame

The abc-to-dq transformation has been widely used in stability analysis of PE-based interface [86]. It makes all phase quantities fixed with each other, thereby leading to constant self and mutual inductance. Hence, it reduces the complexity of AC grid-connected load system analysis and allows the whole system to be analyzed in a DC manner. The three-phase power consumption of a PEV charger is expressed in (2.26). For convenience, we assume no q-axis current going through charger $I_{q,in} = 0$, *i.e.,* the charger is regulated at unity power factor. This assumption does not affect the conclusions of the analysis, and can be relaxed in the augmented form of (2.32).

$$P_{PEV} = \frac{3}{2} V_d I_{d,in} \tag{2.26}$$

Under the equivalent circuit, the system state-space model of an AC grid-connected PEV charger is

$$\dot{\mathbf{x}} = f(\mathbf{x}, \mathbf{u}, \mathbf{p}), \tag{2.27}$$

where $f : D \mapsto \mathbb{R}^4$ is continuously differentiable and $D \subset \mathbb{R}^4$ is a domain that contains the equilibrium point of (2.27) $\mathbf{x}^* \in \mathscr{E} := \{\mathbf{x}^* \in D : f(\mathbf{x}^*) = 0\}$.

By KVL and KCL, the detailed model is given in (2.28) - (2.31).

$$\dot{I}_d = -\frac{R}{L} I_d + \omega I_q - \frac{1}{L} V_d + \frac{E_d}{L} \tag{2.28}$$

$$\dot{I}_q = -\omega I_d - \frac{R}{L} I_q - \frac{1}{L} V_q + \frac{E_q}{L} \tag{2.29}$$

$$\dot{V}_d = \frac{1}{C_{eq}} I_d - \frac{2P_{PEV}}{3C_{eq} V_d} + \omega V_q \tag{2.30}$$

$$\dot{V}_q = \frac{1}{C_{eq}} I_q - \omega V_d, \tag{2.31}$$

where the system state variables are line currents and load voltages $\mathbf{x} = [I_d \; I_q \; V_d \; V_q]^T$, the input variables $\mathbf{u} = [E_d \; E_q \; P_{PEV}]^T$ are grid (source) voltage and charger demand, and the system parameter set is $\mathbf{p} = \{\omega, \; R, \; L, \; C_{eq}\}$ where ω is the line frequency, R, L are line resistance and inductance, respectively, and C_{eq} is the equivalent capacitance representing combined shunt capacitance and charger's dynamic effects.

The state Jacobian matrix of this highly-coupled, high-dimensional dynamic system can be expressed in (2.32).

$$J = \frac{\partial f}{\partial \mathbf{x}} = \begin{bmatrix} -\frac{R}{L} & \omega & -\frac{1}{L} & 0 \\ -\omega & -\frac{R}{L} & 0 & -\frac{1}{L} \\ \frac{1}{C_{eq}} & 0 & \frac{2P_{PEV}}{3C_{eq}V_d^2} & \omega \\ 0 & \frac{1}{C_{eq}} & -\omega & 0 \end{bmatrix} \tag{2.32}$$

The distribution systems are characterized by their high R/X ratio [87]. For instance, for a 12 kV distribution line the ratio could be larger than 10. Under this

circumstance, we can approximate the reactance $X = \omega L \approx 0$ due to the line damping effect $\tau = R/L = R/(X/\omega) = R\omega/X > 10\omega$. Hence, the hereafter analysis is based on the decoupling assumption. Moreover, since the charger is operating in unity power factor (*i.e.,* d-axis dominant), we assume that d-axis states (V_d and I_d) are the main states, which dictate the major dynamics of the system, whereas q-axis states (V_q and I_q) are independent elements that are coupled to each other but decoupled from active elements. Through this decoupling, the dynamic analysis can be conducted in the planar system $g : D \mapsto \mathbb{R}^2$ and the reduced model can be written as

$$\dot{V_d} = -\frac{2P_{PEV}}{3C_{eq}V_d} + \frac{1}{C_{eq}}I_d \tag{2.33}$$

$$\dot{I_d} = -\frac{1}{L}V_d - \frac{R}{L}I_d + \frac{E_d}{L}, \tag{2.34}$$

where the state variable set becomes $\mathbf{x} = [V_d \ I_d]^T$, input variables $\mathbf{u} = [E_d \ P_{PEV}]^T$, and $\mathbf{p} = \{R, \ L, \ C_{eq}\}$.

The corresponding reduced Jacobian matrix is expressed as

$$J_r = \begin{bmatrix} \frac{2P_{PEV}}{3C_{eq}V_d^2} & \frac{1}{C_{eq}} \\ -\frac{1}{L} & -\frac{R}{L} \end{bmatrix}. \tag{2.35}$$

Dynamic System Analysis

The static stability of the operating condition can be obtained by observing the spectrum $spec(J_r)$ of (2.35) evaluated at a specific parameter set $\mathbf{p}^*$ and equilibrium point $\mathbf{x}^* \in \mathscr{E} := \{\mathbf{x}^* \in D : g(\mathbf{x}^*) = 0\}$. The sufficient condition for a particular loading value P_{PEV} to be stable is such that $spec(J) \subset \mathbb{C}^- := \{\lambda \in spec(J) \cap \mathbb{C} : \ \Re[\lambda] < 0\}$. Hence, it is possible to find a demand upper bound P_{PEV}^{max} and to identify the closeness of the current operating point to the voltage collapse point [88].

However, the above linearization-based approach is limited to analyzing the local stability at the equilibrium point. It can neither assess the robustness of equilibrium, nor predict the system behavior when (2.32) becomes ill-conditioned. To understand the finite stability of the system, we have the following proposition.

Proposition. *The structure of three-phase charger dynamics determines that the system exhibits unstable limit cycle* $\Gamma(\mathbf{x}_0) = \{\mathbf{x} \in D : \ \mathbf{x} = \Phi_t^g(\mathbf{x}_0), \ t \in [0, +\infty]\}$, *where* $\Phi_t^g(\mathbf{x}_0)$ *is the flow of the state space model* $\dot{\mathbf{x}} = g(\mathbf{x}, \mathbf{u}, \mathbf{p})$ *passing through initial condition* $\mathbf{x}_0$. *The interior of this limit cycle implies a Region of Attraction (ROA)* $\mathcal{A}$ *of a Locally Asymptotically Stable (LAS) equilibrium, where* $\mathcal{A} := \boldsymbol{int}(\Gamma(\mathbf{x}_0)) = \{\mathbf{x}_0 \in \mathbb{R}^2 : \ \lim_{t\to\infty} |\mathbf{x}(t, \mathbf{x}_0)| = \mathbf{x}^*\}, \ \forall \mathbf{x}^* \in \mathscr{E} \ s.t. \ \mathbf{x}^*$ *is LAS.*

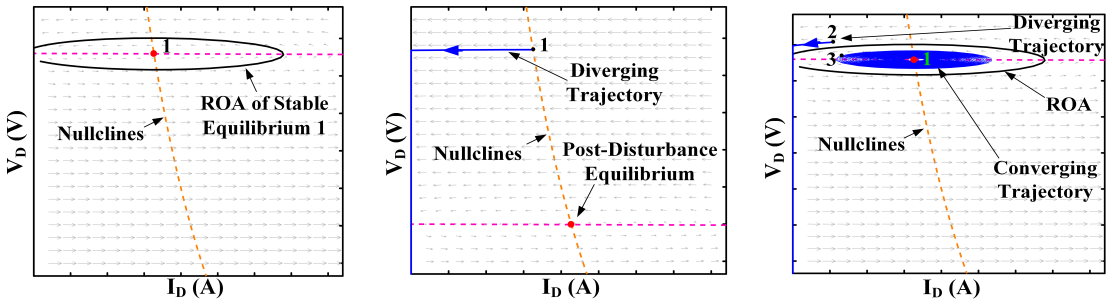

(a) Pre-Disturbance Stable Operation (b) Post-Disturbance Unstable Operation (c) Trajectory Interaction with ROA

Figure 2.13: Phase Portrait Analysis

The ROA $\mathcal{A}$ of an initial pre-disturbance stable equilibrium is an open, connected and invariant set bounded by unstable limit cycle, as shown in the illustrative phase portrait Fig. 2.13a, where for any initial operating condition (I_{d0}, V_{d0}) starting inside the ROA, the system trajectory will spiral toward the stable equilibrium point 1.

Suppose the system undergoes a large disturbance that makes the post-disturbance equilibrium unstable, then the original stable equilibrium point 1 becomes the initial condition for the new unstable system. This causes the trajectory devolving away, as shown in Fig. 2.13b. When the system is restored to original stable operation through fault-clearing, whether or not the trajectory converges depends on where the system operating point is when fault-clearing occurs. For example, as shown in Fig. 2.13c, if the fault is cleared when diverging state trajectory reached point 2 (outside ROA), then it diverges away; on the other hand, if the fault is cleared at point 3 (within ROA), the state trajectory will converge back to the stable equilibrium 1 and the fault-clearing is successful.

The proposition is confirmed through bifurcation diagram analysis as shown in Fig. 2.14, obtained by simulating a system with the following parameters also used throughout Section 2.4.3: $R = 0.0064\ \Omega$, $L = 1.698\ \mu H$, $C_{eq} = 29.333\ \mu F$, $E_d = 392.125\,V$, $P_{PEV} = 19200\,W$. These values were selected to make the initial operating condition start at LAS equilibrium and be realistically consistent with short-line distribution-connected PEV charger model as described in Section 2.4.2.

In the bifurcation diagram, as parameter P_{PEV} varies, the stable state (I_d or V_d) branch is denoted by the thick solid curve, and an unstable branch by the thin curve. Changes in stability occurs at the bifurcation point, where the stability of an equilibrium is lost through its interaction with a limit cycle. The unstable limit cycle exists prior to bifurcation, shrinks and eventually disappears as it coalesces with a stable equilibrium at bifurcation point. Afterwards, the equilibrium becomes unstable, resulting in growing oscillating instability. This series of phenomenon falls in the case of subcritical Hopf Bifurcation (HB). The circles emanating from the Hopf

bifurcation point yield an estimation of maximum magnitude of unstable limit cycle under a specific value of P_{PEV}.

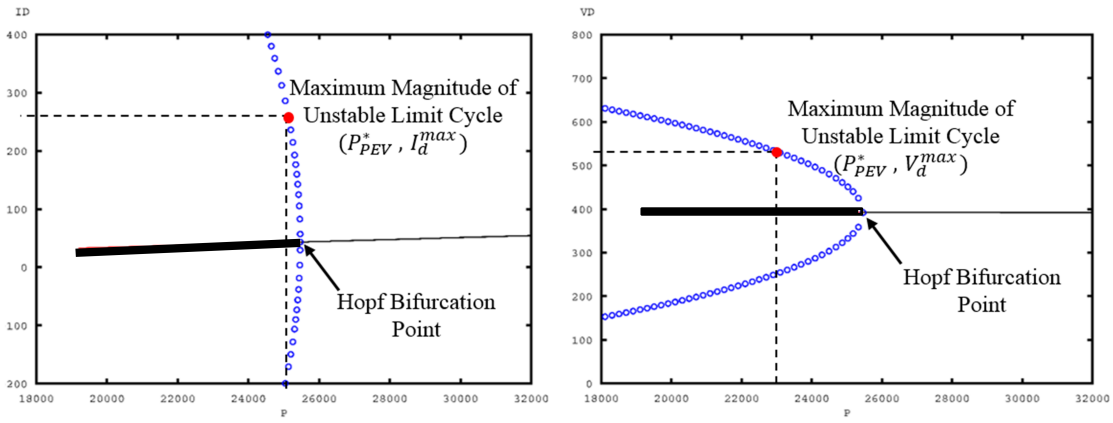

(a) I_d vs. P_{PEV} (b) V_d vs. P_{PEV}

Figure 2.14: Bifurcation Diagram of Parameter P_{PEV}

The validation of HB is reflected in the reduced state Jacobian J_r as in (2.35). In particular, the HB occurs when a pair of complex conjugate eigenvalues lies exactly on the imaginary axis. However, the HB analysis provides more information than standard linear stability theory because it also considers the effect of non-linearity and predicts oscillatory instability through limit cycle interaction. Therefore, such bifurcation analysis is best thought of as a supplementary tool that helps to explain the form of the instability when the stable equilibrium is lost.

2.4.3 Simulation of Charger Response to Grid Disturbance

In the time-domain analysis, the ROA implies a critical fault clearing time, after which the state trajectory originating from the pre-disturbance stable equilibrium have already drifted out of ROA and are not able to converge. Note that the ROA

and trajectories are assumed to be bounded in first quadrant $(I_d, V_d) \subset \mathbb{R}_+$ based on the assumption that the power flow is unidirectional, *i.e.,* from source to PEV charger.

The occurrence and clearance of grid-side large disturbance could be a tripping and ensuing re-closing of the generation/transmission equipment or sudden incremental aggregation of consumption. In particular, two scenarios have been considered as large disturbance in this simulation: (A) sudden source voltage drop, which means a decrease of input variables E_d and E_q; (B) power demand surge, which means an increase of input variable P_{PEV}. The system response under disturbance has been simulated through MATLAB.

For both scenarios, the disturbance occurs at $t = 0.05\ s$ and is cleared at t_{clear}. The three-phase line voltage and current response for scenarios (A) and (B) have been observed in Fig. 2.15 and Fig. 2.16, respectively. In scenario (A), the fault clearing times are selected at $t_{clear} = 0.085\ s$ and $t_{clear} = 0.15\ s$, respectively. As observed in Fig. 2.15a, both voltage and current resume pre-disturbance values after a certain tolerable perturbation. However, when the fault clearing has been delayed to $t_{clear} = 0.15\ s$, the line state will exceed the acceptable range, as shown in Fig. 2.15b, which will trip the protection in the charger. Such dynamic loss of stability implies that the critical clearing time for scenario (A) is within the range $t_{cr}^A \in (0.085, 0.15)s$. Similar implication has been observed for scenario (B), with $t_{cr}^B \in (0.068, 0.08)s$.

Estimation of the critical clearing time is more complicated and will be detailed in future works. A general direction is to integrate searching algorithms with the Boundary Controlling Unstable (BCU) Equilibrium Point method [89]. The system's energy functions can be constructed at the closest and farthest unstable equilibria,

respectively, corresponding to the inner and outer perimeters of the ROA. A searching algorithm, *e.g.,* bisection method, can be applied with the starting points defined as the spheres of the two energy functions to estimate the critical clearing time.

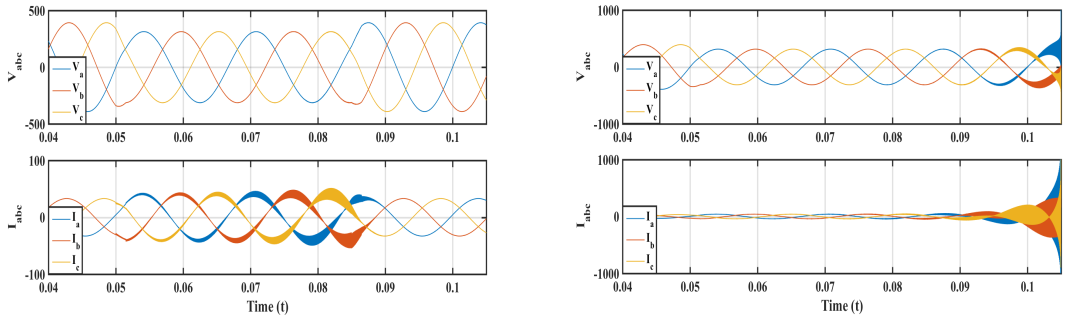

(a) Stable Response when $t_{clear} = 0.085\ s$ (b) Unstable Response when $t_{clear} = 0.15\ s$

Figure 2.15: Critical Clearing Time Implication for Scenario (A)

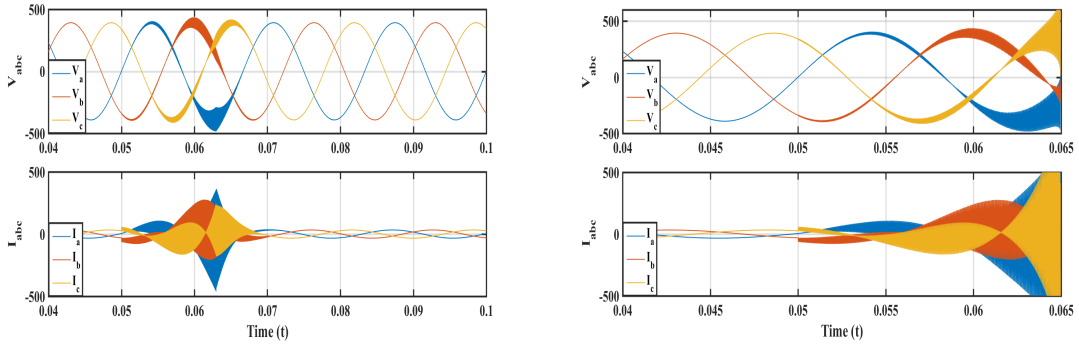

(a) Stable Response when $t_{clear} = 0.068\ s$ (b) Unstable Response when $t_{clear} = 0.08\ s$

Figure 2.16: Critical Clearing Time Implication for Scenario (B)

2.5 Distribution Grid Response Monitor

In this section, we introduce a software prototype, Distribution Grid Response Monitor (DGROM), which serves as a charging impact visualization tool and predictive planning guideline under the increasing PEV penetration [67]. Fig. 2.17 shows the system architecture of this software. The prototype is developed in MATLAB Graphic User Interface (GUI), OpenDSS, and CYME. The GUI takes user's data inputs. The Power System Definition module generates the comprehensive power grid model using the input data of PEV charging, base load, and the grid configuration. In particular, the PEV Definition module derives PEV charging patterns and profiles based on the criteria as illustrated in Section 2.3.2. This data is reformatted for the Time-Series Power Flow (TSPF) analysis in prediction of the charging effects.

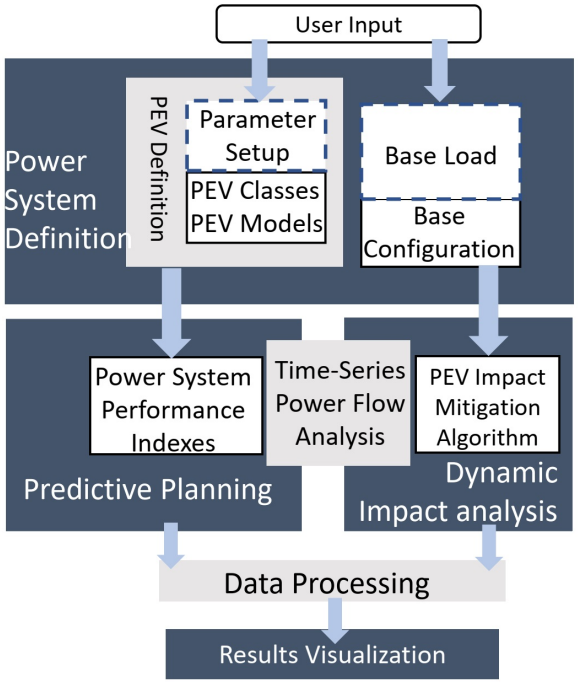

Figure 2.17: Architecture of Software Prototype

The GADM, predictive planning, and visualization modules then process the TSPF results, generate the impact metrics and provide mitigation strategy. All functional modules of DGROM are demonstrated in Fig. 2.18. To facilitate a customized input requirement, multiple alphabetical string analysis algorithms have been implemented in the developing phase. Distinct from related studies, DGROM assesses the impact of PEVs by considering multiple charging characteristics (*e.g.,* driving habits, charging stations, PEV types, etc.) and their interactions. Moreover, DGROM provides a range of predictions for infrastructure upgrading requirements in the distribution grid.

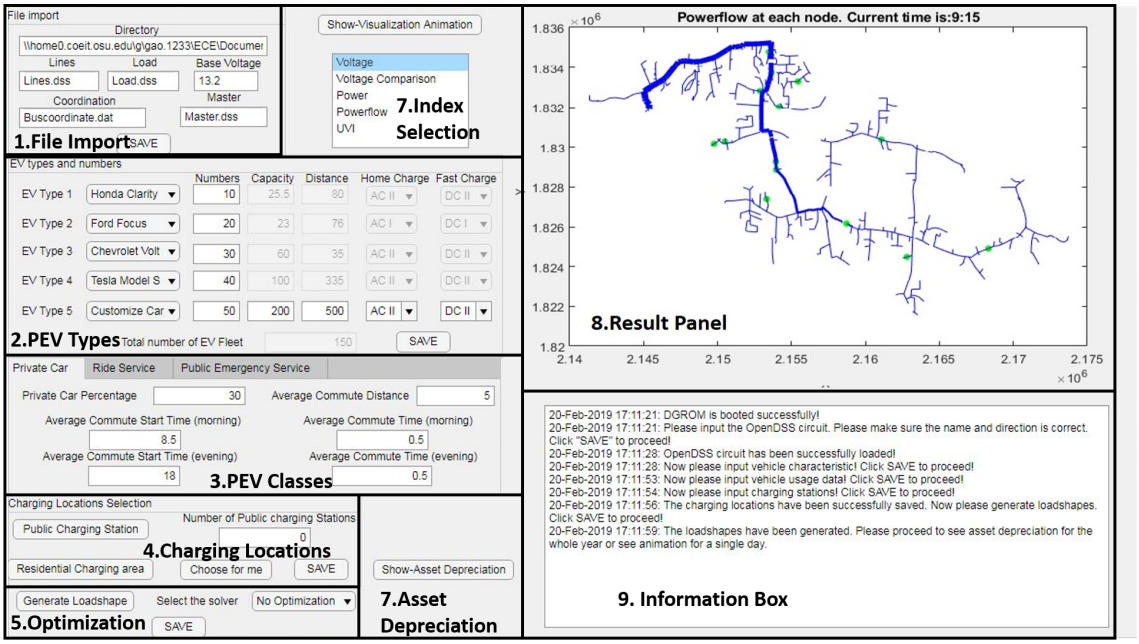

Figure 2.18: Dashboard of Software Prototype

2.6 Summary

With constantly increasing PEV penetration and improving fast charging technologies, it is critical for utilities to quantify the impact of PEV charging on grid assets and plan for equipment replacement or infrastructure expansion to ensure service reliability. The unique impulsive characteristics of PEV loads make conventional assessment methods of load impact unsuitable. To address this challenge, this chapter proposes an algorithm for evaluating grid assets depreciation under high penetration of PEVs. Compared to the existing evaluation methods, which are case-specific or static, the proposed algorithm provides convenient assessment through an integrated interface and is capable of capturing the inter-temporal response of grid assets. In addition, TS analysis and MCS are deployed to ensure the algorithm's accurate and robust performance by accounting for the random charging patterns over time and space. The results of the case study have been developed impact analysis and predictive planning tools for utilities.

Following the charging impact evaluation algorithm, this chapter establishes a new context where the PE-based load, represented by PEV charger, dominates the total power consumption. By studying a PEV-connected rudimentary system, we analyze the mechanism and impact of dynamic loss of voltage stability under grid-side disturbances. The Region of Attraction (ROA) of the stable equilibrium condition is estimated through nonlinear system theories, which implies a critical clearing time for grid disturbance. This implication is demonstrated through time-domain simulation.

Chapter 3: Location Planning of PEV Fast Charging Infrastructure

3.1 Introduction

With the development of battery and charging technologies, the auto industry has envisioned the ability to recharge PEV at speeds that are comparable to the traditional gas refueling. In addition, multiple charge ports are built in a cluster, bringing total power draw in a Fast Charging Station (FCS) to $1 \sim 6\ MW$ (estimated parking $4 \sim 12$ vehicles). Pilot projects aiming to bring FCS to passenger vehicles have been undertaken worldwide. For example, Porsche installed a prototype 350 kW, 800 V FCS at their Berlin office in July 2017. Tesla rolled out its 250 kW V3 supercharger in early 2019, with 1 MW backend infrastructure splitting to 4 charging stalls.

Promotion of these fast charging infrastructure can mitigate range anxiety and facilitate long-distance travel by PEV [90]. On planning the increasing penetration of FCS, two key aspects are taken into considerations in existing studies: power supply and transportation. On the side of power supply, FCS planning should consider the reliability requirement of the existing distribution grid, operation, and capital

costs [14, 91–93]. Capacity sizing and economic evaluation of on-site distributed generation or energy storage for the infrastructure have been considered in FCS planning paradigm as well [94, 95]. Further complications might be introduced by PEV's impulsive loading characteristics, end users' stochastic charging behaviors, and battery degradation [22, 24, 96–98]. On the side of transportation, as a capital-intensive infrastructure in the transportation network, the siting of FCS must allow for complete and efficient travel service [99]. In addition, the estimation of individual mobility of PEV drivers under a fine spatiotemporal resolution has been considered in the planning paradigm [100].

While those works have addressed the aspects of power supply and transportation separately, FCS location planning requires simultaneous consideration of both aspects. Ignoring either aspect could lead to sub-optimal economic decisions, even transportation or power grid operation problems. For example, locating an FCS close to the head of the feeder may minimize power delivery losses. However, this location may be less accessible to PEV drivers due to geographic constraints. A few literature have studied the problem in such an integrated manner. For example, [101] and [102] have incorporated the investment and operational cost of FCS considering traffic constraints in their planning models. In [103], FCS planning has the twin objectives of maximizing the number of visits of PEV and minimizing voltage deviation. In [104], a two-stage stochastic programming is formulated to minimize investment and operational cost by siting FCS jointly with on-site photovoltaic (PV), under PEV driving range constraints in the highway network. The integrated planning scheme in [105] further considered the permissible waiting time and service radius of FCS, thus strengthened the transportation network constraints.

The results of these studies, nevertheless, cannot quantify the long-term impacts of massive FCS because (i) They only considered the direct cost of charging facilities while ignoring the induced cost of its supporting power supplying infrastructure. (ii) The interaction of the transportation and power grid dynamic responses and their operational requirements are overlooked. (iii) The planning results are limited to small-scale scenarios [105–107]. No computationally efficient methods are available to guarantee converged solutions in large-scale FCS planning problems.

To address the above limitations, in this chapter, we propose a graph-computing based integrated location planning model, which maximizes PEV charging convenience while ensuring the power grid's reliability. In addition, the proposed work captures PEV's charging impacts on long-term costs of critical grid assets [108]. The contributions of this work are threefold:

(i) Proposed a graph modeling scheme for power and transportation coupled network integrated with PEV trip chains. Its representation of different entities' relationship allows for a) fast and easy model establishment; b) efficient implementation of distribution power flow; and c) flexible model extension under expanding networks and increasing PEV penetration.

(ii) The inter-temporal response of grid assets is considered in the power aspect of the proposed model, which enables the evaluation of critical equipment' long-term cost over any time span of interest.

(iii) The proposed planning model and cross-entropy (CE) solving method are implemented in a graph-computing platform, in which the Node-based Parallel Computing (NPC) technique has been applied to improve computational efficiency.

This chapter assumes that the power grid operates in the steady-state. The dynamic response of grid assets is defined as the inter-temporal state change. In addition, the mitigation methods against PEV's negative impacts, such as coordinated charging, are out of the scope of this work. Finally, the "distribution system" and "power grid" are used interchangeably throughout the chapter.

3.2 Integrated FCS Location Planning Model

3.2.1 Workflow

The workflow of the integrated location planning model and graph-based solving implementation is shown in Fig. 3.1.

The program is initialized with all possible combinations of FCS candidate locations (*i.e.,* 2^n, where n is the number of all candidate locations), one of which represents a FCS placement strategy. Those combinations are sampled with a predetermined distribution, and only a subset of them (*e.g.,* M combinations) are analyzed for their costs. Given one sample of FCS placement strategy, the Flow Capturing Module (FCM) calculates the capital cost and captured charging volume, and meanwhile, generates the charging profiles at each station. Next, Time-Series Power Flow (TSPF) analysis is performed using the total load, composed of charging profiles and the base load. The output from the TSPF containing the power grid inter-temporal response are fed to the Grid Asset Depreciation Module (GADM) to estimate the long-term costs of grid assets (*e.g.,* the transformer and voltage regulator cost). Hence, this grid asset cost, representing cost of power supply, and the FCS cost and revenue, representing transportation cost, are integrated together as the total cost.

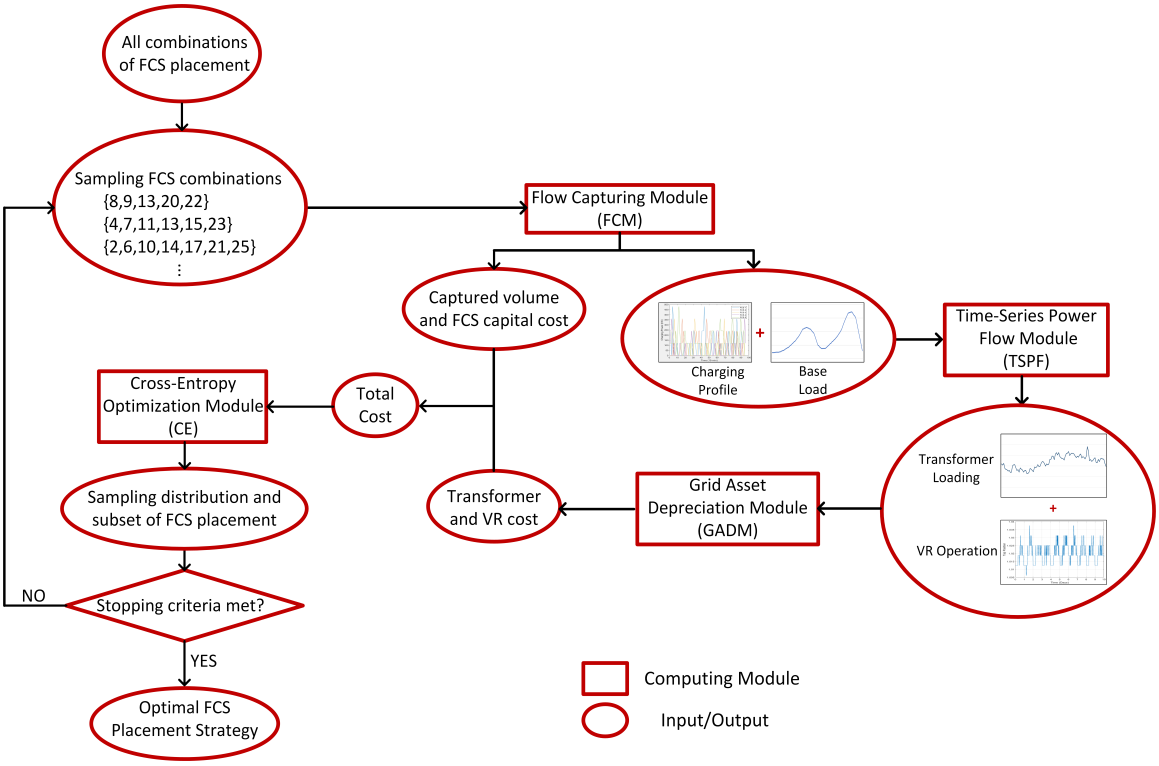

Figure 3.1: Workflow of Location Planning Model

The total costs are obtained for all the samples of FCS placement strategies and fed to the Cross-Entropy (CE) optimization module, which ranks the strategies by cost and generates a sampling distribution associated with top-ranked strategies. If the outputs of CE meet the stopping criterion, we have identified the optimal FCS placement. Otherwise, the FCS combinations are sampled again with the new distribution obtained, and the process repeats.

The computing modules, *i.e.,* FCM and CE, are elaborated in the Section 3.2.3 and Section 3.3. The other two modules, *i.e.,* Time-Series Power Flow (TSPF) and Grid Asset Depreciation Module (GADM), are adopted from Chapter 2, thus the detailed elaboration is omitted in this chapter.

3.2.2 Power Aspects

Chapter 2 has shown that the impulsive and high-power characteristics of PEV charging, especially when aggregated at FCS level, induce rapid variations to voltage profiles along the distribution feeder and overload transformers more frequently. These effects cause detrimental impacts to the grid's operating status and long-term cost of its assets. The power aspects in FCS location planning, from utilities' point of view, are aiming at accurately quantifying the impact of increasing PEV charging on these critical assets and coordinating the replacement as well as expansion, to ensure grid service reliability. We adopted the GADM and re-established TCO analysis proposed in Chapter 2, Section 2.2.2 as the power supply considerations, which are integrated with the transportation requirements in Section 3.2.5.

3.2.3 Transportation Aspects

One of the key considerations for FCS location planning in transportation aspect is the charging accessibility. Flow Capturing Model (FCM) is commonly employed to locate urban service facilities, such as gas stations and retail facilities. Given a departure time, an average speed of each road segment, and an origin-destination pair (O-D pair), the trip chain of a PEV is determined and timestamped by a common rationale such as the shortest distance route. If this trip chain passes through a FCS, it is considered *being captured*. Therefore, for a set of candidate FCS, we can evaluate the total captured traffic volume as the number of trip chains captured. In this work, the proposed planning model does not consider posterior impacts of charging facilities. That is, the typical driving rationales (*e.g.,* shortest distance, minimum traveling time, toll avoidance, etc.) determine the routes; the locations of FCS do

not alter the routes but only capture the routes. The FCM is integrated with power supply requirements and consideration of PEV owner's range anxiety in Section 3.2.5. We omit the full implementation details of FCM and refer to [109, 110].

3.2.4 Power-Transportation Coupled Network Modeling

The graph computing is based on the Graph Database (GDB) that applies semantic queries with vertices, edges, and attributes to store data in a graph structure [111]. As its data structure counterpart, the traditional Relational Database (RDB) uses a collection of interlinked tables (join tables) to store the structured records and relational interconnections [112]. GDB structure is suitable for modeling the pairwise relationship between objects in a network. It allows for efficient data retrieval, processing, and storage as well as a flexible model extension under expanding networks with increasing PEV penetration. For this reason, we adopt a graph-based network approach in the FCS planning to model the power grid and transportation network. The model is detailed below.

Denote the power network by a collection of vertices and edges, which forms an undirected graph $\mathcal{G}_{\mathcal{P}} = (\mathcal{V}_{\mathcal{P}}, \mathcal{E}_{\mathcal{P}})$, where $\mathcal{V}_{\mathcal{P}}$ is the vertex class of distribution nodes, and $\mathcal{E}_{\mathcal{P}} \subseteq \mathcal{V}_{\mathcal{P}} \times \mathcal{V}_{\mathcal{P}}$ is the edge class of distribution line segments. The node and line related information are stored as "attributes" of vertices and edges in the graph model. For example, a simple radial distribution system is shown in Fig. 3.2. The three-phase node voltage magnitudes, phase angles and connected load configuration are three typical sets of attributes associated with $\mathcal{V}_{\mathcal{P}}$. Each line segment between node i and j, denoted by $e_{i,j} \in \mathcal{E}_{\mathcal{P}}$, is characterized by the attributes of resistance $z^r_{i,j}$, reactance $z^i_{i,j}$, capacity $\overline{P}_{i,j}$, etc.

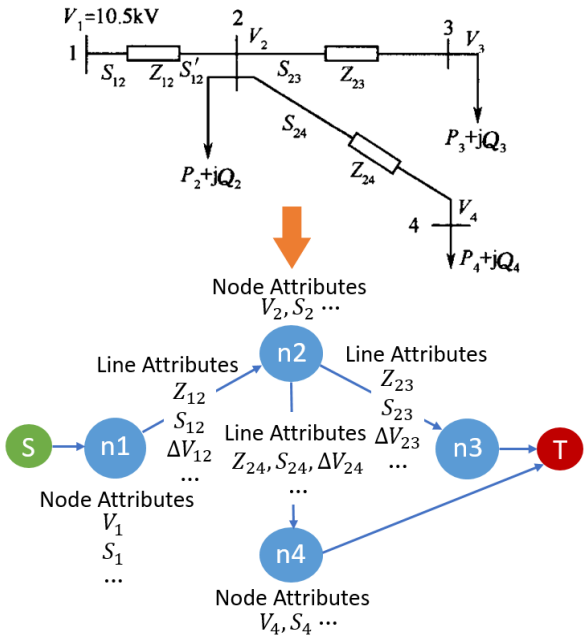

Figure 3.2: Graph Formulation of Distribution Feeder

To accelerate the data processing and computation, a Node-based Parallel Computing (NPC) technique was developed based on the work in [113, 114]. The NPC performs local computation at each node of $\mathcal{V}_\mathcal{P}$ by forming the 3×3 generalized line matrices for distribution power flow (DistFlow) analysis [115] and storing them as node attributes simultaneously.

The transportation network can be similarly modeled as a graph structure $\mathcal{G}_\mathcal{T} = (\mathcal{V}_\mathcal{T}, \mathcal{E}_\mathcal{T})$, where $\mathcal{V}_\mathcal{T}$ is the vertex class of transportation nodes, and $\mathcal{E}_\mathcal{T} \subseteq \mathcal{V}_\mathcal{T} \times \mathcal{V}_\mathcal{T}$ is the edge class of road segments. Individual PEV's information, including their intermediate location on trip chains, are stored as attributes in a special class, $\mathcal{V}^{PEV} \subset \mathcal{V}_\mathcal{T}$. Furthermore, the mapping between two networks can be established through an additional edge class, $\mathcal{E}^* \in \mathcal{E}(\mathcal{V}_\mathcal{P}, \mathcal{V}_\mathcal{T})$, which connects the geographically "overlapping"

distribution nodes and transportation nodes. Fig. 3.4b illustrates the graphic presentation of the power and transportation network, wherein the red dash lines represent $\mathcal{E}^*$. Therefore, a complete description of the coupled network is written as $\mathcal{G} = \mathcal{G}_\mathcal{P} \cup \mathcal{G}_\mathcal{T}$.

3.2.5 Putting it All Together

Integrating the cost functions proposed under the graph-based model, the FCS planning problem is elaborated as below. For conciseness, all the time variables, based on which the power flow is formulated, are omitted without causing ambiguity.

The objective function is the summation of the direct cost of FCS installation, its induced revenue, and long-term cost on the power grid assets.

$$\begin{aligned} \underset{\mathbf{x},\mathbf{y}}{\text{minimize}} \quad & c_1 \sum_{k \in K} x_k - c_2 \sum_{q \in \mathcal{E}_q} f_q y_q \\ & + \sum_{m \in M} TCO_m^T(s_m) + \sum_{l \in L} TCO_l^V(V_l) \end{aligned} \tag{3.1}$$

The first term in (3.1) stands for the installation cost of FCS. c_1 is the coefficient of FCS capital cost. The sole decision variable in the formulation is x_k, which indicates the placement of FCS, as

$$x_k = \begin{cases} 1, & \text{a FCS is placed at } k \\ 0, & \text{otherwise.} \end{cases} \qquad \forall k \in K \subseteq \mathcal{V}_\mathcal{T} \tag{3.2}$$

where K is the set of candidate FCS locations.

The second term in (3.1) is the induced charging revenue. Coefficient c_2 transforms the captured traffic volume into the monetary income. We consider a PEV is captured by a FCS if (i) the FCS is accessible to a PEV, and (ii) the PEV's State of Charge (SOC) is low enough, which is estimated by *range anxiety.* The accessibility of PEV

to FCS are represented by y_q, which is an auxiliary variable dependent on x_k. It equals to 1 if and only if the trip chain q passes through a FCS, written as

$$y_q = \begin{cases} 1, & \text{if } x_k = 1 \text{ and } q(k,\cdot) \neq \varnothing \\ 0, & \text{otherwise.} \end{cases}$$
$$\forall q \in \mathcal{E}_q \subset \mathcal{E}_{\mathcal{T}} \tag{3.3}$$

where $\mathcal{E}_q$ is the set of pre-determined PEV trip chains, $q(k,\cdot) \neq \varnothing$ indicates that k is a node on trip chain q.

Remark 1. The times of a trip chain passes through FCS is not cumulative. That is, $y_q = 1$ even if there exists multiple nodes $k = k_1, ..., k_n$ and $x_k = 1$ for k on q.

To model the effects of range anxiety, f_q is introduced. Range anxiety is a common phenomenon defined as the urge to charge PEV when its battery's SOC falls below a threshold [110]. f_q is the number of PEVs traveling on trip chain q, which hits range anxiety, calculated as

$$f_q = \sum_{p \in p(\cdot,q)} Ra_p \tag{3.4}$$
$$Ra_p = \begin{cases} 1, SOC_p \leq \tau \\ 0, \text{otherwise.} \end{cases} \qquad \forall p \in \mathcal{P}, q \in \mathcal{E}_q$$

where $\mathcal{P}$ is the set of PEV, Ra_p is the range anxiety indicator of the pth PEV, $p(\cdot, q)$ are set of PEV on trip chain q, SOC_p is the pth PEV's SOC, and τ is the PEV owner's range anxiety threshold.

To estimate SOC_p in (3.4), we assume that each PEV begins its daily trip with a full battery capacity C in kWh. The SOC when PEV starts charging can be obtained as

$$SOC_p = 1 - D_p/R_p, \quad \forall p \in \mathcal{P} \tag{3.5}$$

where D_p is the mileage driven when pth PEV arrived at any FCS, R_p is the maximum range of the PEV determined by battery capacity C_p. D_p is estimated in FCM as described in Section 3.2.3. Thus, the charging duration T_p can be calculated as

$$T_p = \frac{C_p(1 - SOC_p)}{P_p^{PEV}}, \quad \forall p \in \mathcal{P} \tag{3.6}$$

where P_p^{PEV} is the charging power for a given vehicle model. T_p is used together with timestamped trip chains to model the nodal power as detailed in (3.10).

The third and fourth term in (3.1) represent the long-term cost on the power grid. TCO^T and TCO^V are daily TCO of substation transformers and VRs. They are functions of the apparent power s_m and nodal voltage V_l, respectively, as defined in (2.16) and (2.15). M and L are the sets of transformers and VRs, representing the continuous loading equipment and discrete operating equipment, and $M, L \subset \mathcal{V}_\mathcal{P}$.

The apparent power of transformer m can be calculated as

$$s_m = (P_m^2 + Q_m^2)^{1/2} \tag{3.7}$$

$$P_m = \sum_{i \in (\mathcal{V}_\mathcal{P} < m)} P_i^A + P_m^{loss} \tag{3.8}$$

$$Q_m = \sum_{i \in (\mathcal{V}_\mathcal{P} < m)} Q_i^o + Q_m^{loss} \tag{3.9}$$

In (3.8) and (3.9), the summation is carried over nodes at the downstream of transformer m, *i.e.*, $i \in (\mathcal{V}_\mathcal{P} < m)$. Q_i^o is the base load reactive power at node $i \in \mathcal{V}_\mathcal{P}$, and P_i^A is the aggregate load at node $i \in \mathcal{V}_\mathcal{P}$, calculated as

$$P_i^A = \begin{cases} \sum_{p \in p(i)} \tilde{P}_p^{PEV} + P_i^o, & \text{if } i \in K \\ P_i^o, & \text{otherwise.} \end{cases} \tag{3.10}$$

where $p(i) \subset \mathcal{P}$ denote the set of PEV, which trip chains are captured by FCS at node i. $\tilde{P}_p^{PEV}$ equals P_p^{PEV} when the PEV is charging at the studied time instance, and equals 0 otherwise.

The total real and reactive power losses measured at transformer m, P_m^{loss} and Q_m^{loss} are function of nodal voltages. The voltage magnitude at node j is estimated as

$$\begin{aligned} V_j^2 =& V_i^2 - 2(z_{i,j}^r P_i^A + z_{i,j}^i Q_i^o) \\ &+[(z_{i,j}^r)^2 + (z_{i,j}^i)^2]\frac{(P_i^A)^2 + (Q_i^o)^2}{V_i^2}, \quad \forall e_{i,j} \in \mathcal{E}_{\mathcal{P}} \end{aligned} \tag{3.11}$$

where $z_{i,j}^r$ and $z_{i,j}^i$ are the resistance and reactance of the branch $e_{i,j}$.

The FCS planning is constrained by the total number of FCS, N_{FCS},

$$\sum_{k \in K} x_k = N_{FCS} \tag{3.12}$$

The FCS location is further subject to the reliability requirements of the distribution system. First, voltage magnitude must be within a predefined range as

$$\underline{V_i} \leq V_i \leq \overline{V_i}, \ \forall i \in \mathcal{V}_{\mathcal{P}} \tag{3.13}$$

where the upper and lower bound of voltages, $\underline{V_i}$ and $\overline{V_i}$, are determined according to the ANSI standards [116]. Secondly, the power flow must be within the lines' power delivery capacity, written as

$$-\overline{P}_{i,j} \geq P_{i,j} \leq \overline{P}_{i,j}, \tag{3.14}$$

where power flow $P_{i,j}$ on branch $e_{i,j} \in \mathcal{E}_P$ can be calculated with (3.8) and (3.10) using KCL.

3.3 Solving the Proposed Model

The planning problem in (3.1) - (3.14) is a generalization of Knapsack Problem (KP) [117]. KP and its variants, *i.e.,* combinatorial problems are NP-hard [118]. The consideration of power grid cost and reliability requirements further complicated the

Algorithm 1 CE Optimization Algorithm

Parameters:
$|K|$: cardinality of set K; M: number of sample solutions in each iteration; γ: rarity parameter.

1: Initialize $\mathbf{v} \in \mathbb{R}_{[0,1]}^{|K|}$.
2: **while** $\mathbf{v}$ is non-degenerate (*i.e.,* $\exists\ v_k \in (0,1)$) **do**
3: Sample M solution vectors $\mathbf{X}_1, \ldots, \mathbf{X}_M$ based on the PMF $\mathbf{f}$ and the $\hat{\mathbf{v}}$.
4: Evaluate $S(\mathbf{X}_i)$ for $i = 1, \ldots, M$
5: Select all the vectors $\mathbf{X}_i^*$ that satisfy $\mathbf{I}\{S(\mathbf{X}_i) \leq \gamma\}$
6: $\mathbf{v} \leftarrow$ the mean of $\mathbf{X}_i^*$
7: **end while**
8: **end**

problem by adding nonlinear terms in the objective function, *i.e.,* TCO^T, TCO^V, as well as nonlinear constraints (3.13) - (3.14). In this section, we propose a graph-based Cross-Entropy (CE) method to solve the formulated problem.

3.3.1 Principle of the Cross-Entropy (CE) Method

CE method was first proposed in [119]. It unifies many existing population-based optimization heuristics and is easy to implement for a diverse range of problems, such as mixed-integer nonlinear programming, optimal policy search, clustering, etc. The basic idea behind the CE method is that locating an optimal solution within the search space is a rare event. Hence, by gradually steering the sampling distribution of the search, we can make the rare event more likely to occur [120]. For this purpose, CE is used as a measure of closeness between two sampling distributions.

The proposed algorithm is summarized in Algorithm 1. Suppose the search space is the set of candidate FCS locations K (viz. (3.2)) and its cardinality is $|K|$. We vectorize the decision variables $x_k,\ k \in K$ in (3.1) as $\mathbf{x} \in \{0,1\}^{|K|}$. Hence, the

deterministic problem (3.1) - (3.14) can be casted into the probabilistic space by randomizing its solution vector $\mathbf{x}$. In the rest of the paper, $\mathbf{X}$ stands for the random vector of $\mathbf{x}$, while X_k stands for the k-th element of $\mathbf{X}$, that is, the random variable of x_k. The algorithm carries out an adaptive importance sampling process iteratively, and each iteration has two steps [121].

In the first step, we sample M vectors, $\{\mathbf{X}_1, \mathbf{X}_2, \ldots, \mathbf{X}_M\}$, in the solution space under a family of Probability Mass Functions (PMF), $\mathbf{f} : \mathbb{R}^{M\times|K|} \rightarrow \mathbb{R}^{M}_{[0,1]}$. Since $\mathbf{X}$ is a binary vector, a simple choice for the PMF could be the multivariate Bernoulli distribution. Equation (3.15) gives the k-th PMF in the t-th iteration

$$f_k^{(t)} = v_k^{(t)} X_k^{(t)} + (1 - v_k^{(t)})(1 - X_k^{(t)}) \tag{3.15}$$

where $v_k^{(t)} \in \mathbb{R}_{[0,1]}$ is the Bernoulli parameter. The vector of v_k is denoted as $\mathbf{v} \in \mathbb{R}^{|K|}_{[0,1]}$.

In the second step, we update the parameter vector $\mathbf{v}^{(t)}$ of the PMF $\mathbf{f}^{(t)}$ based on the performance of the sampled solutions in the t-th iteration, $\mathbf{X}_i^{(t)}$. The updating rule for the k-th parameter can be written as

$$v_{t+1,k} = \frac{\sum_{i=1}^{M}(\mathbf{I}\{S(\mathbf{X}_i^{(t)}) \leq \gamma\} \cdot \mathbf{X}_{i,k}^{(t)})}{\sum_{i=1}^{M} \mathbf{I}\{S(\mathbf{X}_i^{(t)}) \leq \gamma\}}, \quad k = 1, \ldots, |K| \tag{3.16}$$

where $\mathbf{X}_{i,k} \in \{0, 1\}$ is the k-th element of the $\mathbf{X}_i$. $\mathbf{I}\{\cdot\}$ is an indicator function, which equals 1 when the condition in the bracket holds, and equals 0 otherwise. $S(\mathbf{X}_i)$ represents the objective function (3.1) evaluated at the sampled solution $\mathbf{X}_i$. γ is a predetermined parameter. The solution vectors that satisfy $S(\mathbf{X}_i) \leq \gamma$ are referred to as *elite samples* and are denoted as $\mathbf{X}_i^*$. It can be easily seen that (3.16) updates the k-th Bernoulli parameter with the mean of the elite samples' k-th elements.

Finally, $X_i^{(t)}$ is an optimal solution, if $\mathbf{v}^{(t)}$ becomes a binary vector. This is because based on (3.15) and (3.16), once $v_k^{(t)}$ becomes 0 or 1, it will remain that value in the future iterations.

Remark 2. To avoid the guided search getting trapped in local minimum , the smooth updating technique may be used so that $\hat{\mathbf{v}}^{(t+1)} = \alpha \mathbf{v}^{(t+1)} + (1-\alpha)\mathbf{v}^{(t)}$, where $\alpha \in [0, 1]$ is the smoothing parameter.

3.3.2 A Parallel Implementation

For large-scale complex networks, high dimension nonlinear constraints result in a high dimension search space and likely prohibitive computational burden. Grounded in the graph computing platform elaborated in Section 3.2.4, we propose a paralleled implementation based on the MapReduce mechanism [122]. It allow for leveraging the available computing resources such as high-performance servers or cloud computing to accelerate the computing process. Fig. 3.3 illustrates the parallel implementation of the proposed algorithm.

MapReduce uses a split-apply-combine strategy for assigning the work to different computing threads to achieve parallelism. In each iteration, five phrases, "input", "splitting/mapping", "apply", "reducing", and "final result" are created. The "input" phase generates samples, $\mathbf{X}_i, i = 1, \cdots, M$ according to the probability distribution $\mathbf{f}$ and $\mathbf{v}$. Then each sample, $\mathbf{X}_i$, is mapped with one computing node handled by a worker in the computing resource partition process. The calculation in each computing node can be paralleled through the hierarchical group synchronization mechanism in bulk synchronous parallel (BSP) [123]. The performance function value, $S(\mathbf{X}_i)$, of each sample is obtained at the local computing node in the "apply" phase. In the

"reducing" phase, the elite samples, $\mathbf{X_i^*}$, are generated based on the rarity parameter, γ. In the "final result" phase, the probability vector, $\mathbf{v}$, is updated and the algorithm is ready for next iteration. In general, a sufficiently large sample size and problem cardinality is the premise to achieve a reasonable speedup factor [124].

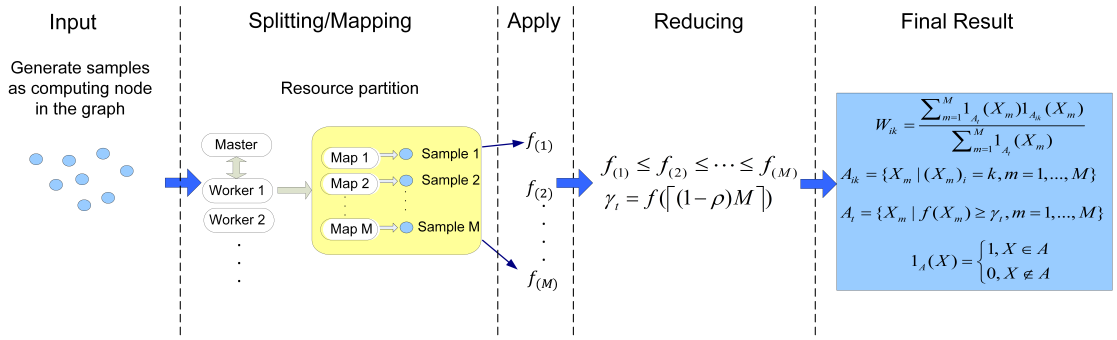

Figure 3.3: Framework of Paralleled CE Method based on MapReduce Mechanism

3.4 Case Study

3.4.1 Simulation Setup

The integrated location planning model with paralleled CE solving algorithm is tested on a synthetic network, *i.e.,* 25-node transportation network coupled with IEEE 123-node distribution test feeder, both of which are commonly analyzed in corresponding research communities [109, 125]. All transportation nodes are geographically mapped to IEEE 123-node system, *i.e.,* $\mathcal{V}_\mathcal{T} \subset \mathcal{V}_\mathcal{P}$. The detailed mapping relationship is shown in Table 3.1. It is also assumed that every node in $\mathcal{V}_\mathcal{T}$ is a candidate location of FCS, which brings the planning problem cardinality to $n = |\mathcal{X}| = 25$.

Table 3.1: Mapping Relationship of Coupled Networks

Transportation Node ID	01 02 03 04 05 06 07 08
Distribution Node ID	30 26 24 48 47 51 46 42
Transportation Node ID	09 10 11 12 13 14 15 16
Distribution Node ID	22 19 65 108 62 09 104 98
Transportation Node ID	17 18 19 20 21 22 23 24 25
Distribution Node ID	67 61 57 54 13 01 06 17 86

The topology of the transportation network alone and the power-transportation coupled network are shown in Fig. 3.4a and Fig. 3.4b, respectively. The number on each road segment represents the normalized distance between two adjacent nodes. We assume that the per-unit distance in Fig. 3.4a is 10 miles, *e.g.,* the distance of segment (1,2) is 4 units, which corresponds to 40 miles. Fig. 3.4a also illustrates three PEV trip chains in the transportation network obtained by the shortest distance algorithm, highlighted by red, green, and yellow. The respective O-D pairs are (1,16), (8,18), and (15,24).

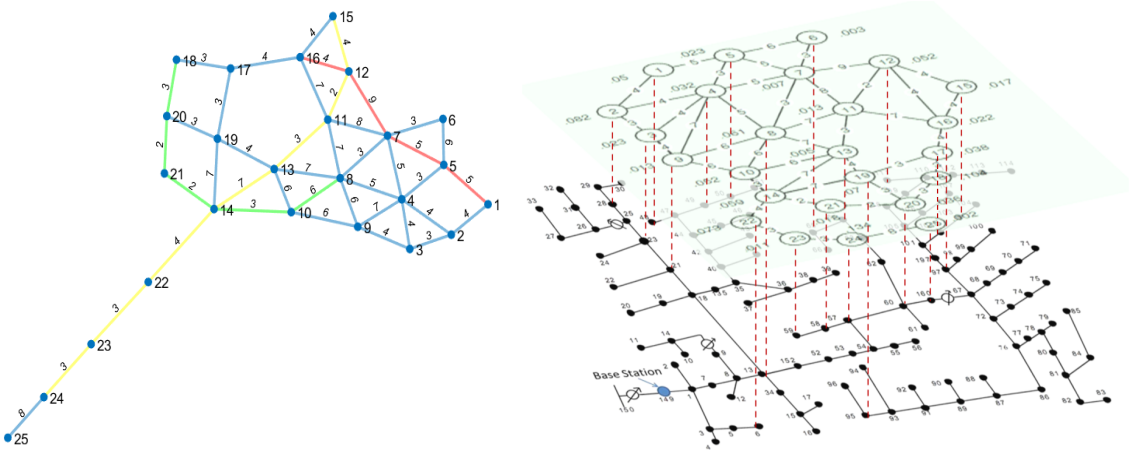

(a) Illustration of Shortest Distance Trip Chain for 3 PEVs

(b) Illustration of Power-Transportation Coupled Network

Figure 3.4: Synthetic Test Network

As a predictive planning guideline, this case study investigates 2 scenarios of total PEV amounts in the system, *i.e.,* 500 and 1000 PEV fleets. The scenario setting of PEV amounts falls in the reasonable median of the load capacity in the 123-node feeder while taking into account the proactive PEV penetration trend. Each individual PEV has a pre-determined random departure time and O-D pair, as well as a trip chain q generated by the shortest distance algorithm, all of which serve as the input of FCM.

Table 3.2: Parameter Specification of Transportation Aspects

Parameter	**Value**
Number of PEV Fleets	500
	1000
Range R	200 mi
Battery Capacity C	50 kWh
MPG	4 mi/kWh
Charging Level P^{PEV}	120 kW
Avg. Speed	30 mph
Range Anxiety Threshold τ	40 %
c_1	\$ 115
c_2	\$ 7.5

The detailed parameter specification of the aforementioned transportation aspects is summarized in Table 3.2. Levelized daily capital cost coefficient c_1, which represents the hardware and installation cost of FCS, is estimated to be $c_1 = \$115$/day, where we assume there are 10 charge ports in every FCS [126]. The cost coefficient c_2, which represents the service revenue for captured charging at FCS, is selected by assuming every charging activity will recharge from range anxiety threshold ($\tau = 0.4$) to the full battery capacity, and the unit price for charging service is \$0.5/min according to an industry pilot project [127]. The specifications regarding power supply aspects

and related TCO parameters in this case study are summarized in Table 3.3. A detailed distribution feeder dataset can be referred to [125]. The case studies are implemented on a server with the graph-computing platform, TigerGraph v2.3. The testing environment is summarized in Table 3.4.

Table 3.3: Power Grid Specifications and TCO Parameters

Parameter	**Value**
Transformer Rating (s_R) [MVA]	5
Permitted Voltage Range ($[\underline{V_i}, \overline{V_i}]$) [p.u.]	[0.95, 1.05]
Transformer Core Loss (CL) [kW]	13.2
Transformer Load Loss (LL) [kW]	53
Levelized Yearly Demand Cost (DC) [$/kW-yr]	120
Responsibility Factor (RF)	0.81
Energy Cost (EC) [$/kWh]	0.05
Dynamic Load Factor Constant (γ)	0.2
Interest Rate (i) [%]	5
Transformer Capital Cost (C_o^T) [$]	70,000
VR Capital Cost (C_o^V) [$]	4,500
Normal Transformer Lifetime [yr]	15.41
Empirical Maximum Number of VR Operations	200,000

Table 3.4: Testing Environment of Graph Platform

Hardware Environment	
CPU	4 sockets × 16 cores × 2 threads @2.50 GHz
Memory	64 GB
Software Environment	
Operating System	Linux CentOS 6.8
Graph Platform	TigerGraph v2.3

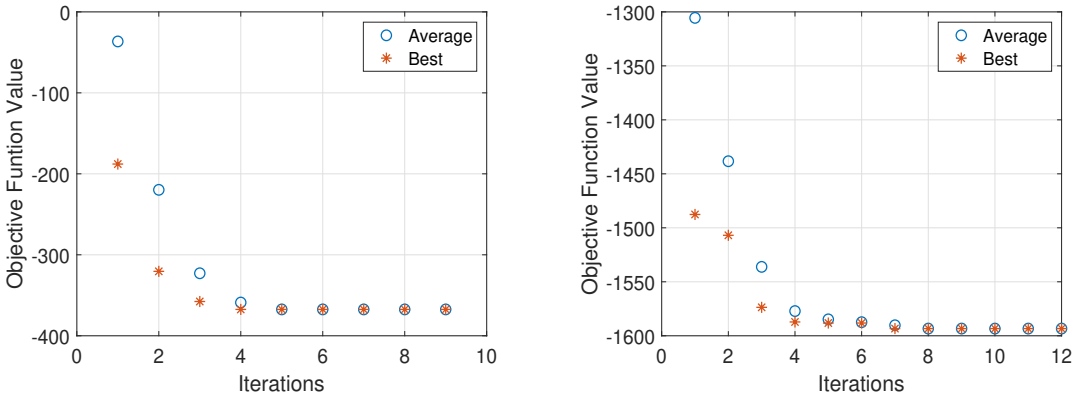

(a) 500 PEVs Case (b) 1000 PEVs Case

Figure 3.5: Convergence of Objective Function Value

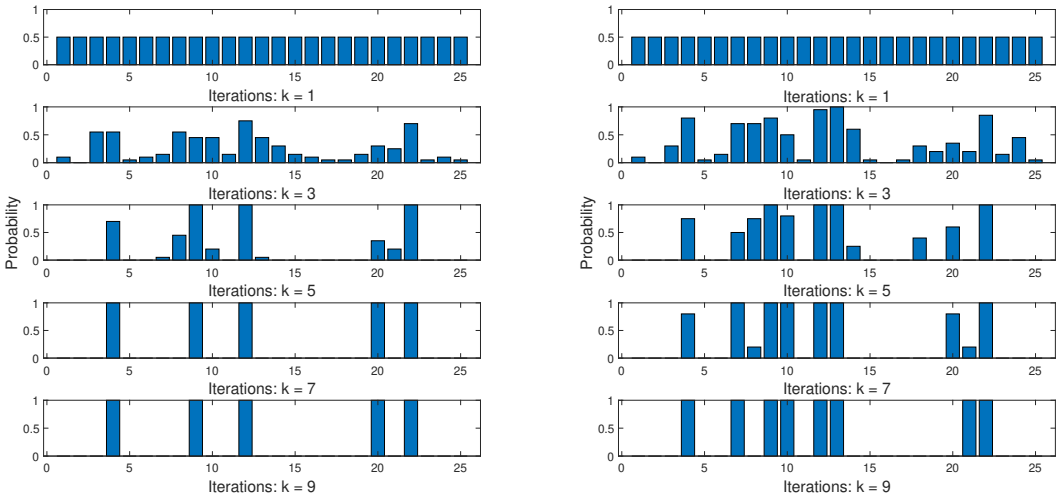

(a) 500 PEVs Case (b) 1000 PEVs Case

Figure 3.6: Evolution of Decision Variable Vector

3.4.2 Location Planning Results

The performance function $S(\mathbf{X})$ in CE algorithm is equivalent to the objective function of the planning model in (3.1). Hence, the convergence of $S(\mathbf{X})$ indicates the minimization of objectives simultaneously. The distribution system operating constraints in (3.13) - (3.14) are enforced by adding penalty terms with a sufficiently large coefficient c_p in the objective function. Without loss of generality, the resource capacity N_{FCS} constraint in (3.12) is not considered in this particular case study, as it's up to the practitioner to decide the amount of available resources.

The FCS location planning results are presented in Fig. 3.5 and Fig. 3.6. As observed in Fig. 3.5a and Fig. 3.5b, the total cost, *i.e.,* objective function value, converges in less than 15 CE iterations. The "Average" is the mean value of 1000 samples of objective function value, and "Best" is the smallest value among 1000 samples of objective function value. Furthermore, Fig. 3.6a and Fig. 3.6b shows the evolution of decision variable vector $\hat{\mathbf{v}}_t$, which converges to a binary vector that corresponds to the optimal solution. The CE stopping criteria is that the maximum difference among any components in decision variable vector $\hat{\mathbf{v}}_t$ between iterations are less than $\varepsilon = 0.001$. Therefore, the optimal locations to place FCS for 500 PEVs and 1000 PEVs are $X = \{4, 9, 12, 20, 22\}$ and $X = \{4, 8, 9, 10, 12, 13, 14, 23\}$, respectively.

It can be observed that the transportation aspects outweigh the power supply aspects with the selection of cost coefficients in this particular case study. In other words, the profits from capturing more charging actions overcome the negative impacts on the capital and long-term cost of grid assets. The planning model tends to add more capital investment, *i.e.,* build more FCS, when the number of PEV fleets

increased. Depending on case-by-case engineering practice, regions, demographic discrepancy, etc., multiple cost coefficient combinations can be applied to the proposed planning model. To incorporate a diverse range of cost items or structures, we can easily modify the objective function (3.1) without fundamentally changing the solving mechanism and raising the computational burden.

3.4.3 Effect of Grid Operating Constraints on Solution

The constraints in (3.13) - (3.14) set the distribution system operating bounds that ensure the grid reliability and grid assets' viability. This section compares the optimal solution performance before and after adding these operating constraints. Fig. 3.7 shows the substation transformer's daily loading at the optimal solution condition. It can be observed that the transformer rating, *i.e.,* 5 MVA, effectively bounds the total load profile at the substation, which mitigates the negative charging impact on the transformer and subsequent TCO, as the asset degradation is sensitive to overloading frequency. Furthermore, the optimal solution changes after adding the constraints, as shown in the summary Table 3.5. The hard power flow constraints have confined the incentive to build more FCS for more captured demand at the expense of grid asset depreciation. For example, the daily TCO^T is reduced by $\sim 50\%$ (\$ 7.018 $\rightarrow$ \$ 3.677) after enforcing the operating constraint.

Fig. 3.8 presents the voltage profile at an end node (node 48, Phase A) of the test feeder at the optimal solution condition. As opposed to the transformer flow limit, the voltage constraints do not saliently affect the solution nor the overall cost in this case. This is because, under 500 or 1000 PEV fleets, all nodes' voltage profiles are staying within the acceptable range $[0.95, 1.05]$ due to multiple VR's regulation, and thus no

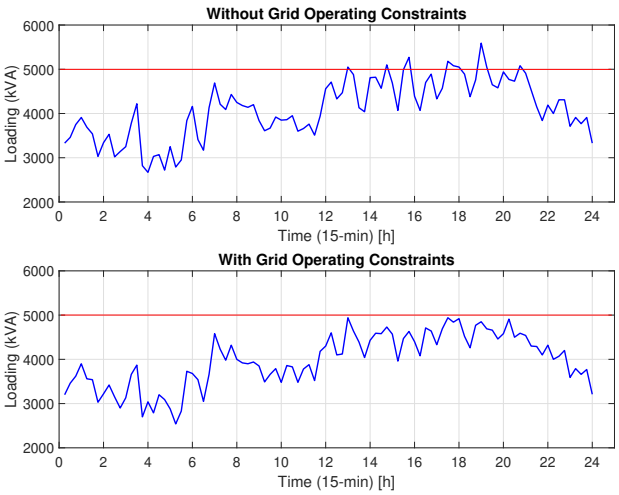

Figure 3.7: Substation Transformer Loading at Optimal Solution

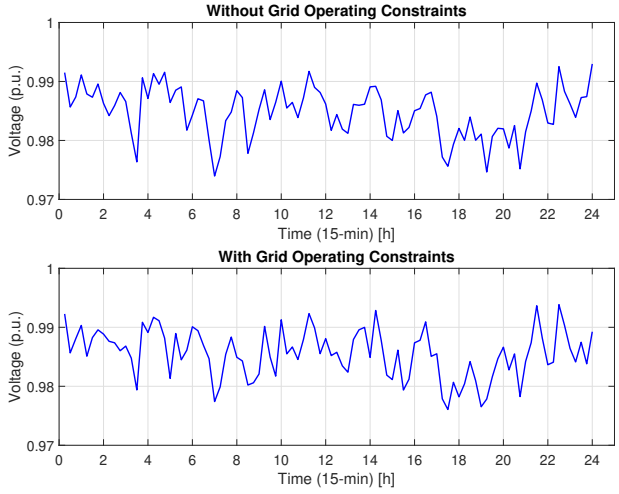

Figure 3.8: End Node Voltage Profile at Optimal Solution

violation of voltage bound occurs in any sample. With more PEV integrated into the system, it is more likely to observe the noticeable smoothing effect of voltage bounds. Nevertheless, even if the over-planning strategy in the distribution system might

Table 3.5: Comparison of Planning Results

Result at Optimal Solution	**Without Operating Constr.**	**With Operating Constr.**
Planned Sites	{4,6,8,9,10, 12,13,14,18,22}	{4,8,9,10, 12,13,14,23}
TCO^T	$ 7.018	$ 3.677
Maximum Loading	5594.43 kVA	4942.81 kVA
Daily VR Operations	346	364
Captured PEV Volume	556	502

conceal the internal complexity of problem structure, the fidelity of the proposed method in the power aspect is demonstrated at various PEV penetration scenarios.

3.4.4 Discussion on Computational Efficiency

When the search space of the planning problem becomes more complex, as in the real-world coupled network with thousands of electric and transportation nodes, the computing time required increases accordingly, as does the need for parallel implementation. The total run time of the planning model is shown in Fig. 3.9 to demonstrate the parallel computing capability under the proposed graph-based scheme. With the increasing number of computing threads, the average computing time of the entire solving process reduces. As future work, it would be promising to implement the proposed planning model and solving platform on the real-world, large-scale system, as shown in Fig. 3.10.

3.4.5 Discussion on Solution Quality

Table 3.6 summarizes the parameters of CE optimization algorithm used in this particular case study. Under this set of parameter, the convergence of objective function value and the evolution of decision variable vector (viz. Fig. 3.5 and Fig. 3.6)

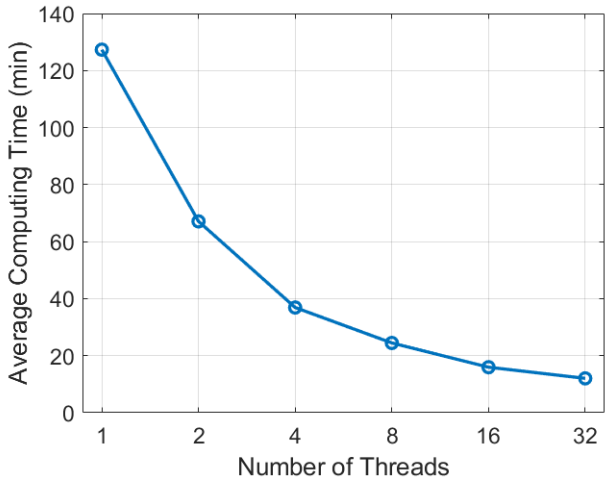

Figure 3.9: Graph Parallel Computing Performance

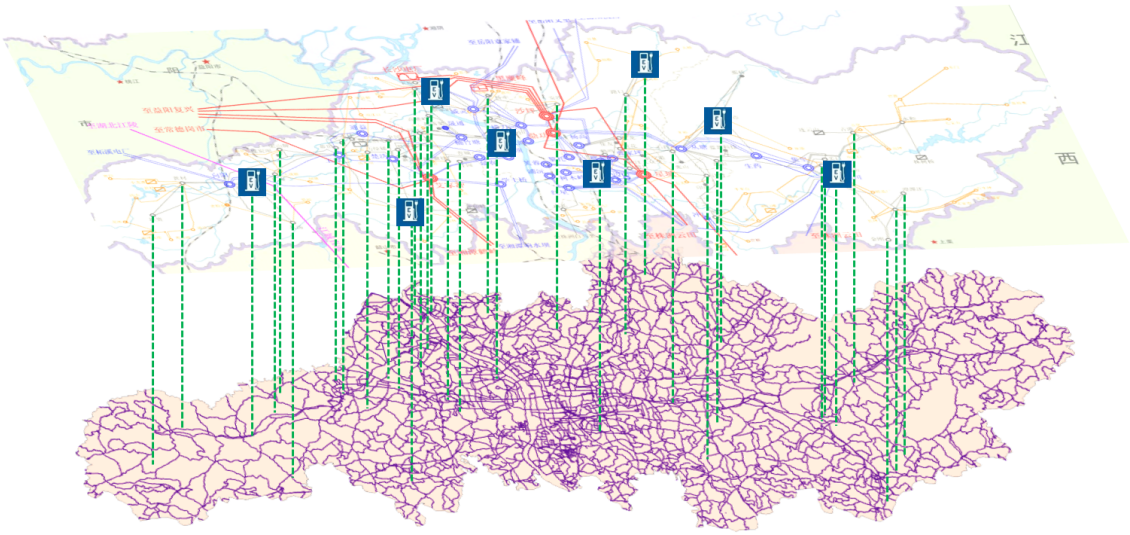

Figure 3.10: Large-scale, Real-World Power-Transportation Coupled Network

show a good alignment and decisive guideline to the solving process. Note that it generally takes a fine tuning of these parameters in order to reach a desirable trade-off between solution quality and computational efficiency. For example, when the

problem cardinality, *i.e.,* $|K|$, increases as in large-scale, real-world case, the number of CE samples M needs to be raised accordingly. Further, the rarity parameter γ needs to be tuned to achieve an empirically desirable "effective" elite sample amounts.

Table 3.6: Parameters of CE Optimization Algorithm

Parameter	**Value**
Problem Cardinality $\|K\|$	25
Number of Samples M	1000
Rarity Parameter γ	2%
Smoothing Parameter α	0.7
Stopping Criteria Threshold ε	0.001

3.5 Summary

With the development of charging technologies, the auto industry has envisioned the ability to recharge PEVs at speeds comparable to the traditional gas refueling. This chapter proposed a graph-computing based integrated location planning model for PEV fast charging stations (FCS). The proposed model considers the requirements for FCS in both aspects of power supply and transportation, thus guaranteeing reliable power grid operation as well as economic planning decisions. The proposed formulation contains integer decision variables and nonlinear terms in objective functions as well as constraints. To ensure fast convergence of the solution, we further propose a graph-based cross-entropy (CE) optimization algorithm, which enhances computational efficiency with graph parallel computing technique. The proposed model and algorithm are validated on a synthetic power and transportation coupled network. This work is the initial effort to address the interdisciplinary FCS planning problem.

Chapter 4: Transmission Level PEV Charging Impact

4.1 Motivation and Related Works

This chapter starts to investigate PEV's charging impact on the power transmission system. Under the ambition of boosting the charging speeds that are comparable to traditional gas refuelling, Ultra-Fast Charging Station (UFCS) has been conceptualized and piloted into the charging infrastructure development [128,129]. At present, there is no standardised power rating or terminal configuration to define UFCS due to the lack of wide-spread implementation, as shown in Table 1.2. A working definition is that the charging level of UFCS can reach up to 500 $kW \sim 1\ MW$, per vehicle per charge, and connected to three-phase DC power.

Under this context, individual UFCS brings total station power draw to 2∼6 MW (estimated parking 4∼12 vehicles), which is comparable to industrial loads [130]. To support and accommodate such a high power draw, UFCS's connection point to the power grid has been considered at the transmission/sub-transmission level instead of the medium/low voltage distribution network [131]. Similar to certain industrial loads, UFCS serve as a primary customer with direct power supply from transmission system. Besides conceptual proposals and a few pilot projects detailed in Chapter 3, Section 3.1, the feasibility, topology, and business model of UFCS have yet to be

thoroughly studied. At the transmission level, literature has assessed UFCS and aggregate of lower level PEV charging in their participation in electricity markets [39–41], frequency regulation [42, 43], congestion management [44, 45], coordination with renewable energy resources [46], and transmission expansion planning [48], etc.

However, the fast growth of PEV and UFCS could exert more disruptive impact on the power grid, including cascading failure. Cascading failure is one of the most catastrophic phenomena that can occur in power transmission systems. The 2003 North American cascading failure left an estimated 50 million people without power in 9 states for more than 4 days, resulting in an estimated total financial loss of 10 billion U.S. dollars [132]. Due to its significance, cascading failure analysis is conducted by utilities and Regional Transmission Operators (RTO) during the transmission planning stage. However, such long-term forecasts often have to accommodate uncertainties through over-planning, which considers the worst case of the maximum coincidental load, leading to high cost or even reliability issues.[4]

On the other hand, to prevent the system from catastrophic failures, RTOs and some utilities conduct routine cascading studies in day-ahead outage scheduling, allowing them taking timely actions to assure system reliability. Such cascading studies are deterministic and use DC power flow approximations to accelerate the convergence, which could lead to incorrect decisions that impact end users. Given the highly stochastic nature of PEV charging, incorporating detailed loading models in AC power flow analysis is highly desirable to achieve accurate results. However, this would require an extensive computation time. While a few research have been devoted

[4]For example, the increased line capacitance will lead to over-voltage during the off-peak hours. This phenomenon has been observed in states of high PEV penetration, such as California.

to cascading failure analysis, they cannot address both of the above problems simultaneously. For example, [133] and [134] present analytic models for cascading failure analysis based on the theory of self-organized criticality. Those models describe load change with slow dynamics and describe grid topological change with fast dynamics. Therefore, they are not suitable for capturing frequent load changes induced by PEV charging. [135] proposes a GPU-based LU-factorization solver which allows for fast analysis of massive power flows. However, the solver is grounded in DC power flow and cannot guarantee the same accuracy as AC power flow. [136] developed an interaction graph to predict cascading outages based on historical grid response. While using AC power flow, this method requires long runtime and can only be implemented offline.

To address the above problems, in this chapter we propose a methodology based on graph-computing techniques to investigate the cascading failures induced by large-scale PEV integration aggregated at UFCS level. In particular, the contributions of this work are threefold:

(i) Proposed a graph modeling method for PEV-integrated transmission system. The representation of the grid topology allows for a) fast model establishment with a faithful presentation of PEV charging patterns at multiple UFCS; and b) efficient implementation of AC power flow.

(ii) Developed an online method for stochastic cascading outage analysis, wherein spatial and temporal stochasticity of the PEV charging behavior are embedded under the umbrella of Monte-Carlo Simulation (MCS).

(iii) Grounded in the above results, developed a graph-computing based cascading failure evolution (G-CFE) analysis, which encompasses line-tripping, island-detection, and generation/load re-dispatch in a closed loop.

The Node-based Parallel Computing (NPC), HierArchical Parallel Computing (HAPC), and Breadth-first Search (BFS) based graph traversal have been applied to improve computational efficiency. The proposed G-CFE analysis will enable RTOs and utilities to conduct accurate cascading studies in transmission systems which are highly penetrated with PEV and take timely actions to assure grid operation reliability.

The proposed G-CFE analysis is not limited to analyze systems of uncertainties induced by PEV charging, and can be applied to analyze the system with other uncertainties, such as intermittent renewable outputs and base load spikes. The later uncertainties, nevertheless, generally present less discreteness than PEV charging and is acceptable to be modeled in aggregates. Therefore, we do not explicitly discuss the performance of the proposed method regarding those uncertainties. In addition, this work assumes that the power grid operates in the steady-state. Finally, the "transmission system" and "power grid" are used interchangeably throughout this chapter.

4.2 PEV-integrated Power Grid Graph Modeling

4.2.1 Graph based Stochastic PEV Integration

As illustrated in Chapter 3, Section 3.2.4, graph is a data structure based on graph database (GDB), which is suitable for modeling pairwise relationship between objects in a network. In this chapter, a graph-based grid model has been adopted as

the natural representation of power transmission system, as denoted by an undirected graph $\mathcal{G} = (\mathcal{V}^{bus}, \mathcal{E}^{line})$, where $\mathcal{V}^{bus}$ is the vertex class of electric buses, and $\mathcal{E}^{line} \subseteq \mathcal{V}^{bus} \times \mathcal{V}^{bus}$ is the edge class of transmission lines. The bus and line related information are stored as "attributes" of vertices and edges in the power grid graph model.

Grounded in the graph-based power grid modeling, the PEV's charging is modeled as a relationship between PEV objects and electric bus objects. This relationship is implemented as the "PEV-TO-GRID" edge class $\mathcal{E}^{PEV-G}$ connecting "PEV" vertex class $\mathcal{V}^{PEV}$ and $\mathcal{V}^{bus}$, as seen in the left-hand side of Fig. 4.1. Hence, the full graph of a power grid with PEVs is $\mathcal{G} = (\mathcal{V}^{bus}, \mathcal{V}^{PEV}, \mathcal{E}^{line}, \mathcal{E}^{PEV-G})$. For the vertex class $\mathcal{V}^{bus}$, all one-hop neighbors of a node are said to be in the first *level* corresponding to that node, and two-hop neighbors are in the second *level*, and so forth.

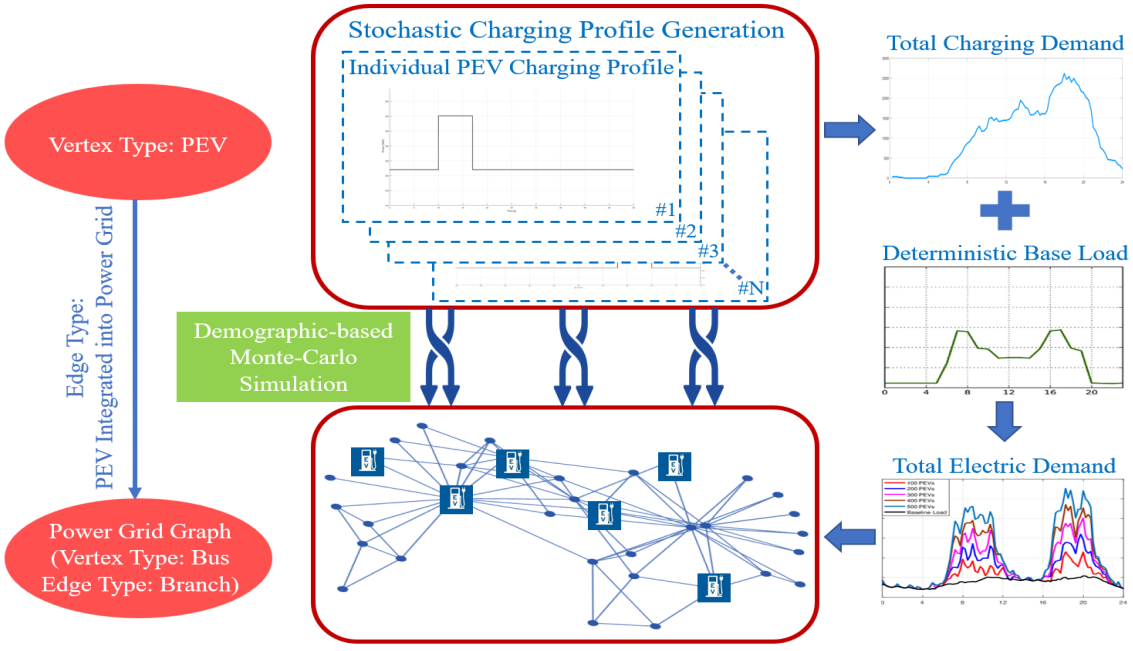

Figure 4.1: Workflow of Graph based Stochastic PEV Integration

To consider stochastic charging patterns and locations of PEVs, Monte-Carlo Simulation (MCS) of power flows is implemented in the time-series (TS) analysis, which records the power grid response by running power flow over consecutive time instants. The working principle is shown on the right-hand side of Fig. 4.1. The PEV's charging locations are selected based on multiple factors, *e.g.,* demographics, regulatory conditions, societal considerations, etc., which are elaborated in Section 4.4. In each iteration of MCS, the total demand is re-established as the sum of a new set of stochastic PEV loads and the deterministic base load. The law of large numbers indicates that as the sample size gets large enough, the expected value of the model outputs can be approximated by the sample mean of the MCS results.

4.2.2 PEV Charging Profile Modeling

A stochastic method is developed to determine individual PEV's daily charging profile. To simplify the generation process, we assume that all PEVs utilize the lithium-ion battery, and thus the real power demanded by a PEV remains constant during its charging duration [137]. Based on PEV specs on the market [138], we characterize a PEV load as below:

The State of Charge (SOC) when individual trip starts is

$$SOC = 1 - \frac{D_t}{R}, \tag{4.1}$$

where D_t (mile) is the mileage traveled since the last charge, R (mile) is the PEV's driving range. The corresponding charging duration t_r (h) is

$$t_r = \frac{C \cdot (1 - SOC)}{c}, \tag{4.2}$$

where C (kWh) is the battery capacity, c (kW) is either the residential charging level, c_r, or the public charging level, c_p, depending on its charging location. Based on PEV driving surveys, we adjust the parameter D_t to follow Gaussian distributions [139].

The PEV users' charging intention is mainly characterized by a range anxiety threshold SOC_{TH}, below which the driver will look for UFCS. The SOC_{TH} is defined as a Normal distributed random variable according to a driver survey [140].

$$SOC_{TH} \sim \mathcal{N}(\mu_{TH}, \sigma_{TH}^2), \tag{4.3}$$

where μ_{TH} and σ_{TH}^2 are mean and variance of SOC_{TH}. Furthermore, the use type of vehicle is categorized as the following two groups.

Commuting Vehicles: Private commuters are the most common usage of vehicle, which departure in the morning for work and return home in the evening. The daily commuting time T_c (h) and one-way distance D_c (mile) follow a Normal distribution

$$T_c \sim \mathcal{N}(\mu_{tc}, \sigma_{tc}^2); \qquad D_c \sim \mathcal{N}(\mu_{dc}, \sigma_{dc}^2). \tag{4.4}$$

Based on the common office hour from 9 am to 5 pm, the vehicle is *en route* from $(9 - T_c)$ am until $(17 + T_c)$ pm. Hence, the SOC in (4.1) for commuting PEVs is

$$SOC = 1 - \frac{2D_c}{R}. \tag{4.5}$$

Ride Service Vehicles: Ride service vehicle becomes an increasingly important component of the transportation system, especially in the densely populated metropolitan area. PEVs have entered this market, *e.g.,* London and Montreal have both introduced PEV cabs [141,142]. Moreover, many PEV owners have turned their vehicles into app-based ride service vehicles. As compared to commuting vehicles

which have a relatively regular driving pattern, ride service vehicle has more flexibility, *i.e.,* the *en route* duration, speed and charging anxiety are more divergent. Therefore, the driving pattern is additionally characterized by the average speed v_r (mph). A ride service vehicle starts daily trip at $t_{r,s}$ with the speed v_r. The mileage traveled before charging can then be written as

$$D_r = (1 - SOC_{TH}) \cdot R, \tag{4.6}$$

where the driver will only recharge at the public charging station with charging level c_p when $SOC < SOC_{TH}$.

4.3 Graph-computing based Cascading Failure Evolution

4.3.1 Graph based Power Flow Analysis

Power flow analysis is the precursory step of cascading outage analysis. We adopted the graph-computing based fast decoupled power flow (FDPF) algorithm that has been proposed in the work [143]. The FDPF has the following iteration scheme

$$\Delta\mathbf{P}/\mathbf{V} = B'\Delta\boldsymbol{\theta} \tag{4.7}$$

$$\Delta\mathbf{Q}/\mathbf{V} = B''\Delta\mathbf{V}, \tag{4.8}$$

where $\mathbf{V}$, $\Delta\mathbf{P}$, and $\Delta\mathbf{Q}$ are vectors of bus voltage magnitude, real power injection increment, and reactive power injection increment, respectively. The real power injection $\mathbf{P}$ is the difference between total generation and total demand that consists of stochastic PEV loads and the deterministic base load. $\Delta\boldsymbol{\theta}$ and $\Delta\mathbf{V}$ are vectors of bus voltage phase angle and magnitude increment, respectively. B' and B'' are constant

Jacobian matrices deduced from Y_{bus} matrix. An illustration of Y_{bus} matrix formulation for a 10-bus system is shown in Fig. 4.2. The diagonal elements are stored as an attribute of $\mathcal{V}^{bus}$ and the off-diagonal elements are stored as an attribute of $\mathcal{E}^{line}$. Each row of Y_{bus} matrix corresponds to a node and is formed simultaneously since it only requires the information from its one-hop neighbors.

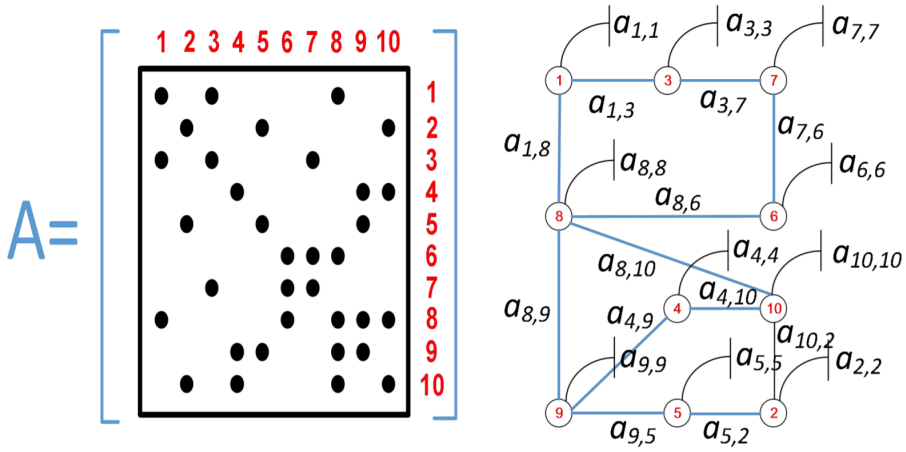

Figure 4.2: Y_{bus} Matrix Formulation for a 10-bus System

To accelerate the computation in FDPF, a graph-based parallel computing technique was developed based on the prior work [143, 144]. It mainly consists of two parts. First, the Node-based Parallel Computing (NPC) performs local computation at each node of $\mathcal{V}^{bus}$ and $\mathcal{V}^{PEV}$ by forming B' and B'' in (4.7) - (4.8), updating system states $\mathbf{V}$ and $\boldsymbol{\theta}$, and calculating branch flow. Second, the HierArchical Parallel Computing (HAPC) is used to formulate the elimination tree from the graph $\mathcal{G}$. The elimination tree is then layered from leaf nodes to the root node. The detailed formulation process is illustrated in a 10-node graph, as seen in Fig. 4.3 [145]. From bottom-up, HAPC performs the computation for nodes at the same layer in parallel,

and the layer next to it is performed after. With HAPC, the LU factorization of B', B'' matrices, which is the most time-consuming process in each power flow iteration, is performed efficiently. Besides the advantages of parallelism in problem formulation and solving process using graph-computing based FDPF, the entire power flow analysis is running in memory, thus saving heavy time cost induced by Input/Output operation between disk and memory. Therefore, with the graph-computing based FDPF, the computation process is highly in parallel, and the computation speed is significantly lifted. The detailed iterative workflow of the graph-computing based FDPF is shown in Fig. 4.4, where NPC and HAPC implementation are highlighted in blue and magenta, respectively. The total PEV charging demand (see Sec. 4.2), in combination with generation and base load profiles, is fed to the input of FDPF.

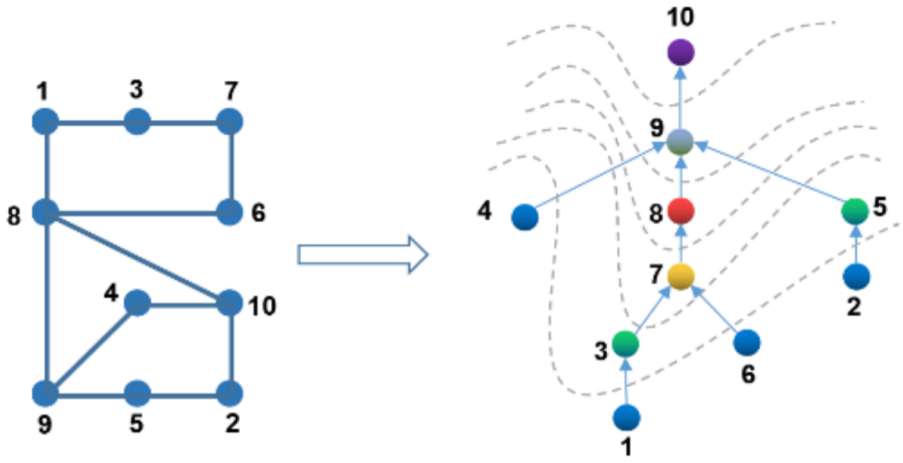

Figure 4.3: Forming Elimination Tree from the Graph

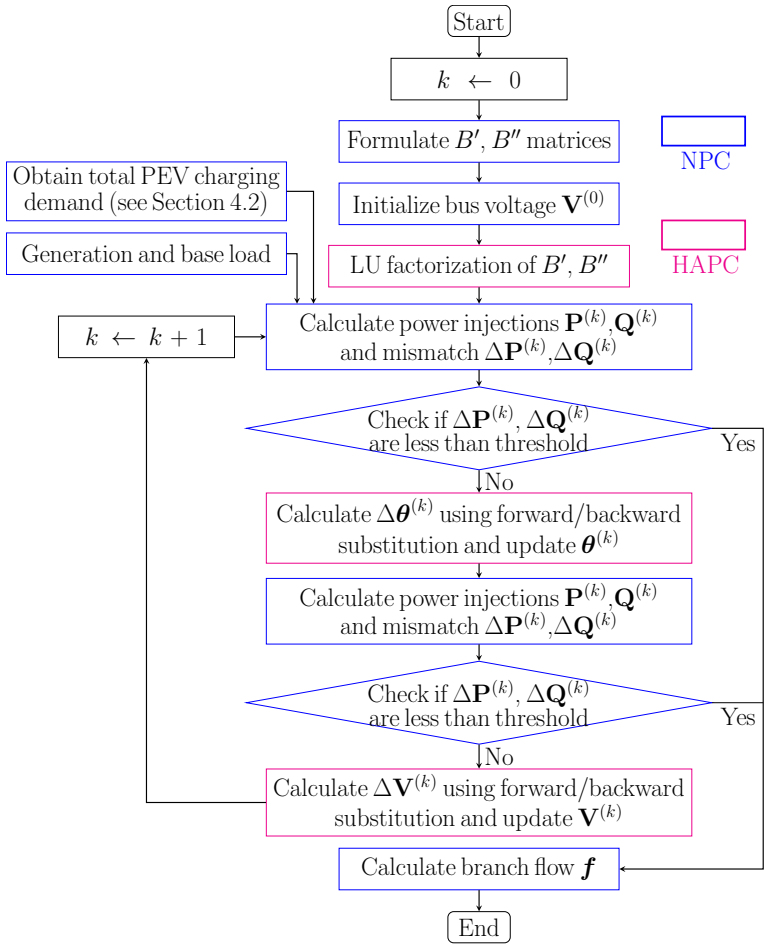

Figure 4.4: Graph-computing based FDPF

4.3.2 Graph-computing based Cascading Failure Evolution (G-CFE)

Cascading failure evolution is a mechanism in which the failure of grid components propagates to cause a large blackout of power transmission systems. As failures occur, the power system evolves successively weakened so that the chance of further failures is increased. In this work, we considered transmission lines tripped by overloading

relays.[5] Once the first outage alters the topology of the power grid, the power flow distribution is changed throughout the remaining system. The subsequent power flows could also exceed the relays' settings, which lead to more line outages. The process repeats until the system stabilizes, *i.e.,* no further overloading event occurs [146].

After the line tripping occurrence, island detection needs to be conducted, because the tripped line could likely be a bridge, also known as a cut-edge, which splits the system into islands, *i.e.,* the grid becomes a disconnected graph. In this study, the Breadth-First Search (BFS) based graph traversal is implemented within G-CFE model for island detection. The BFS starts at the root of the power grid graph $\mathcal{G}$ and visits all of its neighboring nodes at the present level in parallel before moving on to the nodes at the next level. The slack bus is selected as the root in the model for practical reasons. The nodes traversed in a searching path will be marked as *visited*. If the number of *visited* nodes through a complete searching path is less than the cardinality of the entire vertex set, then an islanding occurrence is detected.

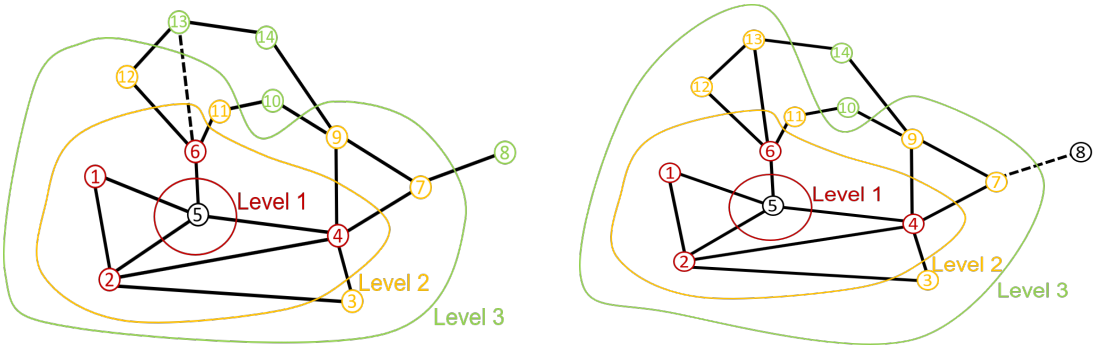

(a) No Islanding Detected (b) Islanding Detected

Figure 4.5: BFS based Graph Traversal for Island Detection

[5]In practice, System Integration Protection (SIP) may be armed under a cascading failure, which desensitize relays to prevent them from tripping. This mechanism is not included in this work to simplify the demonstration of the proposed analysis.

The illustration of such hierarchical parallel BFS traversal for island detection is shown in an exemplary network in Fig. 4.5. The tripped line$(6, 13)$ indicated by a dashed line in Fig. 4.5a is not a cut-edge, thus no islanding occurrence is detected. However, this tripping will cause the node 13 to be visited in color-coded Level 3 instead of Level 2 (*cf.* Fig. 4.5b), as the BFS traversal starts from the root node 5. On the other hand, the cut-edge line$(7, 8)$ in Fig. 4.5b is tripped, and thus one islanding occurrence is detected. Some generation (and/or load) may be lost upon an islanding occurrence. Hence, the demand-supply balance in the mainland is adjusted by decreasing the demand (supply) by the same factor at all demand (supply) nodes. This adjustment corresponds to the load shedding (generation curtailing) [146].

Fig. 4.6 shows the iterative workflow of the G-CFE model. Let $f_e, \forall e \in \mathcal{E}^{line}$ be the active power flow on each line and $\overline{f}_e$ be the corresponding capacity. Let $\mathcal{O}_k$ and $\mathcal{I}_k$ denote the set of line outages and set of islanding occurrence during the kth round of cascading failure, respectively. Let $\mathcal{O}^*$ and $\mathcal{I}^*$ denote the set of cumulative line outages and islanding occurrences until the current round. In this study, the set of initial outages $\mathcal{O}_0$ is determined by the overloaded line whose flow f_e exceeds the rating $\overline{f}_e$ due to the penetration of PEV. This process is repeated until completing the $m = 1, \ldots, M$ MCS runs for every time instant $t = 1, \ldots, T$.

In TS analysis, the G-CFE model is reset every time instant. The cascading outage that evolves in one time instant would not affect the starting status of the power grid in the subsequent instant. With the failure set $\mathcal{O}^*$ and $\mathcal{I}^*$ obtained, qualitative analysis can be conducted to conclude the relationship between base load and PEV charging demand, and how various factors, such as the power network topology, concentration

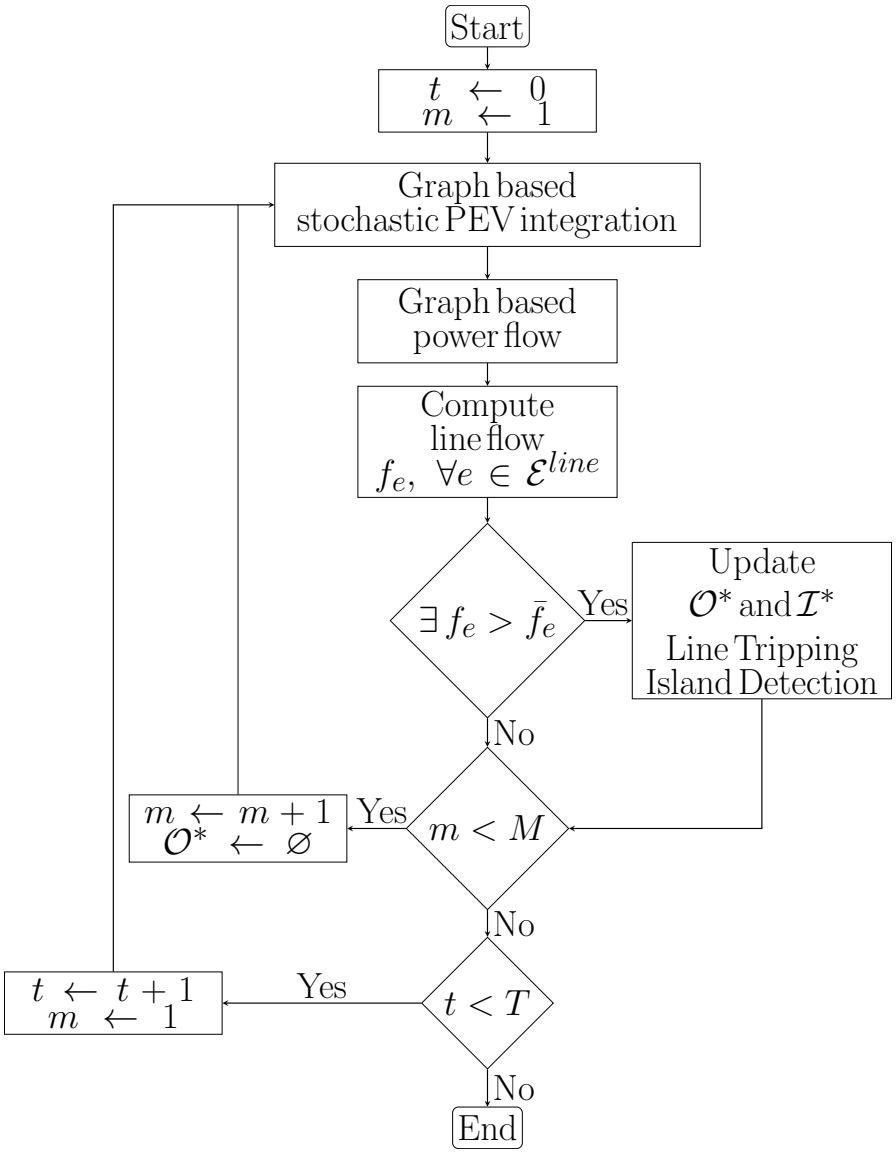

Figure 4.6: Workflow of G-CFE Model

of UFCS, and protection settings, lead to the cascading failures. Analysis can also be conducted to identify critical components that are prone to be affected.

4.4 Case Study

4.4.1 Simulation setup

The validity of the proposed method for UFCS impact assessment has been demonstrated on a large-scale provincial transmission system in Sichuan, China. The geographic area of Sichuan province, overlaid with the backbone transmission lines marked in blue, is shown in Fig. 4.7. This system has 2749 buses and 2917 transmission lines in total, with multiple voltage levels including 220 kV, 110 kV, 35 kV, 10 kV, etc. According to local utility practice, the transmission line is set to trip when the loading level reaches 125% of the line rating.

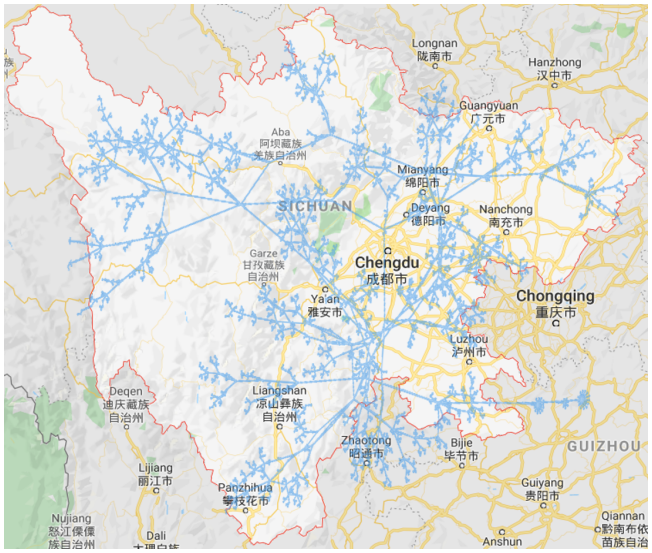

Figure 4.7: Provincial Transmission System in China

The base load at each bus h in the network P_h^b is formed with data from the SCADA's record on a typical summer day in the simulated system, with 15-min resolution. The normalized TS base load curve of one bus is shown in Fig. 4.8.

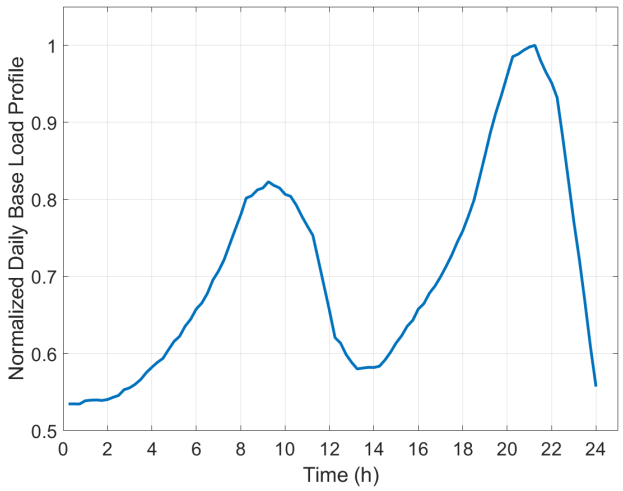

Figure 4.8: Normalized Time-series Base Load Curve

The total load profile at any location is the summation of P_h^b and the aggregated UFCS load P_h^{PEV}, which is generated by the model elaborated in Section 4.2.2. We assume a satisfactory PEV charging profile could be created using data from a segment of the PEV market rather than taking into account every PEV currently available to consumers. The PEV can utilize residential charging level $c_r = 19.2\ kW$ or public fast charging level $c_p = 120\ kW$. The battery capacity is assumed to be $C = 40\ kWh$ or $C = 60\ kWh$. Overall, there are three groups of PEV, a) commuting vehicle with c_r level and $C = 40$ kWh; b) commuting vehicle with c_p level and $C = 60$ kWh; and c) ride service vehicle with c_p level and $C = 60$ kWh, which formed a $1 : 2 : 2$ composition ratio of total PEV amounts in the study. Probabilistic parameters for generating individual PEV's charging profile have been detailed in [60] and thus omitted here.

Aiming at providing predictive planning guideline, this case study investigates four scenarios of PEV amounts ranging from 10,000 to 40,000 in the step of 10,000. The scenarios of PEV amounts are consistent with the penetration goal set by the provincial government. As of December 2017, there are around 23,000 PEVs in Sichuan, and the provincial government is targeting for 100,000 PEVs on the road by 2020. Hence, the particular cases of up to 40,000 PEVs fall in the reasonable median of the PEV density in the studied area. As for charging locations, 50 out of 2749 buses have been selected to be candidate locations of UFCS, based on demographic information that imitates the siting of the expressway service area. For example, currently there are 40 UFCS built along expressways which radiate from the capital city of Sichuan province. In 100 MCS runs, all PEV charging profiles will be randomly allocated to these 50 candidate locations during each iteration.

The case studies are implemented on a server with the graph-computing platform, TigerGraph v2.3. The testing environment is shown in Table 4.1.

Table 4.1: Testing Environment of Graph Platform

Hardware Environment	
CPU	2 CPUs × 6 cores @2.10 GHz
Memory	64 GB
Software Environment	
Operating System	Linux CentOS 6.8
Graph-computing Platform	TigerGraph v2.3

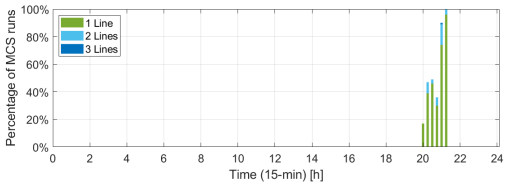

(a) Number of PEV: 10,000

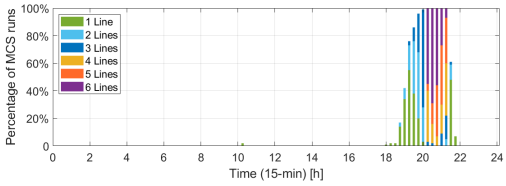

(b) Number of PEV: 20,000

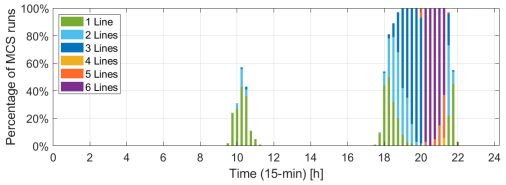

(c) Number of PEV: 30,000

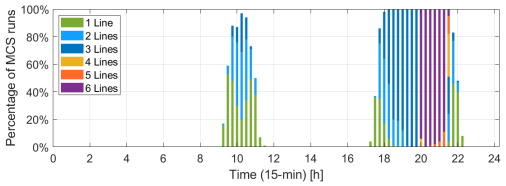

(d) Number of PEV: 40,000

Figure 4.9: No. of Total Tripped Lines

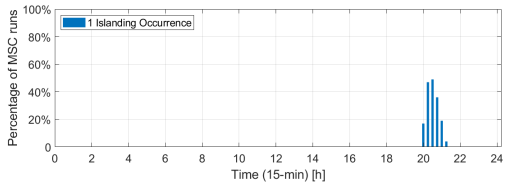

(a) Number of PEV: 10,000

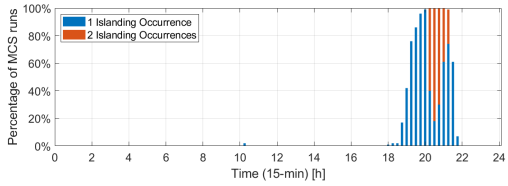

(b) Number of PEV: 20,000

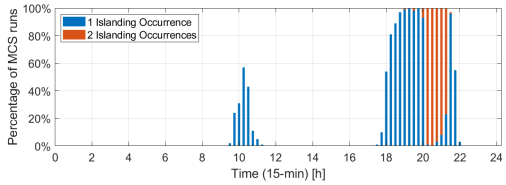

(c) Number of PEV: 30,000

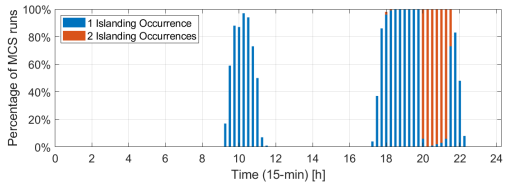

(d) Number of PEV: 40,000

Figure 4.10: No. of Islanding Occurrence

4.4.2 G-CFE Results

Fig. 4.9 and Fig. 4.10 demonstrate the main results in the case study. There are two key metrics in G-CFE output that proved most insightful when performing analysis. These include a) the number of total tripped lines after completing the CFE, *i.e.*, the cardinality of set $\mathcal{O}^*$; and b) the number of islanding occurrence in the CFE, *i.e.*, the cardinality of set $\mathcal{I}^*$.

The y-axis in both figures shows the occurrence percentage of color-coded impact metrics in 100 MCS runs. Compared to the benchmark case where no PEV loads have been integrated into the tested system, the frequency and severity of cascading outages increased with the increasing PEV penetration. In this particular case study, there exists a noticeable difference between the 10,000 and 20,000 PEV cases. In the 10,000 PEV case, there is a maximum probability of approximately 20% for a multi-line (≥ 2) tripping event to occur. However, there was a 100% probability of a first-round line failure that led to cascading outages for the 20,000 PEV case. The 30,000 and 40,000 PEV cases continued such trend with an initial line tripping that almost surely led to cascading outages in a broader range of time. Additionally, for 20,000 $\sim$ 40,000 PEV cases, the system could end up with at most 6 tripped lines and multiple islanding occurrences until stabilized. These observations show that there is not only an increase in the probability of cascading failure but also an increase in the potential severity as the total number of PEV increased.

4.4.3 Performance Evaluation

Result Accuracy

As elaborated in Section 4.3.1, this study adopted a graph based FDPF algorithm, *i.e.,* AC power flow, instead of the commonly used DC power flow in the CFE model. The NPC and HAPC have enabled the proposed model to yield more accurate power flow results without sacrificing computational efficiency. Fig. 4.11 demonstrates the noticeable deviation of G-CFE results between AC and DC power flow algorithm, *ceteris paribus*. As a linear approximation of AC power flow, DC power flow ignores reactive power, assumes lossless transmission line and all bus voltage magnitude to be 1 p.u. Therefore, the CFE tools using DC approximation tends to underestimate the

adverse impact in some cases while overestimating in others, causing inconsistency during analysis.

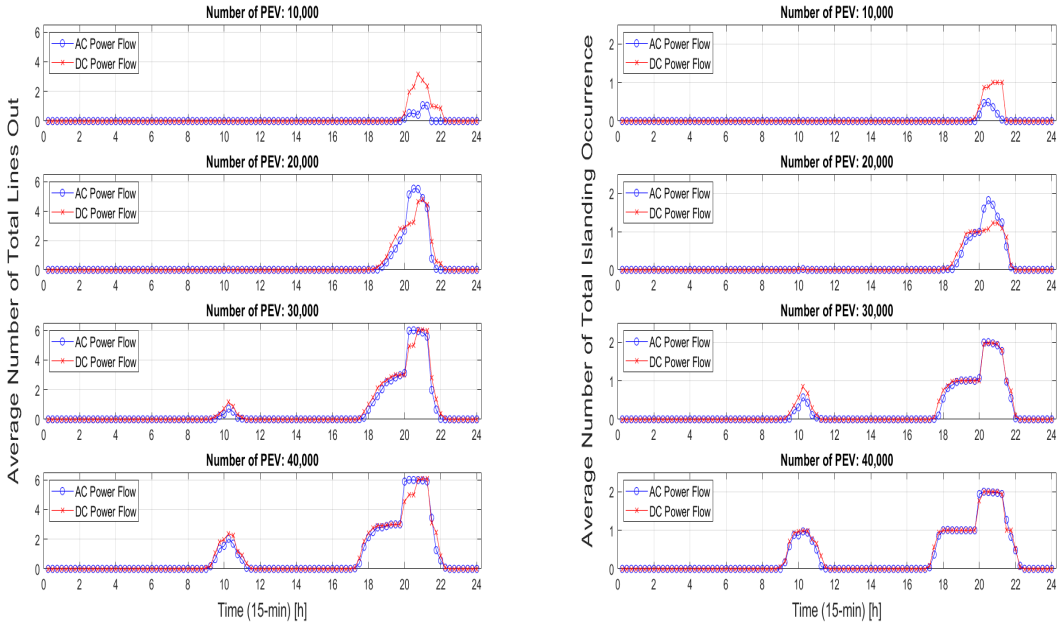

(a) Average No. of Total Tripped Lines (b) Average No. of Islanding Occurrence

Figure 4.11: Performance Comparison of Power Flow Algorithm in G-CFE Model

Computational Efficiency

We benchmark the computational performance of the graph-computing based FDPF with the MATPOWER based FDPF. MATPOWER is an open-source power system simulation tool that scales quite well to large systems, and thus is representative among other software serving as a benchmark. The average computing time of a snapshot power flow for the tested system comparing MATPOWER-FDPF and the proposed method is shown in Table 4.2. The computing time is reduced by enabling

multiple threads through NPC and HAPC in the graph platform. Conversely, due to the sequential implementation in MATPOWER-FDPF, the average computing time is irrelevant to the number of computing threads.

Table 4.2: Computing Time Comparison

Average Computing Time (ms)				
	No. of Threads			
Implementation	1	2	4	8
MATPOWER-FDPF	∼112	∼112	∼112	∼112
Graph-FDPF	33.85	26.99	22.92	20.88

The four functional modules of G-CFE model, *i.e.,* PEV integration, graph-FDPF, line tripping, and island detection, as illustrated in Fig. 4.6, are all implemented in the graph platform with parallel computing enabled. The computing time of each functional module, per iteration per time instant, is shown in Fig. 4.12 to demonstrate its parallelism. With the increasing number of computing threads, the average computing time of each module reduces. Note that the average computing time in Table 4.2 and Fig. 4.12 are calculated by running the case study repetitively 10 times and obtaining the average.

4.5 Summary

The Ultra-Fast Charging Stations (UFCS) could exert disruptive influences on the power grid. This chapter proposes a methodology, a graph-computing based cascading failure evolution (G-CFE) analysis, for assessing and predicting the cascading outages induced by large-scale PEV aggregated at UFCS level on power transmission systems. In comparison to the existing cascading analysis tools, which approximate with DC

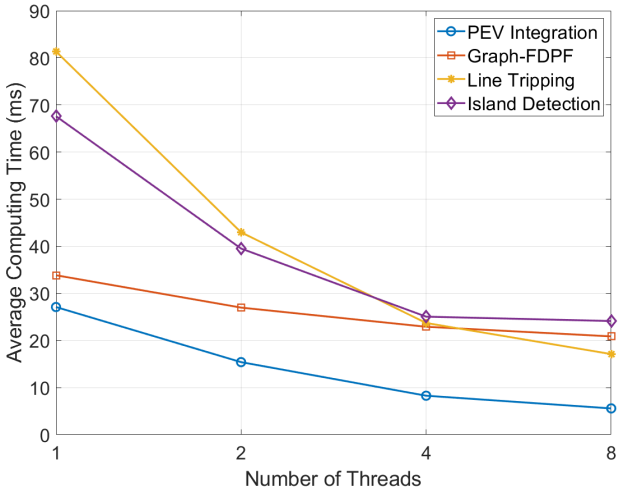

Figure 4.12: Computing Time of Functional Modules in G-CFE Model

power flow or require a long computation time, the proposed method allows utilities and grid operators to actively analyze PEV's disruptive impacts on bulk transmission systems, providing important insights to improve power system reliability.

In the development of G-CFE, this work makes two additional contributions: it a) proposed a graph modeling method, which allows for the flexible model establishment of the power grid with a detailed presentation of PEV charging patterns; and b) developed a method for stochastic cascading failure analysis. The advantages of the proposed method is validated in a provincial power system in China.

Chapter 5: Conclusion and Future Work

5.1 Conclusions

The current electric power grid has been increasingly penetrated with Plug-in Electric Vehicles (PEV). Distinct from traditional electric load, PEV loads are stochastic and impulsive, especially when aggregated at fast charging infrastructure. The PEV loading characteristics make conventional grid impact assessment methods unsuitable. The objective of this dissertation is to propose algorithms and methods for power grid operators and electric utilities to accurately analyze PEV's charging impact on the power system from both distribution and transmission voltage levels. The practical impact metrics provide an important tool to develop proper mitigation strategies through infrastructure planning.

5.2 Contributions

The contributions made in this dissertation are summarized as follows.

5.2.1 Distribution Level PEV Charging Impact

- Provides an approach to accurately and conveniently assess PEV's impact on the grid assets. The PEV charging profiles are pre-processed through Monte-Carlo simulation, which ensures consideration of stochastic charging patterns,

fed into time-series analysis and asset lifetime estimation. The outputs are presented through an integrated interface.

- Inter-temporal response of grid assets is considered. Compared to existing methods, which assess grid assets based on their average loading, the proposed algorithm considers assets' operating frequency and temperature variation. These factors lead to significant differences in the utility assessments.

- The above two engineering advantages are realized under a unified mathematical framework, in which we establish analytic models of two generic classes of grid assets (*i.e.,* continuous and discrete operating assets) and recast their cost functions in the statistical settings of PEV charging. Distinct from simulation-based methods, the proposed method is analytic, and thus greatly reduce the computation resources and data required for accurate assessment.

- Following the integrated algorithm for evaluating PEV's impact on the state of power grid assets, we further introduce a software prototype that serves as an impact visualization tool and predictive planning guideline under the increasing PEV penetration.

5.2.2 Location Planning of PEV Fast Charging Stations

- Proposes a graph modeling scheme for power and transportation coupled network integrated with PEV traffic flows. The representation of different entities' relationship allows for a) fast and easy model establishment; b) efficient implementation of distribution power flow; and c) flexible model extension under expanding networks and increasing PEV penetration.

- The inter-temporal response of grid assets is considered in the power supply aspect of the proposed model, which enables the evaluation of critical equipment' long-term cost over any time span of interest.

- The proposed planning model and cross-entropy optimization solving method are implemented in a graph-computing platform, in which the Node-based Parallel Computing technique has been applied to improve the computational efficiency.

5.2.3 Transmission Level PEV Charging Impact

- Proposes a graph modeling method for PEV-integrated power transmission system, in which the representation of grid topology allows for a) fast model establishment with a faithful presentation of PEV charging patterns at multiple UFCS; and b) efficient implementation of AC power flow.

- Develops an online method for stochastic cascading failure analysis, wherein spatial and temporal stochasticity of the PEV charging behavior are embedded under the umbrella of Monte-Carlo simulation.

- Grounded in the above results, developed a graph-computing based cascading failure evolution (G-CFE) model, which encompasses line-tripping, island-detection, and generation/load re-dispatch in a closed loop.

5.3 Recommendation for Future Work

The recommended future works for this dissertation are summarized as follows.

5.3.1 PEV Charging Impact on Power Grid Asset

In Chapter 2, the integrated algorithm for grid asset impact evaluation and the visualization software prototype based on that are appealing to the industry practitioner, especially utility planner. The future work could extend the functionalities of the visualization interface and incorporate more flexible planning schemes.

5.3.2 Planning of PEV Fast Charging Infrastructure

In Chapter 3, the proposed charging infrastructure location planning model has been validated on a synthesized coupled network. It would be promising to implement the proposed planning model and graph-based solving platform on the real-world, large-scale system in future work. The high-performance graph-computing based solving scheme could be further verified.

5.3.3 Online Prediction for Transmission Cascading Outages

In Chapter 4, the proposed Graph-computing based Cascading Failure Evolution (G-CFE) analysis is the first effort to analyze PEV's disruptive impact on the power transmission systems. More extensive impact metrics based on the developed tool, *e.g.,* N-1 contingency analysis, transient stability analysis, etc., can further improve grid operators' ability to anticipate and prevent possible issues arising under increase penetration of PEV on a large scale. These could be incorporated in future work.

Appendix A: MATLAB Source Code

This appendix includes the MATLAB code used in the simulations of Chapter 3.

```
% This MATLAB function calculates the performance function
    value (objective function in Equation (3.1)) in each
   Cross-Entropy iteration %
% This is the key step of integrated FCS location planning
    problem, as elaborated in Chapter 3 %
function cost = performance_CE_augmented(binary_fcs,
   path_full,shortest_dist,Departure,base_load)
n = 500;
cardi = 25;
[npop,~] = size(binary_fcs);
node_fcs = zeros(npop,cardi);
for i = 1:npop
    node_fcs(i,1:length(find(binary_fcs(i,:)))) = find(
       binary_fcs(i,:));
end
locb = zeros(n,cardi,npop);
for k = 1:npop
    for i = 1:n
        [~,locb(i,:,k)] = ismember(node_fcs(k,:),path_full
           (i,:));
    end
end
fcs_passed = zeros(n,cardi,npop);
first_index = zeros(n,npop);
index = zeros(n,npop);
for k = 1:npop
    for i = 1:n
        B = locb(i,:,k);
        C = min(B(B>0));
```

```
        fcs_passed(i,:,k) = sort(locb(i,:,k));
        if length(unique(fcs_passed(i,:,k)))==2
            first_index(i,k) = 0;
            index(i,k) = 0;
        elseif isempty(C)==1
            first_index(i,k) = 0;
            index(i,k) = 0;
        else
            first_index(i,k) = C;
            temp_index = find(fcs_passed(i,:,k) ==
               first_index(i,k));
            index(i,k) = temp_index(1);
        end
    end
end
Range = 200;
volume = ones(n,npop);
speed = 30;
PEVpower = 120;
starttime = zeros(n,npop);
starttime_quarter = zeros(n,npop);
squares = zeros(n,96,npop);
period = zeros(n,npop);
period_quarter = zeros(n,npop);
endtime = zeros(n,npop);
for m = 1:npop
    for i = 1:n
        if first_index(i,m)==0
            volume(i,m) = 0;
            continue
        end
        if first_index(i,m)~=0
            if path_full(i,first_index(i,m))~=0
                if shortest_dist(path_full(i,1),path_full(
                   i,first_index(i,m)))>=Range/10
                    volume(i,m) = 0;
                elseif shortest_dist(path_full(i,1),
                   path_full(i,first_index(i,m)))>0.5*
                   Range/10 && shortest_dist(path_full(i
                   ,1),path_full(i,first_index(i,m)))<
                   Range/10
```

```
        starttime(i,m) = Departure(i)+
           shortest_dist(path_full(i,1),
           path_full(i,first_index(i,m)))*10/
           speed;
        starttime_quarter(i,m) = ceil(
           starttime(i,m)*4)/4;
        if starttime_quarter(i,m)>=24
            starttime_quarter(i,m) =
               starttime_quarter(i,m)-24;
        end
        period(i,m) = shortest_dist(path_full(
           i,1),path_full(i,first_index(i,m)))
           *10/4/PEVpower;
        period_quarter(i,m) = ceil(period(i,m)
           *4)/4;
        endtime(i,m) = starttime_quarter(i,m)
           + period_quarter(i,m);
        for j = 1:96
            tmp = j/4;
            if tmp >= starttime_quarter(i,m)
               && tmp < endtime(i,m)
                squares(i,j,m) = PEVpower;
            end
        end
    elseif shortest_dist(path_full(i,1),
       path_full(i,first_index(i,m)))<=0.5*
       Range/10
        if index(i,m) == cardi
            volume(i,m) = 0;
            continue
        end
        for k = 1:cardi-index(i,m)
            if path_full(i,fcs_passed(i,index(
               i,m)+k,m))~=0
                if shortest_dist(path_full(i
                   ,1),path_full(i,fcs_passed(
                   i,index(i,m)+k,m)))>0.5*
                   Range/10
```

```
                starttime(i,m) = Departure
                   (i)+ shortest_dist(
                   path_full(i,1),
                   path_full(i,fcs_passed(
                   i,index(i,m)+k,m)))
                   *10/30;
                starttime_quarter(i,m) =
                   ceil(starttime(i,m)*4)
                   /4;
                if starttime_quarter(i,m)
                   >=24
                    starttime_quarter(i,m)
                        =
                       starttime_quarter(i
                       ,m)-24;
                end
                period(i,m) =
                   shortest_dist(path_full
                   (i,1),path_full(i,
                   fcs_passed(i,index(i,m)
                   +k,m)))*10/4/PEVpower;
                period_quarter(i,m) = ceil
                   (period(i,m)*4)/4;
                endtime(i,m) =
                   starttime_quarter(i,m)
                   + period_quarter(i,m);
                for j = 1:96
                    tmp = j/4;
                    if tmp >=
                       starttime_quarter(i
                       ,m) && tmp <
                       endtime(i,m)
                         squares(i,j,m) =
                            PEVpower;
                    end
                end
                break
            end
        end
        if k==cardi-index(i,m)
            volume(i,m) = 0;
        end
    end
```

```
                end
            end
        end
    end
end
cost = zeros(npop,1);
for k = 1:npop
    aaa = sum(squares);
    Profile_unit = aaa(1,:,k);
    Volume = sum(volume);

    margin = 0.05;
    DC = 120;
    DC_hour = DC/35040;
    RF = 0.81;
    int = 0.05;
    r = 0.0322;
    g = 0.01;
    N = 24;
    yr = 15.41;
    FCR = 0.1211;
    Total_rating_TF = 10000;
    [row,column] = size((Profile_unit'+(base_load*10000)))
       ;
    K_factor_3002_500RIDE = (Profile_unit'+(base_load
       *10000))/Total_rating_TF;
    faa_3002_500RIDE=zeros(row,column);
    feqa_3002_500RIDE = zeros(1,column);
    LOL_3002_500RIDE = zeros(1,column);
    for i = 1:column

        hours = 96;
        Qa = 30;
        Qhs_yearly = zeros(hours,1);
        Dt = 15; k22 = 2; t_w = 5; k21 = 2; del_th_hr =
           40; y = 1.3;
        t_o = 150; k11 = 0.5; R = 10; x = 0.9; del_th_or =
            60;
        del_th_h1 = zeros(hours,1);
        del_th_h2 = zeros(hours,1);
        th_o = zeros(hours,1);
        del_th_h1(1) = 53.2;
        del_th_h2(1) = 26.6;
```

```
    th_o(1) = 63.9;
    Qhs_yearly(1) = th_o(1)+del_th_h1(1) - del_th_h2
       (1);
    for j=2:hours
        del_th_h1(j) = del_th_h1(j-1) + (Dt/(k22*t_w))
           *(k21*del_th_hr*(K_factor_3002_500RIDE(j,i)
           ^y)-del_th_h1(j-1));
        del_th_h2(j) = del_th_h2(j-1) + ((Dt*k22)/t_o)
           *((k21-1)*del_th_hr*(K_factor_3002_500RIDE(
           j,i)^y)-del_th_h2(j-1));
        th_o(j) = th_o(j-1) + (Dt/(k11*t_o))*((((1+(
           K_factor_3002_500RIDE(j,i)^2)*R)/(1+R))^x)*
           del_th_or-(th_o(j-1) - Qa));
        Qhs_yearly(j) = th_o(j) + del_th_h1(j) -
           del_th_h2(j);
    end
    faa_3002_500RIDE(:,i) = exp(((15000/383)-(15000./(
       Qhs_yearly + 273))));
    feqa_3002_500RIDE(:,i) = 0.25*sum(faa_3002_500RIDE
       (:,i))/24;
    LOL_3002_500RIDE(:,i) = (feqa_3002_500RIDE(:,i)
       *24/135000)*100;
end
LOL = LOL_3002_500RIDE;
if 100/(LOL_3002_500RIDE*365)<yr
    yr_PEV = 100/(LOL_3002_500RIDE*365);
else
    yr_PEV = 15.41;
end
peak_300 = max((Profile_unit'+(base_load*10000)));
X = (1+r)/(1+int);
CRF_mod_300 = ((int*(1+int)^yr_PEV)/((1+int)^yr_PEV-1)
   );
PL_square_mod_300 = (peak_300/Total_rating_TF)^2*(((1+
   int)^yr_PEV - (1+g)^(2*yr_PEV))/((1+int)^yr_PEV *
   ((1+int)-(1+g)^2)))*CRF_mod_300;
load_factor_300  = (Profile_unit'+(base_load*10000))/
   peak_300;
LoF_mod_300 = 0.2*load_factor_300+0.8*(load_factor_300
   ).^2;
A_mod_300 = ((DC+(N*margin))/FCR)*X*((1-X^yr_PEV)/(1-X
   ))*CRF_mod_300;
```

```
    B_mod_unit_300 = PL_square_mod_300*((RF*DC_hour) +
       LoF_mod_300*(margin/4));
    B_mod_sum_300 = (sum(B_mod_unit_300)/FCR)*X*((1-X^
       yr_PEV)/(1-X))*CRF_mod_300;
    TCO_modified = 70000*LOL+A_mod_300*13.2+B_mod_sum_300
       *53;
    cost_daily = TCO_modified/(yr_PEV*365);

    cost(k) = cost_daily + nnz(binary_fcs(k,:))*0.5 -
       Volume(k)*0.1;
end
end

% get random departure time for 500 PEV fleets %
Dep_time = (randi(97,[500,1])-1)/4;

% get 500 random OD pairs of PEV %
n = 500;
OD = zeros(n,2);
for i = 1:n
    OD(i,:) = randperm(25,2);
end

% input the transportation graph component (vertex and
   edge) and generate the detailed trip chains by shortest
   -distance algorithm %
n = 500; %number of PEVs
G = graph(s,t,weights);
plot(G,'EdgeLabel',G.Edges.Weight);

%find shortest path for 500 PEVs and get the intermediate
   nodes for all PEV
path = zeros(n,20);
dist = zeros(n,1);
for i = 1:n
    [p,d] =shortestpath(G,O(i),D(i));
    path(i,1:(length(p)-2)) = p(2:(end-1));
    dist(i) = d;
end
path_truncate = path;
path_truncate(:,~any(path_truncate,1)) = [];
```

Appendix B: Graph Computing Implementation

This appendix includes the graph computing implementation source code used in Chapter 3 and Chapter 4, written in Graph-SQL, C++ and Linux shell scripting language.

```
// Graph schema of the 25-node transportation network
   coupled with the 123-node distribution test feeder, as
   the case study in Chapter 3

// Power Distribution System Graph
CREATE VERTEX bus_D (primary_id cid string, exId string,
   flag uint, IDNO uint, bus_type uint, PdA double, QdA
   double, PdB double, QdB double, PdC double, QdC double,
    DGvoltage_A double, DGvoltage_B double, DGvoltage_C
   double, DG_Type string, CapA double, CapB double, CapC
   double, Load_Model string, BW_reg double, PT_reg double
   , CT_reg double, vol_reg_A double, vol_reg_B double,
   vol_reg_C double, control_phase_reg string, Tap_A int,
   Tap_B int, Tap_C int, Vbase double, node_phases string,
    area uint, pos_x double, pos_y double, loc_x double,
   loc_y double, Pab_tri double, PF_tri double, CapA_cal
   double, CapB_cal double, CapC_cal double, PdA_cal
   double, QdA_cal double, PdB_cal double, QdB_cal double,
    PdC_cal double, QdC_cal double, PdAB_cal double,
   QdAB_cal double, PdBC_cal double, QdBC_cal double,
   PdCA_cal double, QdCA_cal double, VAmag_cal double,
   VAang_cal double, VBmag_cal double, VBang_cal double,
   VCmag_cal double, VCang_cal double, V_unbalance double,
    startnode string) WITH  STATS="OUTDEGREE_BY_EDGETYPE"
```

```
CREATE DIRECTED EDGE backe_D (from bus_D, to bus_D,
   edge_name string, flag uint, Nt double, connection_T
   string, Raa double, Rab double, Rac double,Rba double,
   Rbb double, Rbc double,Rca double, Rcb double, Rcc
   double, Xaa double, Xab double, Xac double, Xba double,
    Xbb double, Xbc double, Xca double, Xcb double, Xcc
   double, Baa double, Bab double, Bac double, Bba double,
    Bbb double, Bbc double, Bca double, Bcb double, Bcc
   double,linelength double, Config string, PdA_dis double
   , QdA_dis double, PdB_dis double, QdB_dis double,
   PdC_dis double, QdC_dis double, Load_Model_dis string,
   Int_1_x double, Int_1_y double, Int_2_x double, Int_2_y
    double, Int_3_x double, Int_3_y double, IAmag_cal
   double, IAang_cal double, IBmag_cal double, IBang_cal
   double, ICmag_cal double, ICang_cal double)

CREATE DIRECTED EDGE foree_D (from bus_D, to bus_D,
   edge_name string, flag uint, Nt double, connection_T
   string, Raa double, Rab double, Rac double,Rba double,
   Rbb double, Rbc double,Rca double, Rcb double, Rcc
   double, Xaa double, Xab double, Xac double, Xba double,
    Xbb double, Xbc double, Xca double, Xcb double, Xcc
   double, Baa double, Bab double, Bac double, Bba double,
    Bbb double, Bbc double, Bca double, Bcb double, Bcc
   double, linelength double, Config string, PdA_dis
   double, QdA_dis double, PdB_dis double, QdB_dis double,
    PdC_dis double, QdC_dis double, Load_Model_dis string,
    Int_1_x double, Int_1_y double, Int_2_x double,
   Int_2_y double, Int_3_x double, Int_3_y double,
   IAmag_cal double, IAang_cal double, IBmag_cal double,
   IBang_cal double, ICmag_cal double, ICang_cal double)

CREATE VERTEX  switchnode_D (primary_id cid string,  exId
   string, switch_phases string, from_bus string, to_bus
   string, switch_status string, flag uint, Config string,
    loc_x double, loc_y double, startnode string)

CREATE VERTEX  customer_D (primary_id cid string,  exId
   string, loadpoint string, PA double, QA double, PB
   double, QB double, PC double, QC double)
```

```
CREATE DIRECTED EDGE switchlinkF_D (from bus_D, to
   switchnode_D,  flag uint )

CREATE DIRECTED EDGE switchlinkT_D (from switchnode_D, to
   bus_D,  flag uint )

CREATE DIRECTED EDGE customerlink_D (from bus_D, to
   customer_D,  edge_name string )

CREATE DIRECTED EDGE link_D (from bus_D, to bus_D, Raa
   double, Rab double, Rac double,Rba double, Rbb double,
   Rbc double,Rca double, Rcb double, Rcc double, Xaa
   double, Xab double, Xac double, Xba double, Xbb double,
    Xbc double, Xca double, Xcb double, Xcc double, Gaa
   double, Gab double, Gac double, Gba double, Gbb double,
    Gbc double, Gca double, Gcb double, Gcc double, Baa
   double, Bab double, Bac double, Bba double, Bbb double,
    Bbc double, Bca double, Bcb double, Bcc double, hBaa
   double, hBab double, hBac double, hBba double, hBbb
   double, hBbc double, hBca double, hBcb double, hBcc
   double, K double, flag int) with reverse_edge="
   reverse_link_D"

// Transportation network graph
TYPEDEF TUPLE <rowindex INT, h1 DOUBLE,h2 DOUBLE,h3 DOUBLE
   ,h4 DOUBLE,h5 DOUBLE,h6 DOUBLE,h7 DOUBLE,h8 DOUBLE,h9
   DOUBLE,h10 DOUBLE,h11 DOUBLE,h12 DOUBLE,h13 DOUBLE,h14
   DOUBLE,h15 DOUBLE,h16 DOUBLE,h17 DOUBLE,h18 DOUBLE,h19
   DOUBLE,h20 DOUBLE,h21 DOUBLE,h22 DOUBLE,h23 DOUBLE,h24
   DOUBLE,
h25 DOUBLE> ShortDistance

CREATE VERTEX node_trans(primary_id nId int, exId int,
   coupled_bus int, IDNO int, weight double, loc_x double,
    loc_y double, Short_D ShortDistance) WITH STATS="
   OUTDEGREE_BY_EDGETYPE"

CREATE DIRECTED EDGE link_trans(from node_trans, to
   node_trans, edge_name string, length double, speed_rush
    double, speed_other double) with reverse_edge="
   reverse_link_trans"
```

```
CREATE DIRECTED EDGE conn_coupled_D(from node_trans, to
   bus_D)

// Traffic flow graph
// 500 PEV flows
CREATE VERTEX node_traffic(primary_id vId string, exId
   string, N1 uint, N2 uint, N3 uint, N4 uint, N5 uint, N6
    uint, N7 uint, N8 uint, N9 uint, N10 uint, Dist double
   , Departure double) WITH STATS="OUTDEGREE_BY_EDGETYPE"

//The "Sample" vertex to store N sample feasible solutions
CREATE VERTEX sample_sol(primary_id sId string, exId
   string) WITH STATS="OUTDEGREE_BY_EDGETYPE"

create graph powerflow_graph(bus_D, backe_D, foree_D,
   switchnode_D, switchlinkF_D, switchlinkT_D, customer_D,
    customerlink_D, link_D, node_trans, link_trans,
   conn_coupled_D, node_traffic, YearIndex, MonthIndex,
   DayIndex, Y2M, M2D, ofDay, reactive, curr, voltage,
   powerfactor, energy, YIndex, MIndex, DIndex, Yr2Mo,
   Mo2Day, VoltageA, VoltageB, VoltageC, sample_sol)

EXPORT SCHEMA powerflow_graph



// Loading grid data into the defined graph schema:
set sys.data_root="./input"
DROP JOB load_powerflow_D

CREATE LOADING JOB load_powerflow_D FOR graph
   powerflow_graph
{
        load "./input/Node123bus_IES.csv"
        TO VERTEX bus_D VALUES($"bus_id",$0,$1,$2,$3,$4,$5
           ,$6,$7,$8,$9,$10,$11,$12,$13,$14,$15,$16,$17,
           $18,$19,$20,$21,$22,$23,$24,$25,$26,$27,$28,$29
           ,_,$30,$31,$32,$33,_,_,_,_,_,_,_,_,_,_,_,_,_,_,
           _,_,_,_,_,_,_,_,_,_,_,_,_,_),
        TO VERTEX switchnode_D VALUES($"switch_id",$34,$35
           ,$36,$37,$38,$39,$40,$41,$42,_)
        using Separator=",", Header="true";
```

```
// FCS planning related loading jobs
load "./input/Node_transportation.csv"
TO VERTEX node_trans values($"transnode_id",$0,$1,
   $2,$3,$4,$5,ShortDistance($0,$6,$7,$8,$9,$10,
   $11,$12,$13,$14,$15,$16,$17,$18,$19,$20,$21,$22
   ,$23,$24,$25,$26,$27,$28,$29,$30)),
TO EDGE conn_coupled_D values($0,$1) //The edge
   coupling power and transportation network
using Separator=",", Header="true";

load "./input/Link_transportation.csv"
TO EDGE link_trans values($0,$1,_,$2,$3,$4)
using Separator=",", Header="true";

load "./input/Node_traffic.csv"
TO VERTEX node_traffic values($"PEV_id",$0,$1,$2,
   $3,$4,$5,$6,$7,$8,$9,$10,$11,$12)
using Separator=",", Header="true";

load "./input/sample.csv"
TO VERTEX sample_sol values($"sample_id",$0)
using Separator=",", Header="true";

load "./input/Lineconfig123bus.csv"
TO VERTEX lineconfig_D VALUES($"config_id",$0,$1,
   $2, $3, $4, $5, $6, $7, $8, $9,$10,$11,$12,$13,
   $14,$15,$16,$17,$18,$19,$20,$21,$22,$23,$24,$25
   ,$26,$27,$28,$29,$30,$31,$32,$33,$34)
using Separator=",", Header="true";

load "./input/Branch123bus_IES.csv"
TO EDGE backe_D  values($1,$0,_,$2,$3,$4,$5,$6,$7,
   $8,$9,$10,$11,$12,$13,$14,$15,$16,$17,$18,$19,
   $20,$21,$22,$23,$24,$25,$26,$27,$28,$29,$30,$31
   ,$32,$33,$34,$35,$36,$37,$38,$39,$40,$41,$42,
   $43,$44,$45,$46,_,_,_,_,_,_,_),
TO EDGE foree_D  values($0,$1,_,$2,$3,$4,$5,$6,$7,
   $8,$9,$10,$11,$12,$13,$14,$15,$16,$17,$18,$19,
   $20,$21,$22,$23,$24,$25,$26,$27,$28,$29,$30,$31
   ,$32,$33,$34,$35,$36,$37,$38,$39,$40,$41,$42,
   $43,$44,$45,$46,_,_,_,_,_,_,_),
TO EDGE switchlinkF_D  values($47,$48,$49),
```

```
        TO EDGE switchlinkT_D  values($50,$51,$52)
    using Separator=",", Header="true";

        load "./input/Node_transportation.csv"
        TO EDGE conn_coupled_D values($0,$1)
        using Separator=",", Header="true";

        load "./input/transformer.csv"
        TO EDGE transformer_D  values($0,$1,$2,$3,$4,$5,$6
           ,$7,$8,$9,$10,$11,$12,$13,$14,$15,$16,$17)
        using Separator=",", Header="true";

        load "./input/renewable.csv"
        TO EDGE XF_res_D  values($0,$1,$2,$3,$4,$5,$6,$7,
           $8,$9,$10,$11,$12,$13,$14,$15,$16,$17)
        using Separator=",", Header="true";

     load "./input/nodeCEO.csv"
        TO VERTEX DG          VALUES($"DGID",$"DGID",_),
        TO VERTEX prob        VALUES($"probID",$"probID",_,
           _),
        TO VERTEX planSample VALUES($"sampleID",$"sampleID
           ",_),
        TO VERTEX plan        VALUES($"planID",$"planID",_,
           _,_,_,_),
        TO EDGE   getProb     VALUES($"probCopy",$"sampleID
           ")
        using Separator=",", Header="true";
}

clear graph store -HARD
RUN LOADING JOB load_powerflow_D



// The following query implements Cross-Entropy algorithm
   in graph-computing platform to solve for integrated FCS
    location planning problem in Chapter 3

CREATE QUERY Flow_capture(int NumSample, double alpha,
   double ratio) FOR GRAPH powerflow_graph
{
```

```
TYPEDEF tuple <double cost, double h1, double h2, double
   h3, double h4, double h5, double h6, double h7, double
   h8, double h9, double h10, double h11, double h12,
   double h13, double h14, double h15, double h16, double
   h17, double h18, double h19, double h20, double h21,
   double h22, double h23, double h24, double h25> costtup
   ;

// Initialization

ListAccum<costtup> @@strategy;
SumAccum<double> @@cost_single;
ListAccum<int> @List;
SumAccum<double> @cost;
SumAccum<double> @@Best;
SumAccum<double> @@Mean;
SumAccum<double> @@Diff;
MaxAccum<float> @@Max_diff;
ArrayAccum<SumAccum<double>> @@prob[25];
ArrayAccum<SumAccum<double>> @@prob_last[25];
@@cost_single = 0;
@@Max_diff = 10000;

//@@prob is the evolving solution vector
FOREACH k IN RANGE[0,24] DO
        @@prob[k] += 0.5;
END;

FOREACH k IN RANGE[0,24] DO
        @@prob_last[k] = @@prob[k];
END;

//clear
@@strategy.clear();

T0 = {node_traffic.*};
T1 = {node_trans.*};
T2 = {sample_sol.*};

// starting Cross-Entropy Optimization Algorithm
while @@Max_diff >= 0.05 limit 10 do
        print @@Best;
```

```
  print @@prob TO_CSV "/home/tigergraph/output/
     solution.csv";

  foreach j in range[0,24] do
          @@prob[j] = alpha * @@prob[j] + (1-alpha)
             * @@prob_last[j];
  end;

  CallSet = select s from T2:s
Post-Accum
s.@List = [0,0,0,0,0,0,0,0,0,0,0,0,
          0,0,0,0,0,0,0,0,0,0,0,0,0],
foreach i in range[0,24] do
  s.@List.update(i,get_random(@@prob[i]))
end,
//parse s.@List into a string binary_str
string binary_str = "",
foreach i in range[0,24] do
  binary_str = binary_str + "\"" + to_string(i+1) +
     "\"" + ":" + to_string(s.@List.get(i)) + ","
end,
binary_str = "{" + trim(TRAILING "," FROM binary_str
   ) + "}",
//pass the string binary_str into get_cost() query
   to return the sample cost
s.@cost = get_cost(binary_str),
@@strategy += costtup(s.@cost, s.@List.get(0), s.
   @List.get(1), s.@List.get(2), s.@List.get(3), s.
   @List.get(4), s.@List.get(5), s.@List.get(6), s.
   @List.get(7), s.@List.get(8), s.@List.get(9), s.
   @List.get(10), s.@List.get(11), s.@List.get(12),
   s.@List.get(13), s.@List.get(14), s.@List.get(15)
   , s.@List.get(16), s.@List.get(17), s.@List.get
   (18), s.@List.get(19), s.@List.get(20), s.@List.
   get(21), s.@List.get(22), s.@List.get(23), s.
   @List.get(24));

  foreach m in range[0,24] do
          @@prob_last[m] = @@prob[m];
  end;

  @@Best = update_strategy(@@strategy, @@prob,
     NumSample, ratio);
```

```
        @@Max_diff = 0;

        foreach x in range[0,24] do
                @@Max_diff += abs(abs(@@prob_last[x]) -
                   abs(@@prob[x]));
        end;

        @@Mean = get_cost_mean(@@strategy, NumSample,
           ratio);
        @@Diff = abs(abs(@@Mean) - abs(@@Best));
        print @@Max_diff;

end;
}
INSTALL QUERY Flow_capture



// Graph schema of the provincial transmission system in
   Sichuan, China, as the case study in Chapter 4

// Transmission System Graph
create vertex Gnode (primary_id cid string, exId uint,
   flag uint, Pg double, Qg double, Vm double, Vr double,
   Vs double, qUp double, qLower double, Pld double, Qld
   double, V1 double, G double, B double, EV_conn int,
   EV_P double, Ratio_PL double, Ratio_QL double, Ratio_PG
    double, Ratio_QG double, base_kV double, ifisland int,
    bus_name string) with stats="OUTDEGREE_BY_EDGETYPE"

// Add EV_conn to set up EV connection with Gnode, add
   EV_P to attach EV (load) profile to Gnode
create directed edge connected (from Gnode, to Gnode, G
   double, B double, hB double, K double, Kcount int, BIJ
   double, flag int, P_TLPF double, Q_TLPF double, CAP
   double, reverse int, I_lim double, status int)

// Transportation graph
CREATE VERTEX EV(primary_id vId string, exId string, flag
   int, EV_P double) WITH STATS="OUTDEGREE_BY_EDGETYPE"
```

```
CREATE DIRECTED EDGE EV2BUS(from EV, to Gnode, busname
   string, selection int) with reverse_edge="
   reverse_link_trans"

create graph cascading_graph(Gnode, connected, EV, EV2BUS)

EXPORT SCHEMA cascading_graph



// Loading grid data into the defined graph schema:
DROP JOB load_cascading

CREATE LOADING JOB load_cascading FOR graph
   cascading_graph
{
//loading job for transmission system
load "$sys.data_root/sc_20180824_10500nodeinfo.csv"
to vertex Gnode values($"bus_id",$0, $"type", $"
   generation_p", $"generation_Q", $"voltage", $"voltage",
    $"angle", $"MAX_Q", $"Min_Q", $"load_P", $"load_Q", $"
   angle", $"G", $"B", $"EV_conn", _, $"ratio_PL", $"
   ratio_QL", $"ratio_PG", $"ratio_QG", $"base_kV", $"
   ifisland", $"bus_name")
using Separator=",", Header="true";

//loading job for PEV profile
// switch between different number of total PEVs
load "$sys.data_root/Vertex_EV.csv"
TO VERTEX EV values($"PEV_id",$0,$1,$2)
using Separator=",", Header="true";

load "$sys.data_root/sc_20180824_10500edgeinfo.csv"
to edge connected values($0, $1,reduce(add(_getG($"R", $"X
   ")))),reduce(add(_getB($"R", $"X"))), reduce(add($"B")),
    reduce(add($"transformer_final_turns_ratio")), reduce(
   add(1)), reduce(add(divide($"X"))),$"type", _, _,
   reduce(add($29)), 1, reduce(add($"limit")), $"status"),
```

```
to edge connected values($1, $0,reduce(add(_getG($"R", $"X
   ")))),reduce(add(_getB($"R", $"X"))), reduce(add($"B")),
    reduce(add(_minus($"transformer_final_turns_ratio"))),
    reduce(add(1)), reduce(add(divide($"X"))),$"type", _,
   _, reduce(add($29)), -1, reduce(add($"limit")), $"
   status")
using  Separator=",", Header="true";

//loading job for PEV-BUS connection
// switch between different number of total PEVs
load "$sys.data_root/Edge_EV2BUS.csv"
TO EDGE EV2BUS values($0,$1,$2, _)
using Separator=",", Header="true";
}

clear graph store -HARD
RUN LOADING JOB load_cascading



// The following queries are performing necessary graph
   operations for the Graph-computing based Cascading
   Failure Evolution (G-CFE) model

drop query EV_assign
drop query cfe_model
drop query island_detect

create query EV_assign (vertex s, int MC) for graph
   cascading_graph
{
SumAccum<double> @EV_P;
        T0 = {s};
        T0 = select v from T0:v - (:e) - Gnode:t
         where t.EV_conn == MC
         accum
         e.selection = 1;
}
install query EV_assign

// Define G-CFE query
```

```
create query cfe_model(int i,int j) FOR GRAPH
   cascading_graph returns (SumAccum<int>)
{
 typedef tuple<double p_flow, double capacity>
    triplineflowtup;
 ListAccum<triplineflowtup> @@TripLineFlow;
 ListAccum<string> @@Trippedline;
 SumAccum<int> @@Status = 0;
 MapAccum<int,int> @reverseMap;

 @@TripLineFlow.clear();

 T0 = {Gnode.*};

 // Set the status of overloading line to be 0 (trip it!)
    and record the name of tripped line
 TripSet = select s from T0:s - (connected:e)-> Gnode:t
   where ((e.status == 1 and abs(e.CAP) != 0 and e.K == 0
      and abs(e.P_TLPF) > e.CAP and s.base_kV <= 220 and t
      .base_kV >= 10) or (e.status == 1 and abs(e.CAP) !=
      0 and e.K != 0 and abs(e.P_TLPF) > e.CAP))
   accum
   e.status = 0,
   s.@reverseMap += (t.exId -> 1),
   @@Trippedline += s.bus_name + "-" + t.bus_name + ",␣",
   @@TripLineFlow += triplineflowtup(e.P_TLPF, e.CAP),
   @@Status += 1;

  reverseSet = select s from T0:s - (connected:e) -> Gnode
     :t
         where (e.status == 1)
         accum
         IF (t.@reverseMap.containsKey(s.exId) == true and
            s.@reverseMap.containsKey(t.exId) == false)
            THEN
                  e.status = 0,
                  @@Status += 1,
                  @@Trippedline += s.bus_name + "-" + t.
                     bus_name + ",␣",
                  @@TripLineFlow += triplineflowtup(e.P_TLPF
                     , e.CAP)
         END;
```

```
        print "Tripped_Line" + "," + "Line_Flow" + "," + "
           Line_Capacity" + "," + "MC:" + TO_STRING(i) + "
           ," + "Time:" + TO_STRING(j+1) TO_CSV "/home/
           tigergraph/cascading_failure_PEV/output/
           tripped_line.csv";
        print @@Trippedline TO_CSV "/home/tigergraph/
           cascading_failure_PEV/output/tripped_line.csv";
        print @@TripLineFlow TO_CSV "/home/tigergraph/
           cascading_failure_PEV/output/tripped_line.csv";

        return @@Status/2;
}
install query cfe_model

// Define island detection query
create query island_detect() FOR GRAPH cascading_graph
   returns (SumAccum<int>)
{
 SumAccum<int> @visited = 0;
 SumAccum<int> @island = 0;
 SumAccum<int> @@NumofNodes = 0;
 SumAccum<int> @@Counter = -1;
 SumAccum<int> @@islandcounter = 0;
 SumAccum<double> @@Net;
 SumAccum<double> @@SumPg;
 SumAccum<double> @@SumPld;
 T0 = {Gnode.*};

  // Islanding detection
  SlackSet = select s from T0:s
        where (s.flag == 3)
        post-accum
        s.@visited = 1,
        @@NumofNodes += 1,
        @@SumPg += s.Pg,
        @@SumPld += s.Pld;

  while (@@Counter != 0) do
        @@Counter = 0;
        SlackSet = select t from SlackSet:s - (connected:e
           )-> Gnode:t
        where (e.status == 1 and t.@visited == 0)
        post-accum
```

```
        t.@visited = 1,
        @@Counter += 1,
        @@NumofNodes += 1,
        t.@island = 1,
        t.ifisland = 1,
        @@SumPg += t.Pg,
        @@SumPld += t.Pld;
  end;

  //The following block is to calculate the net power of
     all island nodes
  IF (@@NumofNodes != T0.size()) THEN
    islandSet = select s from T0:s
        where (s.@visited == 0)
        post-accum
        @@Net += s.Pg - s.Pld,
        @@SumPg += s.Pg,
        @@SumPld += s.Pld;

  //The following block is to conduct load shedding or
     generation curtail
        IF (@@Net >= 0 ) THEN
                sheddingSet = select s from T0:s
                  where (s.@visited == 1)
                  post-accum
                  s.Pld = s.Pld * (1 - @@Net/@@SumPld);
        ELSE IF (@@Net < 0) THEN
                sheddingSet = select s from T0:s
                  where (s.@visited == 1)
                  post-accum
                  s.Pg = s.Pg * (1 + @@Net/@@SumPg);
        END;
  END;

        return @@NumofNodes;
}

install query island_detect
```

Bibliography

[1] Sumedha Rajakaruna, Farhad Shahnia, and Arindam Ghosh. *Plug in electric vehicles in smart grids: charging strategies*. Springer, 2014.

[2] US EIA. Annual energy outlook 2015: with projections to 2040. 2017.

[3] Steven J Skerlos and James J Winebrake. Targeting plug-in hybrid electric vehicle policies to increase social benefits. *Energy Policy*, 38(2):705–708, 2010.

[4] IEA. Global EV Outlook 2019. Technical report, 2019.

[5] PETER O'Connor. 40% Growth? The Latest Electric Vehicle Sales Numbers Look Good, July 2017.

[6] Reuters. China targets 35 million vehicle sales by 2025, NEVs to make up one-fifth, April 2017.

[7] Eshe Nelson. Norway is planning to pull the plug on its wildly successful electric-car incentives, Octerber 2017.

[8] ORTEC. Market impact of Dutch electric vehicle sales targets, May 2017.

[9] Bronwyn Lauten. EVs – findings from Japan, July 2015.

[10] Scott Hardman, Eric Shiu, and Robert Steinberger-Wilckens. Changing the fate of fuel cell vehicles: Can lessons be learnt from tesla motors? *International Journal of Hydrogen Energy*, 40(4):1625–1638, 2015.

[11] John Voelcker. Porsche's fast-charge power play. *IEEE Spectrum*, 56(09):30–37, 2019.

[12] Zhenya Ji and Xueliang Huang. Plug-in electric vehicle charging infrastructure deployment of china towards 2020: Policies, methodologies, and challenges. *Renewable and Sustainable Energy Reviews*, 90:710–727, 2018.

[13] Murat Yilmaz and Philip T Krein. Review of Battery Charger Topologies, Charging Power Levels, and Infrastructure for Plug-in Electric and Hybrid Vehicles. *IEEE Transactions on Power Electronics*, 28(5):2151–2169, 2013.

[14] Hussain Shareef, Md Mainul Islam, and Azah Mohamed. A Review of the Stage-of-the-art Charging Technologies, Placement Methodologies, and Impacts of Electric Vehicles. *Renewable and Sustainable Energy Reviews*, pages 403–420, 2016.

[15] SAE Hybrid Committee et al. SAE Charging Configurations and Ratings Terminology. *Society of Automotive Engineers*, 2011.

[16] Jiankang Wang. Toward resilience of the electric grid. *Smart Cities: Foundations, Principles, and Applications*, pages 535–574, 2017.

[17] Júlio César Guerra Justino, Thiago Morais Parreiras, and Braz J Cardoso Filho. Hundreds kw charging stations for e-buses operating under regular ultra-fast charging. *IEEE Transactions on Industry Applications*, 52(2):1766–1774, 2015.

[18] IEA. Global EV Outlook 2018. Technical report, 2018.

[19] Robert C Green II, Lingfeng Wang, and Mansoor Alam. The impact of plug-in hybrid electric vehicles on distribution networks: A review and outlook. *Renewable and sustainable energy reviews*, 15(1):544–553, 2011.

[20] Ahmed MA Haidar and Kashem M Muttaqi. Behavioral characterization of electric vehicle charging loads in a distribution power grid through modeling of battery chargers. *IEEE Transactions on Industry Applications*, 52(1):483–492, 2015.

[21] Rong-Ceng Leou, Jen-Hao Teng, and Chun-Lien Su. Modelling and verifying the load behaviour of electric vehicle charging stations based on field measurements. *IET Generation, Transmission & Distribution*, 9(11):1112–1119, 2015.

[22] Arturs Purvins, Catalin-Felix Covrig, and Georgios Lempidis. Electric vehicle charging system model for accurate electricity system planning. *IET Generation, Transmission & Distribution*, 12(17):4053–4059, 2018.

[23] Gillian Lacey, Ghanim Putrus, and Edward Bentley. Smart ev charging schedules: supporting the grid and protecting battery life. *IET Electrical Systems in Transportation*, 7(1):84–91, 2016.

[24] Zhe Wei, Yue Li, and Lin Cai. Electric vehicle charging scheme for a park-and-charge system considering battery degradation costs. *IEEE Transactions on Intelligent Vehicles*, 3(3):361–373, 2018.

[25] Anamika Dubey and Surya Santoso. Electric vehicle charging on residential distribution systems: Impacts and mitigations. *IEEE Access*, 3:1871–1893, 2015.

[26] Rong-Ceng Leou, Jen-Hao Teng, Heng-Jiu Lu, Bo-Ren Lan, Hong-Ting Chen, Ting-Yen Hsieh, and Chun-Lien Su. Stochastic analysis of electric transportation charging impacts on power quality of distribution systems. *IET Generation, Transmission & Distribution*, 12(11):2725–2734, 2018.

[27] Nafeesa Mehboob, Mauricio Restrepo, Claudio A Cañizares, Catherine Rosenberg, and Mehrdad Kazerani. Smart operation of electric vehicles with four-quadrant chargers considering uncertainties. *IEEE Transactions on Smart Grid*, 2018.

[28] Olivier Beaude, Samson Lasaulce, Martin Hennebel, and Ibrahim Mohand-Kaci. Reducing the impact of ev charging operations on the distribution network. *IEEE Transactions on Smart Grid*, 7(6):2666–2679, 2016.

[29] Bo Sun, Zhe Huang, Xiaoqi Tan, and Danny HK Tsang. Optimal Scheduling for Electric Vehicle Charging with Discrete Charging Levels in Distribution Grid. *IEEE Transactions on Smart Grid*, 2016.

[30] Mingxi Liu, Phillippe K Phanivong, Yang Shi, and Duncan S Callaway. Decentralized charging control of electric vehicles in residential distribution networks. *IEEE Transactions on Control Systems Technology*, (99):1–16, 2017.

[31] Ozan Erdinç, Akın Taşcıkaraoğlu, Nikolaos G Paterakis, Ilker Dursun, Murat Can Sinim, and João PS Catalão. Comprehensive optimization model for sizing and siting of dg units, ev charging stations, and energy storage systems. *IEEE Transactions on Smart Grid*, 9(4):3871–3882, 2017.

[32] Sitki Guner and Aydogan Ozdemir. Stochastic energy storage capacity model of ev parking lots. *IET Generation, Transmission & Distribution*, 11(7):1754–1761, 2017.

[33] Jian Zhao, Zhao Xu, Jianhui Wang, Cheng Wang, and Jiayong Li. Robust distributed generation investment accommodating electric vehicle charging in a distribution network. *IEEE Transactions on Power Systems*, 33(5):4654–4666, 2018.

[34] Samy Faddel, Tarek Youssef, Ahmed T Elsayed, and Osama A Mohammed. An automated charger for large-scale adoption of electric vehicles. *IEEE Transactions on Transportation Electrification*, 4(4):971–984, 2018.

[35] Marjan Gjelaj, Seyedmostafa Hashemi, Chresten Traeholt, and Peter Bach Andersen. Grid integration of dc fast-charging stations for evs by using modular li-ion batteries. *IET Generation, Transmission & Distribution*, 12(20):4368–4376, 2018.

[36] Pilar Meneses de Quevedo, Gregorio Muñoz-Delgado, and Javier Contreras. Impact of electric vehicles on the expansion planning of distribution systems considering renewable energy, storage and charging stations. *IEEE Transactions on Smart Grid*, 2017.

[37] Abdullah S. Bin Humayd and Kankar Bhattacharya. A Novel Framework for Evaluating Maximum PEV Penetration into Distribution Systems. *IEEE Trans. Smart Grid*, 9(4):1–1, Jul 2018.

[38] Daijiafan Mao, Ziran Gao, and Jiankang Wang. An integrated algorithm for evaluating plug-in electric vehicle's impact on the state of power grid assets. *International Journal of Electrical Power & Energy Systems*, 105:793–802, 2019.

[39] Di Wu, Dionysios C. Aliprantis, and Lei Ying. Load Scheduling and Dispatch for Aggregators of Plug-In Electric Vehicles. *IEEE Trans. Smart Grid*, 3(1):368–376, Mar 2012.

[40] Hongyu Wu, Mohammad Shahidehpour, Ahmed Alabdulwahab, and Abdullah Abusorrah. A game theoretic approach to risk-based optimal bidding strategies for electric vehicle aggregators in electricity markets with variable wind energy resources. *IEEE Transactions on Sustainable Energy*, 7(1):374–385, 2015.

[41] Mushfiqur R Sarker, Hrvoje Pandžić, Kaiwen Sun, and Miguel A Ortega-Vazquez. Optimal operation of aggregated electric vehicle charging stations coupled with energy storage. *IET Generation, Transmission & Distribution*, 12(5):1127–1136, 2017.

[42] Jun Tan and Lingfeng Wang. Coordinated optimization of PHEVs for frequency regulation capacity bids using hierarchical game. In *2015 IEEE Power & Energy Society General Meeting*, pages 1–5. IEEE, Jul 2015.

[43] Chioke B. Harris and Michael E. Webber. The impact of vehicle charging loads on frequency regulation procurements in ERCOT. In *ISGT 2014*, pages 1–5. IEEE, Feb 2014.

[44] Visvakumar Aravinthan and Ward Jewell. Controlled electric vehicle charging for mitigating impacts on distribution assets. *IEEE Transactions on Smart Grid*, 6(2):999–1009, 2015.

[45] Vijaykumar Prajapati et al. Congestion management of power system with uncertain renewable resources and plug in electrical vehicle. *IET Generation, Transmission & Distribution*, 2019.

[46] Yin Yao, David Wenzhong Gao, and James Momoh. Dual-optimisation of power sources including plug-in electric vehicles and renewable energy resources

at transmission-level system. *The Journal of Engineering*, 2019(5):3448–3454, 2019.

[47] Xuan Wu, Antonio J Conejo, and Nima Amjady. Robust security constrained acopf via conic programming: Identifying the worst contingencies. *IEEE Transactions on Power Systems*, 33(6):5884–5891, 2018.

[48] Saeed Naghdizadegan Jahromi, Alireza Askarzadeh, and Amir Abdollahi. Modelling probabilistic transmission expansion planning in the presence of plug-in electric vehicles uncertainty by multi-state Markov model. *IET Gen., Trans. & Dist.*, 11(7):1716–1725, May 2017.

[49] Yunfei Mu, Jianzhong Wu, Nick Jenkins, Hongjie Jia, and Chengshan Wang. A Spatial–temporal Model for Grid Impact Analysis of Plug-in Electric Vehicles. *Applied Energy*, 114:456–465, 2014.

[50] Francis Mwasilu, Jackson John Justo, Eun-Kyung Kim, Ton Duc Do, and Jin-Woo Jung. Electric vehicles and smart grid interaction: A review on vehicle to grid and renewable energy sources integration. *Renewable and sustainable energy reviews*, 34:501–516, 2014.

[51] Qiuming Gong, Shawn Midlam-Mohler, Vincenzo Marano, and Giorgio Rizzoni. Study of PEV Charging on Residential Distribution Transformer Life. *IEEE Transactions on Smart Grid*, 3(1):404–412, 2012.

[52] Murat Yilmaz and Philip T Krein. Review of the Impact of Vehicle-to-grid Technologies on Distribution Systems and Utility Interfaces. *IEEE Transactions on Power Electronics*, 28(12):5673–5689, 2013.

[53] Luis Pieltain Fernandez, Tomas Gomez San Roman, Rafael Cossent, Carlos Mateo Domingo, and Pablo Frías. Assessment of the Impact of Plug-in Electric Vehicles on Distribution Networks. *IEEE Transactions on Power Systems*, 26(1):206–213, 2011.

[54] Soroush Shafiee, Mahmud Fotuhi-Firuzabad, and Mohammad Rastegar. Investigating the Impacts of Plug-in Hybrid Electric Vehicles on Power Distribution Systems. *IEEE Transactions on Smart Grid*, 4(3):1351–1360, 2013.

[55] Rong-Ceng Leou, Chun-Lien Su, and Chan-Nan Lu. Stochastic Analyses of Electric Vehicle Charging Impacts on Distribution Network. *IEEE Transactions on Power Systems*, 29(3):1055–1063, 2014.

[56] Kejun Qian, Chengke Zhou, Malcolm Allan, and Yue Yuan. Modeling of Load Demand due to EV Battery Charging in Distribution Systems. *IEEE Transactions on Power Systems*, 26(2):802–810, 2011.

[57] ABB. Total Cost of Ownership Calculator. *[Online] Available at: http://tcocalculator.abb.com.*

[58] Daijiafan Mao, Danielle Meyer, and Jiankang Wang. Evaluating PEV's Impact on Long-term Cost of Grid Assets. In *Power & Energy Society Innovative Smart Grid Technologies Conference (ISGT)*, pages 1–5. IEEE, 2017.

[59] Daijiafan Mao, Karun Potty, and Jiankang Wang. The impact of power-electronics-based load dynamics on large-disturbance voltage stability. In *2018 IEEE Power & Energy Society General Meeting (PESGM)*, pages 1–5. IEEE, 2018.

[60] Ziran Gao, Daijiafan Mao, and Jiankang Wang. Distribution grid response monitor. *IET Generation, Transmission & Distribution*, 13(19):4374–4381, 2019.

[61] Rural Utilities Services. Guide for Economic Evaluation of Distribution Transformers. 2016.

[62] IEC. 60076-7: 2005 Loading Guide for Oil-Immersed Power Transformers. *International Electrotechnical Commission, Geneva, Switzerland*, 2005.

[63] IEEE. Standard C57.91-1995 Guide for Loading Mineral-oil Immersed Transformers. 57:1–112, 1995.

[64] EPRI. OpenDSS Manual. *[Online] Available at: http://sourceforge. net/apps/mediawiki/electricdss/index. php.*

[65] Longcheng Tan, Bin Wu, Sebastian Rivera, and Venkata Yaramasu. Comprehensive DC Power Balance Management in High-power Three-level DC–DC Converter for Electric Vehicle Fast Charging. *IEEE Transactions on Power Electronics*, 31(1):89–100, 2016.

[66] Adella Santos, Nancy McGuckin, Hikari Yukiko Nakamoto, Danielle Gray, and Susan Liss. Summary of Travel Trends: 2009 National Household Travel Survey. Technical report, 2011.

[67] Ziran Gao and Jiankang Wang. Visualizing the Impact of PEV on Power Distribution Grids. In *Transportation Electrification Conference and Expo (ITEC)*. IEEE, 2018.

[68] Mark Singer. Consumer Views on Plug-in Electric Vehicles–National Benchmark Report. Technical report, NREL (National Renewable Energy Laboratory (NREL), Golden, CO (United States)), 2016.

[69] David Block, Paul Brooker, et al. Prediction of Electric Vehicle Penetration (2017). *EVTC Report Number: FSEC-CR-2069-17*, 2017.

[70] Stephanie Searle, Nikita Pavlenko, and Nic Lutsey. Leading Edge of Electric Vehicle Market Development in the United States: An Analysis of California Cities, 2016.

[71] Nic Lutsey. California's Continued Electric Vehicle Market Development (2018). 2018.

[72] PK Sen, S Pansuwan, K Malmedal, O Martinoo, M Godoy Simoes, and K Butler-Purry. Transformer Overloading and Assessment of Loss-of-life for Liquid-filled Transformers (2011). *Power Systems Engineering Research Center (PSERC)*, 2011.

[73] Chen Yuan, Mahesh S Illindala, and Amrit S Khalsa. Modified Viterbi Algorithm based Distribution System Restoration Strategy for Grid Resiliency. *IEEE Transactions on Power Delivery*, 32(1):310–319, 2017.

[74] EPRI. Understanding the Grid Impacts of Plug-In Electric Vehicles (PEV): Phase 1 Study – Distribution Impact Case Studies Palo Alto, CA. Technical report, 2012.

[75] N Yorino, H Sasaki, Y Masuda, Y Tamura, M Kitagawa, and A Oshimo. An investigation of voltage instability problems. *IEEE transactions on power systems*, 7(2):600–611, 1992.

[76] GK Morison, B Gao, and P Kundur. Voltage stability analysis using static and dynamic approaches. *IEEE transactions on Power Systems*, 8(3):1159–1171, 1993.

[77] B Gao, GK Morison, and P Kundur. Towards the development of a systematic approach for voltage stability assessment of large-scale power systems. *IEEE transactions on power systems*, 11(3):1314–1324, 1996.

[78] PW Sauer and MA Pai. Power system steady-state stability and the load-flow jacobian. *IEEE Transactions on power systems*, 5(4):1374–1383, 1990.

[79] C-C Liu and Khoi T Vu. Analysis of tap-changer dynamics and construction of voltage stability regions. *IEEE Transactions on circuits and systems*, 36(4):575–590, 1989.

[80] Wilsun Xu and Yakout Mansour. Voltage stability analysis using generic dynamic load models. *IEEE Transactions on Power Systems*, 9(1):479–493, 1994.

[81] Thierry Van Cutsem and Costas Vournas. *Voltage stability of electric power systems*, volume 441. Springer Science & Business Media, 1998.

[82] Petar Kokotović, Hassan K Khalil, and John O'reilly. *Singular perturbation methods in control: analysis and design*. SIAM, 1999.

[83] Hassan K Khalil. Noninear systems. *Prentice-Hall, New Jersey*, 2(5):5–1, 1996.

[84] CH Dharmakeerthi and N Mithulananthan. PEV load and its impact on static voltage stability. In *Plug In Electric Vehicles in Smart Grids*, pages 221–248. Springer, 2015.

[85] Silva Hiti. *Modeling and control of three-phase PWM converters*. PhD thesis, 1995.

[86] Damon Bazargan, Shaahin Filizadeh, and Ani M Gole. Stability analysis of converter-connected battery energy storage systems in the grid. *IEEE Transactions on Sustainable Energy*, 5(4):1204–1212, 2014.

[87] Ulas Eminoglu and M Hakan Hocaoglu. A new power flow method for radial distribution systems including voltage dependent load models. *Electric power systems research*, 76(1):106–114, 2005.

[88] Luis Herrera, Wei Zhang, and Jin Wang. Stability analysis and controller design of dc microgrids with constant power loads. *IEEE Transactions on Smart Grid*, 2015.

[89] Hsiao-Dong Chiang, Felix F Wu, and Pravin P Varaiya. A bcu method for direct analysis of power system transient stability. *IEEE Transactions on Power Systems*, 9(3):1194–1208, 1994.

[90] David Howell, Steven Boyd, Brian Cunningham, Samm Gillard, Lee Slezak, Shabbir Ahmed, Ira Bloom, Andrew Burnham, Keith Hardy, Andrew N Jansen, et al. Enabling fast charging: A technology gap assessment. Technical report, 2017.

[91] Zhipeng Liu, Fushuan Wen, and Gerard Ledwich. Optimal planning of electric-vehicle charging stations in distribution systems. *IEEE Transactions on Power Delivery*, 28(1):102–110, 2012.

[92] Hongcai Zhang, Zechun Hu, Zhiwei Xu, and Yonghua Song. An integrated planning framework for different types of pev charging facilities in urban area. *IEEE Transactions on Smart Grid*, 7(5):2273–2284, 2015.

[93] Lizi Luo, Wei Gu, Suyang Zhou, He Huang, Song Gao, Jun Han, Zhi Wu, and Xiaobo Dou. Optimal planning of electric vehicle charging stations comprising multi-types of charging facilities. *Applied energy*, 226:1087–1099, 2018.

[94] Soodeh Negarestani, Mahmud Fotuhi-Firuzabad, Mohammad Rastegar, and Abbas Rajabi-Ghahnavieh. Optimal sizing of storage system in a fast charging station for plug-in hybrid electric vehicles. *IEEE transactions on transportation electrification*, 2(4):443–453, 2016.

[95] Daijiafan Mao, Hussam J Khasawneh, Mahesh S Illindala, Benjamin L Schenkman, and Daniel R Borneo. Economic evaluation of energy storage options in a microgrid with flexible distribution of energy and storage resources. In *2015 IEEE/IAS 51st Industrial & Commercial Power Systems Technical Conference (I&CPS)*, pages 1–7. IEEE, 2015.

[96] Tianyang Zhang, Xi Chen, Zhe Yu, Xiaoyan Zhu, and Di Shi. A monte carlo simulation approach to evaluate service capacities of ev charging and battery swapping stations. *IEEE Transactions on Industrial Informatics*, 14(9):3914–3923, 2018.

[97] Giambattista Gruosso, Giancarlo Storti Gajani, Zheng Zhang, Luca Daniel, and Paolo Maffezzoni. Uncertainty-aware computational tools for power distribution networks including electrical vehicle charging and load profiles. *IEEE Access*, 7:9357–9367, 2019.

[98] Zohreh Fotouhi, Massoud Reza Hashemi, Hamed Narimani, and Islam Safak Bayram. A general model for ev drivers' charging behavior. *IEEE Transactions on Vehicular Technology*, 68(8):7368–7382, 2019.

[99] Ahmed Abdalrahman and Weihua Zhuang. Pev charging infrastructure siting based on spatial-temporal traffic flow distribution. *IEEE Transactions on Smart Grid*, 2019.

[100] Yanyan Xu, Serdar Çolak, Emre C Kara, Scott J Moura, and Marta C González. Planning for electric vehicle needs by coupling charging profiles with urban mobility. *Nature Energy*, 3(6):484, 2018.

[101] Yue Xiang, Junyong Liu, Ran Li, Furong Li, Chenghong Gu, and Shuoya Tang. Economic planning of electric vehicle charging stations considering traffic constraints and load profile templates. *Applied Energy*, 178:647–659, 2016.

[102] Hongcai Zhang, Scott J Moura, Zechun Hu, and Yonghua Song. Pev fast-charging station siting and sizing on coupled transportation and power networks. *IEEE Transactions on Smart Grid*, 9(4):2595–2605, 2018.

[103] Guibin Wang, Zhao Xu, Fushuan Wen, and Kit Po Wong. Traffic-constrained multiobjective planning of electric-vehicle charging stations. *IEEE Transactions on Power Delivery*, 28(4):2363–2372, 2013.

[104] Hongcai Zhang, Scott J Moura, Zechun Hu, Wei Qi, and Yonghua Song. Joint pev charging network and distributed pv generation planning based on accelerated generalized benders decomposition. *IEEE Transactions on Transportation Electrification*, 2018.

[105] Akanksha Shukla, Kusum Verma, and Rajesh Kumar. Multi-objective synergistic planning of ev fast-charging stations in the distribution system coupled with the transportation network. *IET Generation, Transmission & Distribution*, 13(15):3421–3432, 2019.

[106] Hongcai Zhang, Scott J Moura, Zechun Hu, Wei Qi, and Yonghua Song. A second-order cone programming model for planning pev fast-charging stations. *IEEE Transactions on Power Systems*, 33(3):2763–2777, 2017.

[107] LI Xiang, Qing-guang LI, Hai-long WANG, and Ning-hui ZHU. Planning of fast charging stations considering distribution grid and transportation network. *DEStech Transactions on Environment, Energy and Earth Sciences*, (epeee), 2018.

[108] Daijiafan Mao, Jiankang Wang, Jun Tan, Guangyi Liu, Yiran Xu, and Jie Li. Location planning of fast charging station considering its impact on the power grid assets. In *2019 IEEE Transportation Electrification Conference and Expo (ITEC)*, pages 1–5. IEEE, 2019.

[109] M John Hodgson. A flow-capturing location-allocation model. *Geographical Analysis*, 22(3):270–279, 1990.

[110] Fei Wu and Ramteen Sioshansi. A stochastic flow-capturing model to optimize the location of fast-charging stations with uncertain electric vehicle flows. *Transportation Research Part D: Transport and Environment*, 53:354–376, 2017.

[111] Gelli Ravikumar and Shrikrishna A Khaparde. A common information model oriented graph database framework for power systems. *IEEE Transactions on Power Systems*, 32(4):2560–2569, 2016.

[112] R. Dai, G. Liu, Z. Wang, B. Kan, and C. Yuan. A novel graph-based energy management system. *IEEE Transactions on Smart Grid*, pages 1–1, 2019.

[113] Chen Yuan, Yuqi Zhou, Guofang Zhang, Guangyi Liu, Renchang Dai, Xi Chen, and Zhiwei Wang. Exploration of graph computing in power system state estimation. In *2018 IEEE Power & Energy Society General Meeting (PESGM)*, pages 1–5. IEEE, 2018.

[114] Chen Yuan, Yi Lu, Kewen Liu, Guangyi Liu, Renchang Dai, and Zhiwei Wang. Exploration of bi-level pagerank algorithm for power flow analysis using graph database. *arXiv preprint arXiv:1809.01415*, 2018.

[115] William H Kersting. *Distribution system modeling and analysis*. CRC press, 2006.

[116] National Electrical Manufacturers Association et al. *American National Standard for Electric Power Systems and Equipment-Voltage Ratings (60 Hertz)*. National Electrical Manufacturers Association, 1996.

[117] Hans Kellerer, Ulrich Pferschy, and David Pisinger. Knapsack problems, 2004.

[118] Albert YS Lam, Yiu-Wing Leung, and Xiaowen Chu. Electric vehicle charging station placement: Formulation, complexity, and solutions. *IEEE Transactions on Smart Grid*, 5(6):2846–2856, 2014.

[119] Reuven Y Rubinstein. Optimization of computer simulation models with rare events. *European Journal of Operational Research*, 99(1):89–112, 1997.

[120] Reuven Y Rubinstein. Combinatorial optimization, cross-entropy, ants and rare events. In *Stochastic optimization: algorithms and applications*, pages 303–363. Springer, 2001.

[121] Pieter-Tjerk De Boer, Dirk P Kroese, Shie Mannor, and Reuven Y Rubinstein. A tutorial on the cross-entropy method. *Annals of operations research*, 134(1):19–67, 2005.

[122] Jeffrey Dean and Sanjay Ghemawat. Mapreduce: simplified data processing on large clusters. *Communications of the ACM*, 51(1):107–113, 2008.

[123] Guangyi Liu, Chen Yuan, Xi Chen, Jingjin Wu, Renchang Dai, and Zhiwei Wang. A high-performance energy management system based on evolving graph. *IEEE Transactions on Circuits and Systems II: Express Briefs*, 2019.

[124] Gareth E Evans, Jonathan M Keith, and Dirk P Kroese. Parallel cross-entropy optimization. In *Proceedings of the 39th conference on Winter simulation*, pages 2196–2202. IEEE Press, 2007.

[125] William H Kersting. Radial distribution test feeders. In *Power Engineering Society Winter Meeting, 2001. IEEE*, volume 2, pages 908–912. IEEE, 2001.

[126] Andrew Burnham, Eric J Dufek, Thomas Stephens, James Francfort, Christopher Michelbacher, Richard B Carlson, Jiucai Zhang, Ram Vijayagopal, Fernando Dias, Manish Mohanpurkar, et al. Enabling fast charging–infrastructure and economic considerations. *Journal of Power Sources*, 367:237–249, 2017.

[127] Electrify america releases new app, big price changes. *Electric Revs*, 2019.

[128] Michail Vasiladiotis and Alfred Rufer. A modular multiport power electronic transformer with integrated split battery energy storage for versatile ultrafast ev charging stations. *IEEE Transactions on Industrial Electronics*, 62(5):3213–3222, 2014.

[129] Daniel Aggeler, Francisco Canales, H Zelaya, De La Parra, A Coccia, N Butcher, and O Apeldoorn. Ultra-fast dc-charge infrastructures for ev-mobility and future smart grids. In *2010 IEEE PES Innovative Smart Grid Technologies Conference Europe (ISGT Europe)*, pages 1–8. IEEE, 2010.

[130] IEEE recommended practice for conducting load-flow studies and analysis of industrial and commercial power systems. *IEEE Std 3002.2-2018*, pages 1–73, Nov 2018.

[131] Danielle Meyer and Jiankang Wang. Integrating Ultra-fast Charging Stations within the Power Grids of Smart Cities: A Review. *IET Smart Grid (2018)*, 2018.

[132] A Muir and J Lopatto. Final report on the august 14, 2003 blackout in the united states and canada: Causes and recommendations. 2004.

[133] Ian Dobson, BA Carreras, V Lynch, and D Newman. An initial model for complex dynamics in electric power system blackouts. In *hicss*, page 2017. Citeseer, 2001.

[134] Shengwei Mei, Fei He, Xuemin Zhang, Shengyu Wu, and Gang Wang. An improved opa model and blackout risk assessment. *IEEE Transactions on Power Systems*, 24(2):814–823, 2009.

[135] Gan Zhou, Rui Bo, Lungsheng Chien, Xu Zhang, Fei Shi, Chunlei Xu, and Yanjun Feng. Gpu-based batch lu-factorization solver for concurrent analysis of massive power flows. *IEEE Transactions on Power Systems*, 32(6):4975–4977, 2017.

[136] Wenyun Ju, Kai Sun, and Junjian Qi. Multi-layer interaction graph for analysis and mitigation of cascading outages. *IEEE Journal on Emerging and Selected Topics in Circuits and Systems*, 7(2):239–249, 2017.

[137] F. Marra, Guang Ya Yang, E. Larsen, C. N. Rasmussen, and Shi You. Demand profile study of battery electric vehicle under different charging options. In *2012 IEEE Power and Energy Society General Meeting*, pages 1–7. IEEE, Jul 2012.

[138] Alireza Hatefi Einaddin and Ahmad Sadeghi Yazdankhah. A novel approach for multi-objective optimal scheduling of large-scale ev fleets in a smart distribution grid considering realistic and stochastic modeling framework. *International Journal of Electrical Power & Energy Systems*, 117:105617, 2020.

[139] U.S. Department of Energy. AVTA: ARRA EV Project Charging Infrastructure Data Summary Reports. Technical report.

[140] Michael J Kuby, Scott B Kelley, and Joseph Schoenemann. Spatial refueling patterns of alternative-fuel and gasoline vehicle drivers in los angeles. *Transportation Research Part D: Transport and Environment*, 25:84–92, 2013.

[141] Anmar Frangoul. With new electric vehicle, london's iconic black cabs are about to go green. `https://www.cnbc.com/2017/07/12/londons-iconic-black-cabs-are-about-to-go-green.html`. Accessed 2017.

[142] Zach Mcdonald. Electric taxis are on their way. `https://www.fleetcarma.com/electric-taxis-on-their-way/`. Accessed 2017.

[143] Chen Yuan, Yi Lu, Wei Feng, Guangyi Liu, Renchang Dai, Yachen Tang, and Zhiwei Wang. Graph computing based distributed fast decoupled power flow analysis. *arXiv preprint arXiv:1902.06893*, 2019.

[144] Junjie Shi, Guangyi Liu, Renchang Dai, Jingjin Wu, Chen Yuan, and Zhiwei Wang. Graph based power flow calculation for energy management system. In *2018 IEEE Power & Energy Society General Meeting (PESGM)*, pages 1–5. IEEE, 2018.

[145] Joseph WH Liu. The role of elimination trees in sparse factorization. *SIAM journal on matrix analysis and applications*, 11(1):134–172, 1990.

[146] Saleh Soltan, Dorian Mazauric, and Gil Zussman. Analysis of failures in power grids. *IEEE Transactions on Control of Network Systems*, 4(2):288–300, 2015.